Università degli Studi di Salerno

Facoltà di Scienze

Matematiche, Fisiche e Naturali

Dipartimento di Fisica "E. R. Caianiello"

Dottorato di Ricerca in Fisica

X Ciclo, 2° Serie (2008-2011)

The ground deformations: tools, methods and application to some Italian volcanic regions

Coordinator: Prof. Giuseppe Grella
Tutor: Prof. Roberto Scarpa

Dott. Pierdomenico Romano

Table Of Contents

Abstract

The objective of this thesis is the study of slow deformation of the soil as a result of intrusion of magma inside the magmatic chambers of some volcanoes located in Southern Italy. In particular, the Mt. Vesuvius and Campi Flegrei caldera have been monitored over the last 7 years. The research has been accomplished through the use of geodetic instrumentation (long baseline tiltmeters, Sacks-Evertson dilatometers) that has been installed during the entire period of the research near the aforementioned volcanoes. The data were recorded with the aid of data-logger, some of which are specifically designed for the current research.

Campi Flegrei and Mt. Vesuvius are two volcanoes located near Naples, already monitored by Osservatorio Vesuviano, the local office of INGV (Istituto Nazionale di Geofisica e Vulcanologia). In the last 40 years systematic recordings of seismic data, of changes in distance of milestones, of leveling lines, of local gravimetric anomalies and of GPS-InSAR data have been carried out. Starting from 2004, the monitoring network maintained by Osservatorio Vesuviano has been enriched by the DINEV project: this is intended as a complementary network of geodetic stations and consists in the installation of a small array of 6 borehole stations (with an average depth of 120 m), each of which is constituted by a three components borehole broadband seismometer Teledyne Geotech KS2000BH and a Sacks-Evertson areal strainmeter (dilatometer). In addition, two three components surface broadband seismometers Guralp CMG 3-ESP have been installed to control the anthropogenic surface noise.

In Campi Flegrei caldera, then, another array of instruments has been installed: two long baseline water tiltmeters have been installed in Italian Army abandoned tunnels. The total length of tiltmeters is about 350 m for the northernmost tunnel, and of about 150 m for the southernmost tunnel. Tiltmeters were installed, respectively, in axial and tangential direction in respect with the position of the Campi Flegrei magmatic chamber.

The use of the instruments described in the current report allows to model the strain field in the range of low frequencies, monitoring the deformation tensor for its non-diagonal components (pure tilt) by using the tiltmeters, and the diagonal components (pure deformation) by using the dilatometers.

The monitoring is occurred for a time range of some years in length, needed to remove the seasonal drifts due to changes in rainfalls, while the deformation due to changes in barometric pressure have been deleted using linear regression techniques.

Chapter 1 – Introduction

Seismic and volcanic processes are usually associated to catastrophes and other kind of destructive phenomena, but, from a geophysical and geological point of view, they represent even the only signals Earth gives us in order to allow scientists to understand the complex dynamics that still regulate the changes in our young planet.

The internal structure of the Earth can, so, be understood by an inverse analysis that starts from these phenomena: following the strategies developed by geophysicists it is, in fact, ideally possible to learn what the Earth contains in its depths and, hopefully, one day predict the next catastrophic event.

The study of the Earth's internal structure is performed by using a huge range of different instruments, each of them recording a different kind of signal.

Seismic waves have been constantly monitored, recorded and analyzed in the past decades, allowing scientists to better understand how the Earth's interior is layered, and all the theoretical studies performed over the data recorded by the seismic networks available all over the World gave us a more precise idea of Earth's internal structure, how seismic waves travel in the depths and on surfaces which separate the different layers, and the kind and entity of damages they could do to human artifacts. Seismic waves transport high frequency energy, which can be easily monitored through the usage of a wide range of different seismometers (accelerometers, velocity transducers and so on).

The spectrum of the energies emitted by the Earth, anyway, has a wide series of different values, ranging from the very high frequencies of body waves, to the very low frequencies of the secular strain, as represented in Table 1-1. In this context, seismology and geodesy represent the two extremes for geophysicists. Seismology can be seen as the branch of geophysics which studies the phenomena related with the high frequency energy emission due to earthquakes, strong motion events, volcanic eruptions and so on. Geodesy, on the other hand, is the branch of geophysics related with the study of emission of energy at lower frequency: Earth tides, tectonic plates subduction, aseismic deformations, magmatic chambers pressure changes, crustal deformation are all examples of low frequency phenomena which are described by the geodesy.

Table 1-1 – Frequency ranges vs. geophysical phenomena

Frequency range	Phenomenon
$10^{-8} \div 10^{-7}$ Hz	Secular strain
$10^{-6} \div 10^{-4}$ Hz	Tides
$10^{-5} \div 10^{-1}$ Hz	Afterslip – Slow ruptures
$10^{-3} \div 10^{-2}$ Hz	Dynamic fault rupture
$10^{-3} \div 10^{3}$ Hz	Body waves propagation

Lower frequency doesn't mean lesser energy: usually low frequency waves transport even higher energies than the most destructive earthquake, even if in the former case energies are averaged on a longer time than the latter case.

Geodetic phenomena are related with deep changes of the Earth's interior: the monitoring of these events can be used to verify the Earth's response to gravitational interaction with celestial bodies (Sun-Moon system interaction which generates the Earth tides) and the plate tectonic theory, and even to predict possible volcanic eruptions through the analysis of strain and tilt data near large volcanic calderas.

The following PhD thesis is about the development of an integrated network of instruments which are used to record and analyze deformation data coming from the Campi Flegrei-Mt. Vesuvius volcanic region, located in the southern part of the Italian peninsula. The instrument network deployed by University of Salerno, with international scientific partners (Carnegie Institution of Washington, Washington D.C. and University of Colorado, Denver), consists of areal strainmeters and tiltmeters, associated with broad-band seismometers and barometric pressure transducers.

During the years 2004-2005 an array of 6 borehole areal strainmeters (dilatometers) was installed in the region, in order to record strain tensor diagonal components. To improve the recording quality, barometric pressure was also taken in account, recording it at the same sampling frequency of the strain, and thereafter removed from the raw strain trends: since the dilatometers output can in principle be expressed as a linear combination of areal strain and vertical strain due to barometric changes, the strain changes due to the atmospheric pressure can be modeled just as an uniaxial stress or strain (or more rigorously as distributed loads applied to the surface of a half-space, to a layer of distinct elastic properties overlying the half-space, or to the surface of a spherical earth).

The six dilatometers were installed in boreholes separated each other by several kilometers, and the so developed network was chosen to cover critical distances from the crustal magma bodies which underlie beneath the Campi Flegrei and Vesuvius volcanoes.

In order to further improve the network, each station was integrated with a three-component broad-band accelerometer, to avoid the strain field changes due to high frequency seismic waves and to calibrate the dilatometers in the high frequency range.

During the years 2007-2008, moreover, near the Campi Flegrei caldera were installed two long baseline water-filled tiltmeters: tilt components (i.e., the components not lying on the diagonals) of the strain tensor can be monitored through the data recorded by tiltmeters.

The complete network of instruments can, so, be used to monitor all the strain tensor components.

1.1 – Strainmeters and Dilatometers

Stresses and strains have long been of great importance in various human activities. Engineers are used to use small devices, known as strain gauges, in which the resistance of a metal wire or semiconductive film varies with strain. In the past, these devices where tried to be used even by geophysicist in order to measure rock stress: the results were poor, because of their insensibility. Geophysicists, then, started to design their own strainmeters.

Most of the geophysical strainmeters are extensometers, measuring the displacement between two separated points. Extensometers may usefully be divided into three classes according to what they use to span the distance between endpoints: rod strainmeters (some used in boreholes), wire strainmeters and optical strainmeters. A final class of strainmeters uses hydraulic amplification to make borehole measurements: the best known example of this class of strainmeters, which is even the instrument used in the following of the current report, is the Sacks-Evertson areal dilatometer.

1.1.1 – Rod Strainmeters

The very first rod strainmeter ever built for seismometry, was produced by Benioff in early 1930s. This instrument consists of a 20m iron pipe attached at one end to a pier and at the other to a variable reluctance transducer, which drove a recording galvanometer. Using a solid rod to transfer the relative displacement of one point to another has the merit of extreme simplicity: for all but the highest frequencies the rod may be treated as a rigid body, and the frequency response is flat. Typically it was used as active element a velocity transducer, which made the instrument a strain rate gauge, which is desirable for seismic recording because it reduces the noise from temperature fluctuations and tides. Many different rod strainmeters have been developed during time, by only changing the rod material and the way in which the displacements between rod and piers are measured.

Many rod strainmeters were built so that they were able to measure tidal and secular strains, whose typical frequencies are completely ignored by seismometers due to their own design.

Because the displacements measured by mechanical rod strainmeters are very small, an accurate calibration is difficult. Benioff applied a force to the free end of the strainmeter rod and used its known elasticity to convert this to a displacement. Another calibration method usually followed, is to mount the fixed part of the sensor on a motion reducer driven by a micrometer. Lately, interferometers have also been used for calibration of rod strainmeters and to record their long-term motion.

In the most recent period, borehole extensometers have been deployed too. Because of the advantages of a borehole instrument, both in flexibility of deployment and possible long-term stability, several miniature rod extensometers have been built for borehole installations. In all of these the ends of extensometer are attached to a thin canister that is cemented to the borehole wall. Because the base-length is short, the displacements to be detected are small, and they are usually measured with capacitance sensors. *Moore et al. [1974]* designed a borehole strainmeter that used a 0.14m quarts-rod length standard. At high frequencies the nominal noise was -230dB relative to $1\frac{\varepsilon^2}{Hz}$. The only installation reported was made in a 1.5m deep borehole drilled in a mine tunnel: the strainmeter recorded tides adequately and showed an exponentially decreasing drift (about 10^{-13} s^{-1} after 200 days) presumably from cement expansion.

1.1.2 – Wire Strainmeters

Although several rigid-rod strainmeters have been designed to be portable, this has never been practical because the length standard is so cumbersome. As a more convenient alternative, several designs have instead used a flexible wire. Because a wire must be supported by keeping it in tension, which increases creep, this might seem unwise, but in fact wire strainmeters have been very successful, especially for tidal measurements. The earliest design hung an Invar wire between two points in a shallow catenary; changes in the distance between the ends caused the bottom of the catenary to rise and fall. This motion was recorded with an optical lever. More recent instruments stem from the design by *Sydenham [1969]* of a strainmeter in which the wire is fixed at one end and at the other is free to move but kept under constant tension.

The design of such an instrument is governed by the theory of a flexible line suspended in a catenary. The usual development *[Bomdford, 1962]* gives the relation between base-length *l*, wire length *w*, and central sag *y* as

$$w = L_C sinh\left(\frac{l}{L_C}\right) \tag{1.1.1}$$

$$y = \frac{1}{2}L_C\left[cosh\left(\frac{l}{L_C}\right) - 1\right] \tag{1.1.2}$$

where the catenary scaling length L_C is $\frac{2F_0}{\rho g A_w}$, ρ being the density of the wire and A_w its cross-sectional area. F_0 is the tension at the lowest point; for a shallow catenary this is very near the tension at the end. This tension will stretch the wire elastically to an extension e_w; expressing F_0 in terms of e_w, we find

$$L_C = 2e_w \frac{E}{\rho g} \equiv e_w L_w \qquad (1.1.3)$$

where E is the Young's modulus of the material and we have defined a wire scaling length $L_w = \frac{2E}{\rho g}$. For a given material, L_w is fixed and while it is desirable to make L_C large to keep the catenary flat, this entails increasing e_w, which should be kept small to minimize creep.

Because the length standard is flexible, wire strainmeters have many spurious resonances at relatively low frequencies *[Bilham and King, 1971]*. One mode is longitudinal oscillation of the wire and tensioning system. Tension is usually applied by a weight on a lever; in a longitudinal oscillation this act as a mass and the wire as a spring. The frequency of oscillation f_l depends on the moment of inertia of the tensioning system (I_p), the distance from the pivot point to the attachment point of the wire (r_a), and the effective spring constant of the wire, which acts as it had a Young's modulus of $\frac{E}{W}$. The result is

$$f_l = \frac{r_a}{2\pi} \left(\frac{A_w E}{I_P W} \right)^{1/2}. \qquad (1.1.4)$$

The wire can also oscillate transversely, with the restoring force being some combination of tension and gravity. The gravest purely tensional mode has a frequency of

$$f_t = \frac{1}{l} \left(\frac{g L_w e_w}{8} \right)^{1/2}. \qquad (1.1.5)$$

It is relatively easy to make these frequencies a few hertz (above the microseism band), but difficult to make them much larger: wire strainmeters are poor seismometers.

1.1.3 – Laser Strainmeters

Because the wavelength of light, unlike any material object, is an invariant standard, interferometry has obvious attractions for strain measurements. The development of the laser, with its very long coherence length, made it possible to build extensometers using interferometers with very unequal arms. Though several groups have built laser strainmeters, only a few designs have produced significant results. Among the others, here should be mentioned the laser strainmeter produced by the University of California, San Diego (UCSD) [*Berger and Lovberg, 1970*], the instrument from Cambridge University [*Goulty et al., 1974*] and one from the U.S. National Bureau Of Standards (NBS) [*Levine and Hall, 1972*]. All of the hundreds of other laser strainmeters are evolution of the design of the above mentioned instruments, which will be used in the following of the current paragraph as a reference.

The USCD strainmeter used the most straightforward optical design: an unequal-arm Michelson interferometer, in which changes in the length of the long arm cause fringe shifts at the detector. Counting fringes gives the strain change, with the frequency response and dynamic range being limited by the counting electronics. Using suitable optics, a change of $\lambda/4$ can be detected in the path length difference Λ:

since the path length is twice the instrument base-length *l*, this corresponds to a strain of $\lambda/8l$. While the optics are relatively simple, *l* must be fairly large to get adequate resolution. For the UCSD instrument, *l* is 731m, giving a least count of 0.108 nε. This length means that the instrument has to be located above ground, in fact, building an instrument that could be so installed was a goal of this design, since such a surface installation allows a wider choice of sites than one in mines and tunnels.

Figure 1.1 – Mechanical design of the UCSD laser strainmeter. The two endpoints are tall piers of dimension stone sunk in the ground. These, and the optics they carry, are inside temperature-controlled enclosures in air-conditioned buildings. The measurement path is inside a vacuum pipe except at the very ends; telescopic joints keep the length of the air paths constant.
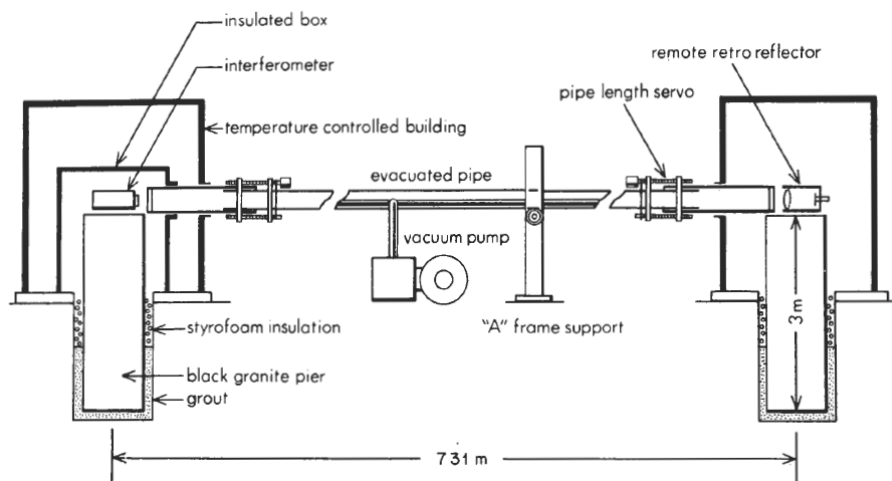
On the other hand, a surface installation complicates the mechanical design of the strainmeter (Figure 1.1). Almost all of the optical path along the long arm runs through a pipe evacuated to 1 Pa, so that temperature and pressure changes do not matter. For ease of adjustment the interferometer optics and remote retro-reflector are not in the vacuum. Because of this, any motion of the end of the evacuated pipe changes the proportion of the path in air and in vacuum, and therefore the optical path length, with 1mm of motion causing an apparent strain of 0.4 nε. Temperature changes cause the aluminum pipe to expand and contract up to 0.6 m. To eliminate this problem, the vacuum pipe is anchored in the middle, and telescopic joints are put at each end; these joints are servo-controlled to keep the end of the evacuated path a constant distance from the optics. A prism at the midpoint of the pipe allows a break in the optical path, so that the pipe need not be in a single straight section. The optics at each end are inside heavily-insulated boxes in small air-conditioned buildings In the three instruments first built the endpoints were long columns (up to 4 m) of dimension stone sunk into the ground, Because these tilted (causing spurious strains), the endpoints for the fourth instrument were short piers in vaults just below the surface. Displacements of these piers proved to be large enough [*Wyatt, 1982*] that optical anchors were needed to correct for them.

The optical system had lots of refinements, one of which was the isolation of the laser from the light returning through the beam-splitter, using a polarizer and quarter-wave plate. This is needed to keep the laser from "seeing" the modes of the optical cavity formed by the long interferometer arm, and having its frequency pulled towards them. Because of the length of the instrument, the laser beam must be expanded before being sent into the vacuum pipe, to reduce diffractive spreading.

The interferometer is illuminated by a single-frequency laser whose wavelength is stabilized by locking it to a reference cavity: it is formed by two mirrors, separated by a 30cm quartz spacer and kept in a tightly controlled environment. The mirrors form a Fabry-Perot interferometer [*Born and Wolf, 1980*] in which there is a multiple interference of the light that bounces back and forth between the two ends. If the mirrors transmit slightly so that light can be sent in one end, the ratio of intensity coming out the other to that sent in is

$$\frac{I_T}{I_l} = \left[1 + \frac{4F_n^2}{\pi^2} sin^2 \left(\frac{4\pi \Lambda_c}{\lambda}\right)\right]^{-1}$$
(1.1.6)

where λ is the wavelength of the light, Λ_c is the optical path length between the ends (including phase shifts at the mirrors), and F_n the finesse (optical *Q*) of the system, which depends on the reflectivity and alignment of the mirrors. Even for highly reflective mirrors, the system is transparent for $\Lambda_c = \frac{N\lambda}{2}$ (*N* an integer) and transmits less well for other values of λ; for F_n large the transmittance falls rapidly as λ shifts away from one of the resonant values. About the instrument described here, the value of Λ_c is fixed and the laser light transmitted through it is measured by a photo-detector. Because F_n is about 100, small shifts in λ cause a large change in the intensity received. The signal from the photo-detector changes the size of the laser cavity to maximize this intensity.

In this paragraph it has been stressed out the design of the USCD laser-strainmeter since huge similitude there exist with the tiltmeters used in the following of the current report.

1.1.4 – Borehole Hydraulic Strainmeters

In his first strainmeter paper, *Benioff* [*1935*] suggested that dilatational strains might be measured by burying a large container of liquid with a small opening. Strains in the ground would change the volume of the container and force liquid to flow in and out; for a sufficiently small opening the flow could be detected. Benioff's idea does not seem to have been tried until 30 years later, when it was revived by Sacks and Evertson. Their very first design has seen wide use, especially in Japan [*Suyehiro, 1982*]; the most complete description of it is in the thesis written by *Evertson* [1977]. The basic principle is the same as that suggested by Benioff, with the sensing volume (Figure 1.2) cylindrical so that it fits in a borehole. The outer case is divided into two parts: the actual sensing volume, completely filled with liquid, and a smaller backing volume, partly filled with inert gas. Changes in the size of the sensing volume force liquid in and out of the backing volume, which offers little resistance because of the high compressibility of the gas. The liquid actually flows into and out of a bellows inside the backing volume, and the bellows motion is measured. The two volumes are also connected by a valve; if the sensing volume changes so much that the bellows would be pushed past its limits, opening this valve equalizes the pressure in the two volumes and re-zeroes the bellows. The tube connecting the sensing volume to the bellows attenuates high-frequency motions, protecting the bellows from large, rapid changes, such as those expected near an earthquake.

Figure 1.2 – Simplified cross-section through a Sacks-Evertson dilatometer, shown cemented in a borehole. The sensing volume S is largely filled by a hollow insert and has a filling port at the bottom. The only openings between the sensing volume (lower) and the backing volume (upper) are the re-zero valve V (shown open) and the capillary to the bellows B. A DC-LVDT L above the bellows measures the bellows motion
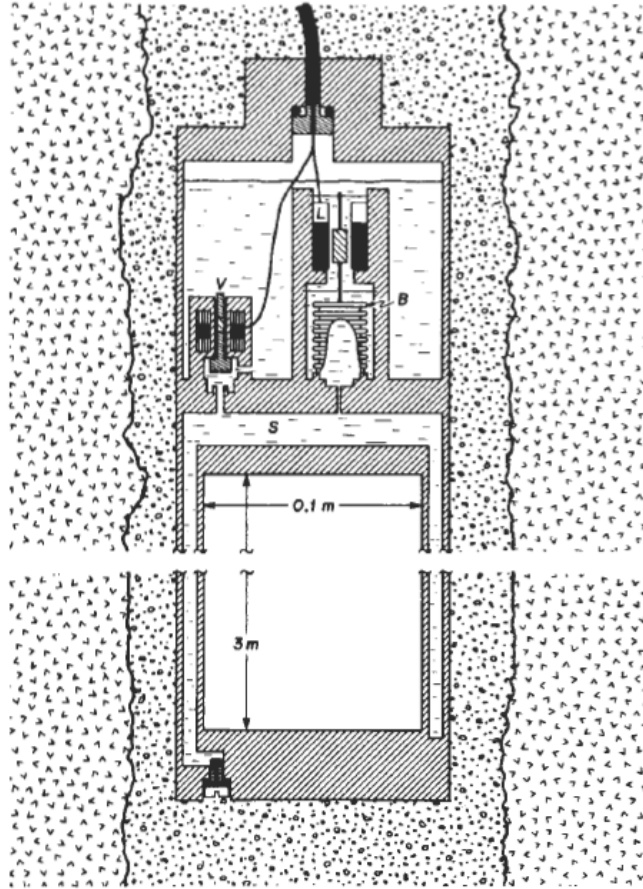
The response of the hydraulic system depends not only on the relative size of the volumes but also on the compressibility of the liquid in the sensing volume and on the stiffness of the bellows. If the bellows is much smaller than the sensing volume, we may assume the liquid in the bellows to be incompressible. The sensing volume is

$$v_s = v_s^0(1 + D) \tag{1.1.7}$$

where D is the dilatation of the instrument. The bellows volume is

$$v_b = v_b^0 + A_b q \tag{1.1.8}$$

where A_b is the effective area of the bellows and q the displacement of its end; this linear approximation is very accurate for well-made bellows [*Scaife et al., 1977*]. By conservation of mass we find

$$\left(\frac{p}{1 + \frac{p_s}{k_s}}\right) v_s^0(1 + D) + \rho(v_b^0 + A_b q) = \rho(v_s^0 + v_b^0) \tag{1.1.9}$$

where ρ is the density of the liquid, k_s its bulk modulus, and p_s the pressure in the sensing volume, which is given by

$$p_s = \frac{k_b q}{A_b} + \frac{128\eta L_t A_b}{\pi b_t^4}\dot{q} \qquad (1.1.10)$$

where the first term comes from the pressure produced by the bellows, which has a spring rate k_b, and the second term comes from the pressure drop along the connecting tube, assuming laminar flow. L_t is the tube length, b_t its diameter, and η the dynamic viscosity of the liquid. Making the approximation that $p_s << k_s$, these two equations can be combined to give

$$q\left(1 + \frac{k_b v_s^0}{A_b^2 k_s}\right) + \dot{q}\left(\frac{128\eta L_t v_s^0}{\pi b_t^4 k_s}\right) = -\frac{v_s^0}{A_b}D. \qquad (1.1.11)$$

At long periods the effect of liquid compressibility is thus to reduce the instrument response from the "ideal" $\left(-\frac{v_s^0}{A_b}\right)$ by a factor

$$K_H = \left(1 + \frac{k_b v_s^0}{A_b^2 k_s}\right)^{-1}. \qquad (1.1.12)$$

At high frequencies the connecting tube attenuates the response, acting as a single-pole low pass filter with a corner frequency of

$$f_c = \frac{b_t^4 k_s}{256 K_H \eta L_t v_s^0}. \qquad (1.1.13)$$

In the instruments put in Japan, v_s^0 was 0.033 m^3 and A_b 2 cm^2, giving an ideal response of $q = 170D$, so that the displacements to be measured were roughly the same as for a 170m extensometer. However, the liquid used (silicone oil) was relatively compressible ($k_s = 9 \times 10^8$ Pa), and the bellows relatively stiff ($k_b = 970$ N m^{-1}, though in fact 85% of this came from the stiffness of a piezoelectric displacement transducer), so that K_H was 0.51, reducing the effective "length" to 85m. Because the liquid had a relatively high viscosity (0.019 N s m^{-2}), it was not difficult to make b_t small enough for f_c to be about 1 Hz.

In the early instruments [*Sacks et al., 1971*] an inductive sensor measured the long-term bellows motion; in more recent versions, an LVDT is used for this, and the piezoelectric transducer has been eliminated. Another change has been done to reduce the volume of liquid by filling most of the sensing volume with a solid insert, usually a sealed hollow tube. This changes the apparent bulk modulus k_s from that of the liquid, k_L, to $\frac{k_L}{\left[\chi_L + (1-\chi_L)\frac{k_L}{k_l}\right]}$ where k_l is the bulk modulus of the insert and χ_L the fraction of v_s^0 occupied by liquid. Instruments recently installed in California have had $v_s^0 = 0.028$ m^3, $A_b = 0.43$ cm^2, and $k_b = 230$ N m^{-1}; given the increased effective rigidity of the liquid, the effective length was 325 m. The size of the connecting tube has been enlarged to raise f_c into a range near 10Hz.

The response of the instrument depends not only on the relation between q and Δ but also on that between instrument deformation and earth strain. If the instrument were perfectly flexible, the equations for an empty borehole show that

15

$$D = \left(\frac{2-\nu}{1-\nu}\right)\Delta \qquad\qquad (1.1.14)$$

where Δ is the volumetric strain in the absence of a hole and ν the Poisson's ratio of the material. An approximate solution [*Evertson, 1977*] to the problem of an elastic tube cemented into a hole shows that the vertical strain is not altered and that for the tube used in the Sacks-Evertson instrument, the areal strain is 90% of what it would be in an empty hole, the above equation remaining about right.

The success of this strainmeter depends on careful attention to details. For example, any gas bubbles in the sensing volume would greatly decrease k_s and reduce the response. To avoid this, the volume is filled under vacuum, the silicone oil being distilled into it to remove volatile components. The installation must also be done carefully. Sack's group places a slow-setting expansive cement of relatively low viscosity in the hole; the instrument is then lowered into this material, which sets around it, forming a tight pre-stressed bond.

While the Sacks-Evertson design is simple and robust, it cannot provide directional information. The borehole extensometers described above are one solution to this; another is a three-component hydraulic instrument developed by *Sakata et al.* [1982]. In this the sensing volume is almost completely filled by a solid cylinder, and the remaining annulus of liquid is divided into three sectors. The volume change of each sector is measured separately by a bellows and inductive displacement sensor, and the complete horizontal strain tensor is reconstructed form these three outputs.

1.2 – Inclinometers and Tiltmeters

Inclinometers and tiltmeters are instrument used by scientists to measure the inclination of a free surface (in our case, Earth's ground surface), and, thus, to obtain a direct measure of the tilt components of the strain tensor (i.e., the pure rotational changes in a solid half-space).

The best long baseline tiltmeters allow geophysicists to obtain an angular resolution up to 10^{-9} rad over a period of the order of the day, and an annual drift that gives a stability of the order of 10^{-6} rad/year, which means that the maximum error on measures, in this case, is a mere 10^{-6} rad.

Just as for the case of strainmeters, there exist different kind of tiltmeters too. Short baseline inclinometers are the instruments usually used in seismic context, since are simple to be deployed on the field and easily manageable, but, on the other hand, they are not only very sensible to local inhomogeneities and anisotropies, but have even a lower resolution (typical values for short baseline tiltmeters is about 10^{-8} rad under ideal conditions, while somewhat smaller changes could be detected further lowering real resolution). The opposite extreme is represented by long baseline tiltmeters: the highest resolution is obtained through the use of an instrument hard to deploy, which needs a stable plain place, in stationary temperature conditions. In the current work, only long baseline tiltmeters will be taken in account.

1.2.1 – Long baseline tiltmeters

The first long baseline tiltmeters were built by Michelson in 1914. They are based on the communicating vessels physical principle, part of the Stevin's law related to hydrostatic pressure: two jars were connected together by one pipe of about 15 m in length, half-filled with fluid. The instrument was placed 2 m beneath the Earth's surface and closely tied to the ground, and the height changes in jars were measured by the use of a microscope. Differences in height of fluid's surface in relation with the edge of jars at both ends of the pipe were related with a ground tilt deformation (solid rotation of the Earth's free surface), which was consequently measured.

Tiltmeters can be installed both in deep tunnels or just on the Earth's surface.

Deep tunnels (more than 100 m in depth) installations are primarily used in subsurface laboratories to study Earth tides or oceanic charge. In the case of deep tunnels installations, the rocks shield the thermal wave (in some cases thermal changes can be as low as 0.01° C/year) allowing resolutions up to 10^{-9} rad and stabilities up to 10^{-6} rad/year. Thanks to these features, the most stable tiltmeters can record free surface waves and Earth's proper modes associated to the most energetic earthquakes.

Tiltmeters installed near the Earth's surface (or just on it) have usually lower resolutions, due to the thermal effects produced by the dilatation of fluids used to built them [*Beaven & Bilham, 1977*]: changes in temperature of just 0.2° C on a 4 m tube half-filled of fluid with a slope of 2% can generate statistical errors up to 0.1 μrad. Statistical errors like this will not occur for horizontal pipes.

Different kind of tiltmeters can be installed, according to the type of transducer chosen to measure fluid surface changes: optical or laser interferometers, magnetic probes, floating devices or pressure measuring devices. According to the type of transducer and the geometry of the system jar / pipes, three different kind of tiltmeters can be distinguished: filled pipe with external floating devices, half-filled pipe with external floating devices and filled pipe with central pressure measuring device [*Agnew, 1986*]: in Figure 1.3 the three different kind of tiltmeters are shown and compared.

Figure 1.3 – Comparison between the different categories of long baseline inclinometers installed near the earth's surface
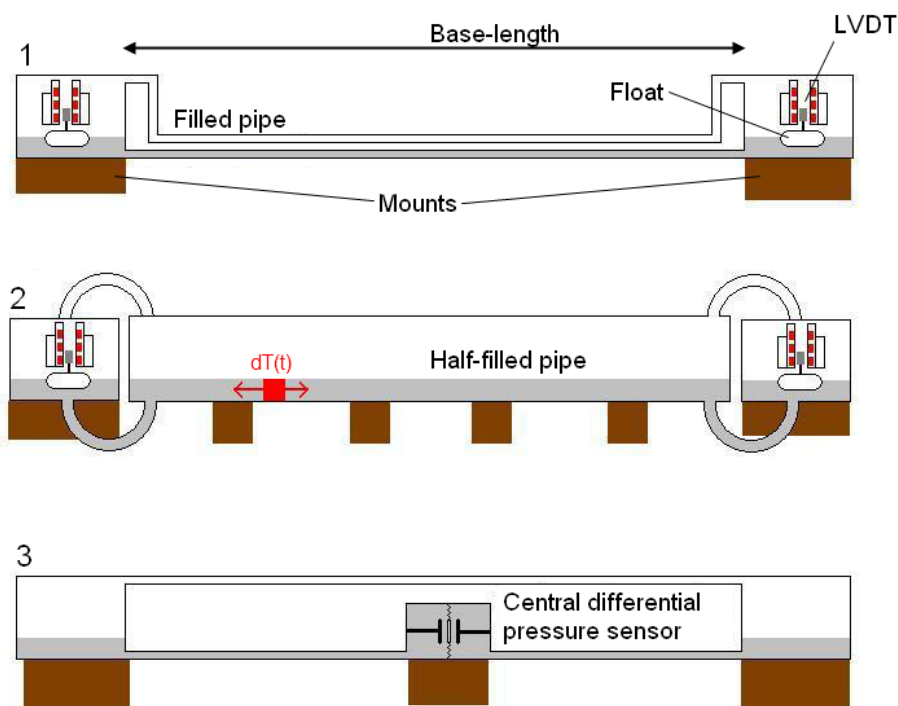
The first two kind of instruments are basically insensitive to uniform temperature variations since we look at the difference of level variations at the ends. Similarly, the third kind of instruments is insensitive to the same changes in temperature thanks to the central differential pressure sensor which will monitor changes in barometric pressure: uniform disturbances pose no problems indeed. This is also true for the problems of micro-leakage: the first two instruments shall be resistant to this type of problem, particularly the instrument no. 2 because it has a larger free surface of liquid. By cons, it must be more sensitive to the problems of evaporation.

It has been seen that the three instrument types are insensitive to uniform thermal perturbations. In opposition, if thermal changes occur locally on the pipes and supposing that all the pipes were put in places perfectly horizontally, only the third type of instruments (those with the central pressure sensor) will behave wrongly, and consequently will be perturbed: a fluid dilatation occurring in the left section of the instrument, in fact, will increase the height of the left section of the fluid's free surface, causing a change in left section's pressure on the central sensor, and this behavior will not re-equilibrate the fluid contained into the right section.

On the other hand, if the first kind of instrument was not installed correctly, presenting some ripples in its wall mounts (or support, depending on the type of installation), output will result in incorrect data when a local thermal perturbation occurs since fluid dilatation summed with pipe inclination generate a change in pressure gradient inside the fluid. Possible solution to this kind of problem are available and will be discussed in the following of the present work.

The second kind of instrument does not have this drawback because the expansion of the liquid due to local temperature changes affects uniformly the ends of the instrument. However, this type of installation

also requires a perfectly horizontal tube, and there are the same constraints for installation on site seen in the case of the first instrument. It seems that whatever is the type of instrument used, it is essential to have a horizontal line, which involves difficult installation in places where the topography is complex enough.

The first two instruments are insensitive to tube deformation, while this is not the case for the third one.

The instruments installed for this work use a floating device coupled with a displacement transducer which is used to measure the differential changes in height of the fluid free surface in order to obtain the tilt variation measured by the whole instrument, and its general design is very similar to the second instrument depicted into Figure 1.3.

1.2.2 – Precautions and limitations

One of the major problems for inclinometers is the stability of the supports which holds in place the instruments, particularly for short base inclinometers, but also for long baseline tiltmeters. These should minimally deform or move under the effect of local inhomogeneities in the risk of introducing instrumental drifts. It is therefore important to minimize the number of supports. Instruments 1 and 3 depicted into Figure 1.3 will be sensitive to vertical movements of the supports at the ends. The third instrument, in principle should be insensitive to local inclination of the central support.

In this case the second instrument depicted has higher benefits than the other two, since it could be installed with as low as 4 total supports, two placed to hold jars at both ends of the pipe, and two used to support the whole length of the pipe. This instrument is able to distinguish the movement of one of the jars over the other because of the large free surface of liquid in the tube half-filled, so it will be less sensitive to parasitic movements of the two jars. However, this instrument is sensitive to vertical movements of the supports at the ends of the tube half-filled. Finally it will be sensitive to the 4 support points.

Whichever the instrument installed, it is clear from this quick review of long baseline tiltmeters that it is of fundamental importance to be as much accurate as possible in installation of the instrument and in its coupling with the Earth's surface.

1.2.3 – Previous long baseline tiltmeters installations

The largest installation in the world for a long baseline inclinometer station in surface was performed at Piñon Flat Observatory in California (USA).

In 1981, following the work of Bilham at the Seismological Observatory of Ogdenbourg in New York, the Lamont Doherty Earth Observatory developed an instrument with the record dimensions of 535 m in length, using the principle of measurement by laser interferometry [*Bilham et al, 1979*]. This instrument was installed at a depth of only 1 m.

Later, the University of UCSD also redeveloped the measuring principle of Michelson and Gale for the installation of an instrument of the same size with a measuring system which was using white light interferometry [*Wyatt, 1982*]. This instrument is placed next to the previous one, but uses different supports, and is formed by a half-filled pipe. The fluid used is a mixture of water and ethylene glycol to increase the

viscosity of the liquid which will better attenuate waves resonance on the free surface of the fluid flowing in the half-filled pipe. These waves can be excited by the presence of moderate earthquakes.

Finally, the University of Cambridge developed an instrument with the central pressure sensor of the same length of both previous tiltmeters [*Horsfall & King, 1978*]. This latter instrument is placed on the same supports as the Bilham's instrument. Significant work has also been made to coupling both ends with the rock. The instruments are placed on pillars that are connected to stable points located at higher depths through invar bar extensometers using a magnetic transducer. In Figure 1.4 it is depicted a diagram similar to this type of system used in another installation in Mexico. The instrument developed by the UCSD uses a laser extensometer anchored at 26 m depth which can also check the stability of the pillars.

Figure 1.4 – Illustration of the method of coupling used at both ends of the half-filled pipe for the long baseline tiltmeters installed close Acapulco in the Mexican subduction zone.

V. Kostoglodov et al. 2002
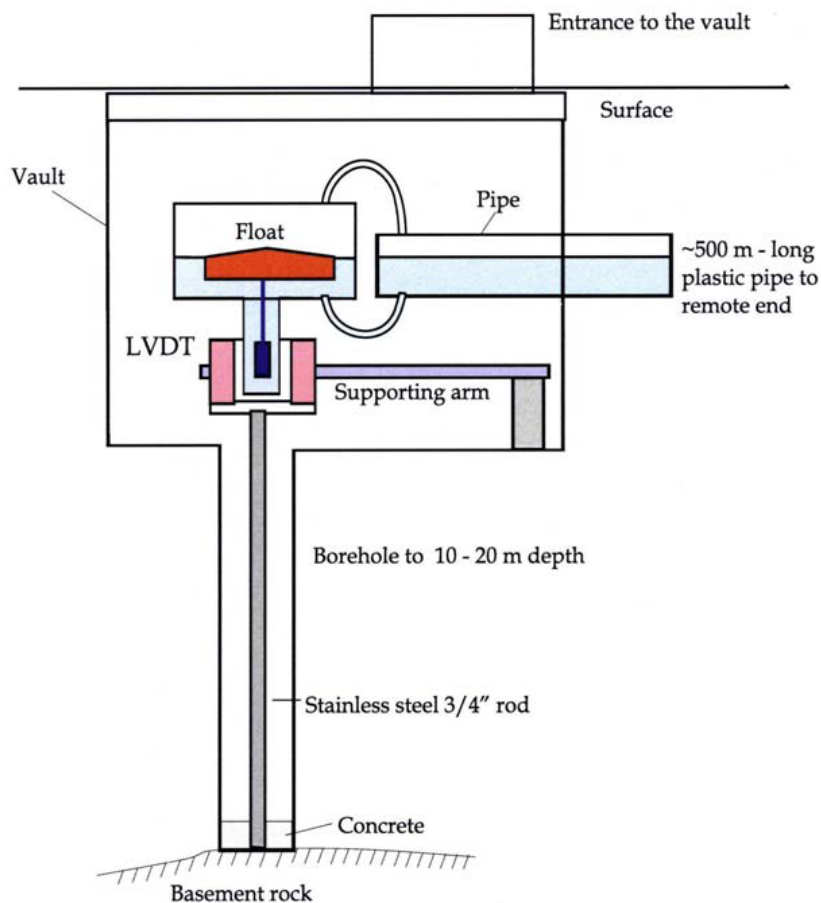
Chapter 2 – Theory underlying Earth's crust deformations

The theory underlying the Earth's crust deformations derives from some different branches of the physics: the theory of continuum, the fluid dynamics, the theory of gravitation, the thermodynamics. Of course, to fully understand how sensors and other devices used in the following of the current work operate, other details need to be explained.

The current chapter deals with all of the theoretical information needed in order to better understand and appreciate the physics that governs deformations.

2.1 – Continuum mechanics: theory of elasticity

The theory of elasticity is one branch of continuum mechanics, which studies systems whose properties are defined at all points in space.

The two main elements to deal with in theory of elasticity are the *stress* – the force experienced at every point in space – and the *strain* – the displacement caused by stress. Other properties, such as temperature, could be of interest in some specific case (for example, thermal variations may contribute to overall rock deformations, and hence should be taken in account for a more accurate model).

In general, theory of elasticity tries to solve equations to find functions of the form $\varphi(x, y, z; t)$, where *x*, *y*, *z* and optionally *t* are *independent* variables, whilst ϕ which could be a scalar of a vector, is a *dependent* variable.

2.1.1 – Stress tensor

Let's consider an infinitesimal element of volume *dV* for a homogeneous body. It is subject to external *body forces* which act on each atom of the body. For the Earth's interior, for example, these forces are the gravitational forces acting on the body as a whole. In addition to these forces, *contact forces* act on the external surfaces of the small volume too: these forces are produced by surrounding molecules through atomic or molecular interactions. An example of contact forces is represented by the pressure of a fluid

over a surface. The average contact force measured per unit area of a surface is known as **stress** (dimensionally, $N/_{m^2} = Pa$).

Let's now suppose to have an infinitesimal surface element *dS* having arbitrary orientation, and inside an homogeneous medium in static equilibrium, as depicted into Figure 2.1. The orientation of the small surface element can be specified through the use of the unit vector *n*, normal to the plane where *dS* lies. The force per unit area exerted through this surface by the molecules of the body on the side indicated by the direction of unit vector *n* is called traction and is represented by a vector $T = T(n)$, whose direction and magnitude depend on *n*.

Figure 2.1 – Explanation of the concept of traction
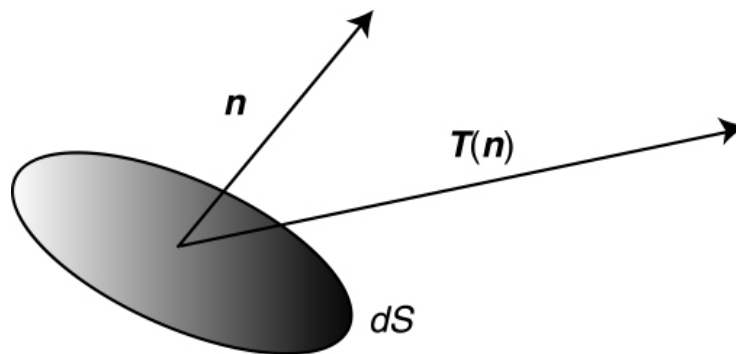
Obviously, in equilibrium the molecules present on the opposite side of *dS* exert a force $T(-n) = -T(n)$. The components of *T* normal and parallel to the plane of *dS* are called respectively normal stress and shear stress. In the case of a fluid shear stress is always zero, so we have: $T = -Pn$, where *P* is the pressure.

Figure 2.2 - Three vectors of traction are sufficient to describe the surface forces acting in a point of the body: they act through three orthogonal surface elements in a Cartesian coordinate system xyz.
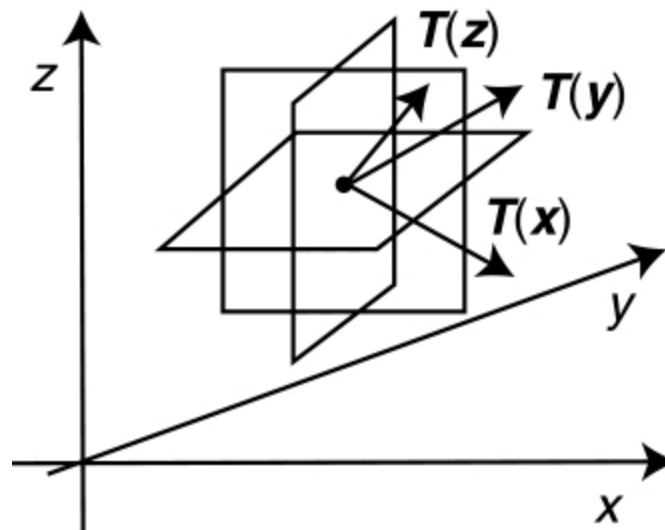

Now let's consider the system of surface forces that are exerted at any point of the body. The resultant of these forces can be decomposed into three components, which are represented by tension vectors acting on three infinitesimal surfaces orthogonal and normal to the axes in the considered point (Figure 2.2).

Alternatively, by letting $e_1 \equiv x$, $e_2 \equiv y$ and $e_3 \equiv z$, where (x, y, z) are the unit vectors associated with the Cartesian axes, we can describe the surface forces through a tensor of order 3. The stress tensor is the mathematical entity:

$$\tau_{ij} = T_i(e_j) \qquad (2.1.1)$$

In this notation the second index of the tensor indentifies the direction of the unit vector (i.e., the direction orthogonal to the surface), while the first index is the component of the traction vector. The stress tensor allows in turn to establish the traction exerted on any surface inside a body.

Figure 2.3 - Positive components of the stress tensor for four of the six faces of a cube.
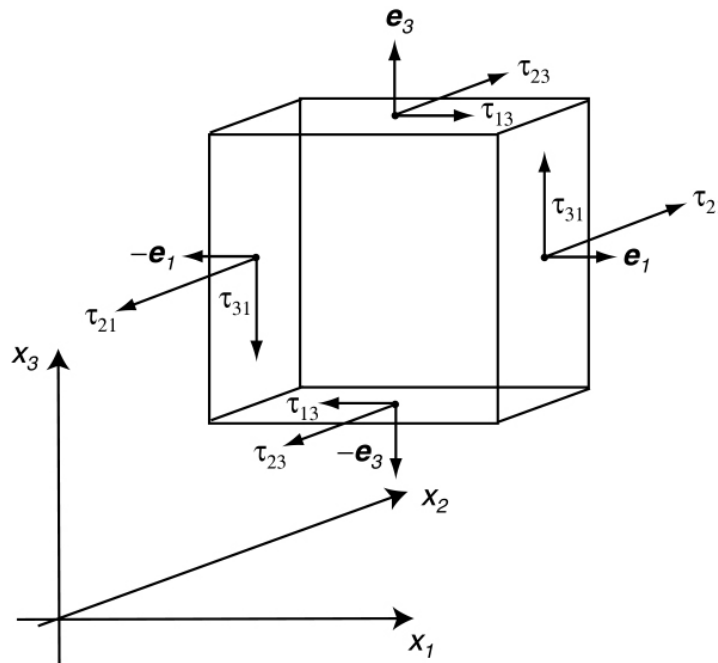
From Figure 2.3 it is clear how tensor components are oriented into a system of Cartesian axes. For example, on the side identified by the unit vector e_3, the element τ_{13} has a positive value when traction is exerted along the e_1 direction. Vice versa, on the opposite side – the one identified by the unit vector $-e_3$ – τ_{13}, τ_{23} and τ_{33} assume a positive value when traction occurs, respectively, in direction $-e_1$, $-e_2$ and $-e_3$, since $T_i(-e_j) = -T_i(e_j)$. This implies that:

$$\tau_{ij} = \tau_{ji} \qquad (2.1.2)$$

The equation (2.1.2) implies that the stress tensor is a symmetric tensor, since, for example, it is clear from Figure 2.3 that the couple generated by the components τ_{31} is opposed to the couple generated by the components τ_{13}. The equation (2.1.2), moreover, states another important property of the stress tensor: only six of the total nine components of the tensor are independent. So, the stress tensor con be seen as the linear operator that generates a traction vector T starting from a directional unit vector n. Given any set of components τ_{ij}, it is always possible to find a direction n for which there is no shear stress on a surface element normal to n. When this happens, n and $T(n)$ have the same direction:

$$T(n) = \lambda n = \tau n \tag{2.1.3}$$

where λ is a scalar. To find a direction **n** which satisfies (2.1.3) it must be solved, then, the following eigenvalue problem:

$$(\boldsymbol{\tau} - \boldsymbol{I}\lambda)\boldsymbol{n} = \boldsymbol{0} \tag{2.1.4}$$

where **I** is the identity matrix of order 3. This system of equations has a nontrivial solution only when:

$$\det(\boldsymbol{\tau} - \boldsymbol{I}\lambda) = 0 \tag{2.1.5}$$

The equation (2.1.5) is a third degree equation which admits three solutions, the eigenvalues λ_1, λ_2 and λ_3. Since τ is symmetric and real, the eigenvalues are real too. The three corresponding eigenvectors $\boldsymbol{n}^{(i)}$ are orthogonal and define the *principal axes* of stress. To compute the components of the stress tensor in the principal axes system, in which the associated matrix has only diagonal nonzero components, we apply a simple transformation of similarity. The diagonalization of the stress tensor, hence, is:

$$\boldsymbol{\tau}' = \boldsymbol{N}^T \boldsymbol{\tau} \boldsymbol{N} = \begin{bmatrix} \tau_1' & 0 & 0 \\ 0 & \tau_2' & 0 \\ 0 & 0 & \tau_3' \end{bmatrix} \tag{2.1.6}$$

where **N** is the matrix formed with the components of the three eigenvectors.

In the particular case in which it is $\tau'_1 = \tau'_2 = \tau'_3$, the stress field is called *hydrostatic* (in this case on the small element of volume *dV* acts only the hydrostatic pressure) and there are no surfaces for which the shear stress is different from zero. In a fluid the stress tensor can be written as:

$$\boldsymbol{\tau} = \begin{bmatrix} -P & 0 & 0 \\ 0 & -P & 0 \\ 0 & 0 & -P \end{bmatrix} \tag{2.1.7}$$

where *P* is the pressure. Stress has units of force per unit area, as already stated at the beginning of the current paragraph.

Hydrostatic pressure the increases rapidly with depth within the Earth, as shown in Table 2-1.

24

**Table 2-1 – Pressure variation with depth in the Earth**

Depth (Km)	Region	Pressure (GPa)
0-24	Crust	0-0.6
24-400	Upper Mantle	0.6-13.4
400-670	Transition Zone	13.4-23.8
670-2891	Lower Mantle	23.8-135.8
2891-5150	Outer Core	135.8-328.9
5150-6371	Inner Core	328.9-363.9

Shear stress, conversely, is much smaller going deep, where it is associated with movements of mantle convection and with the propagation of seismic waves. A significant static shear stress is found only in the brittle upper crust (10-100 MPa).

2.1.2 – Strain tensor

Now let's consider the problem of representing the deformation of a body subject to external forces. After a deformation, each point of the body, identified by a position vector $r = (x_1, x_2, x_3)$, undergoes a shift u from its original position $r_0 = r(t_0)$ at the initial time $t = t_0$.

Figure 2.4 – Geometry of deformation. The depicted example shows how deformation is associated to a relative shift *du* **between two points that were originally separated by the distance** *dr*.
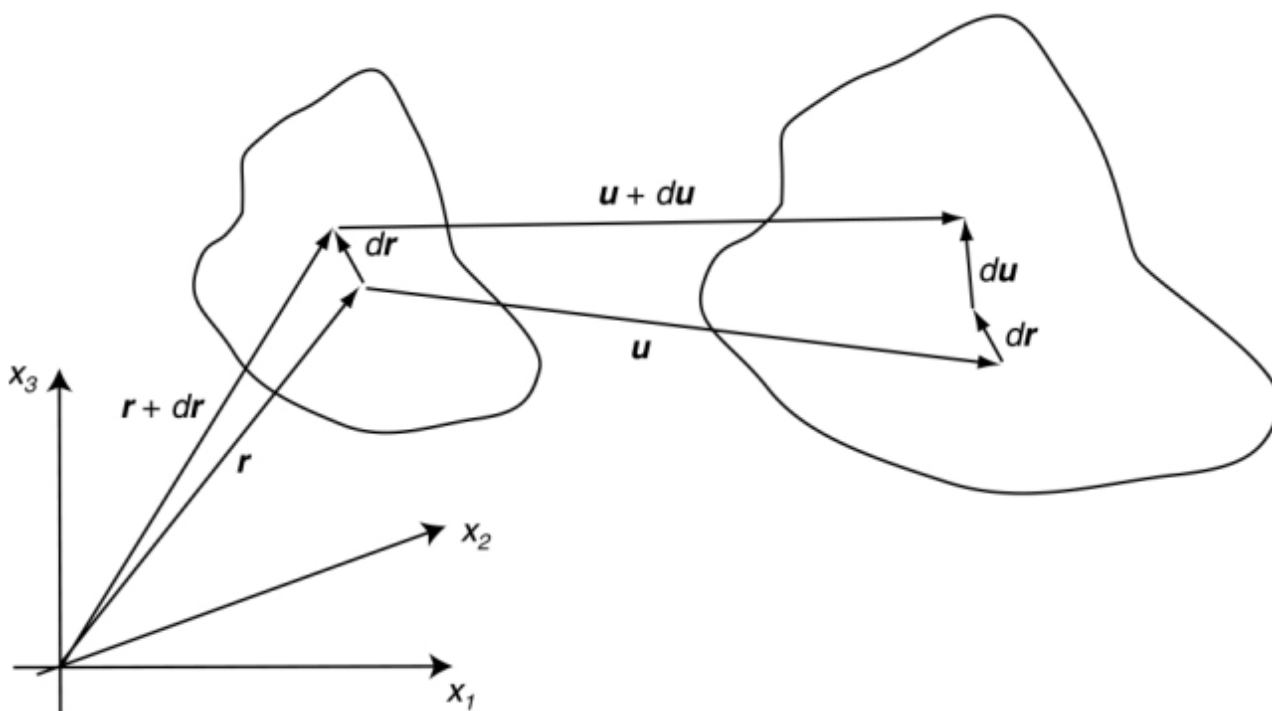
The position taken by the points of the rigid-body system with respect to the starting positions can so be represented with a vector field, the displacement field u:

$$u(r_0) = r - r_0 \tag{2.1.8}$$

The displacement field gives an absolute measure of the changes in position of the points internal to a continuous body. Moreover, changes in position can occur even without deformations. This occur when $|r - r'|$ is a constant for each couple of points **r** and **r'**.

Strain hence represents locally a measure of the relative variations of the displacement field, or rather of the spatial gradients of the field: for example, the extensional strain is defined as a change in length in respect to the original length of a body (e.g., a 100m long metal bar elongated up to 101m is subject to a displacement field which changes uniformly from zero to one meter along the bar, while the strain field is constantly equal to 0.01, or 1%).

Let's now consider the displacement **u** for a point which originally was located in **r**, as depicted in Figure 2.4. It is possible to describe the displacement for a neighboring point, having initially position **r + dr**, by expanding u in Taylor series expansion, choosing a first order approximation. What we get is:

$$u(r + dr) = u(r) + \sum_{i=1}^{3} \frac{\partial u}{\partial x_i} dx_i. \tag{2.1.9}$$

The relative displacement to the first order, so, is equal to:

$$du = \sum_{i=1}^{3} \frac{\partial u}{\partial x_i} dx_i \tag{2.1.10}$$

where the derivatives are computed in the point **r**.

The displacement can be divided into two different contributions: the deformation and the rigid rotation, which doesn't contribute to the actual deformation. For this purpose, it is possible to decompose the matrix $J_{ij} = \frac{\partial u_i}{\partial x_j}$ in a symmetrical half and an anti-symmetrical half:

$$J = \varepsilon + \omega \tag{2.1.11}$$

where the symmetrical strain tensor $\varepsilon_{ij} = \varepsilon_{ji}$ has components:

$$\varepsilon_{ij} = \frac{1}{2} \left(\frac{\partial u_i}{\partial x_j} + \frac{\partial u_j}{\partial x_i} \right) \tag{2.1.12}$$

while the rigid-rotations tensor **ω** is anti-symmetrical ($\omega_{ij} = -\omega_{ji}$) and has components:

$$\omega_{ij} = \frac{1}{2} \left(\frac{\partial u_i}{\partial x_j} - \frac{\partial u_j}{\partial x_i} \right). \tag{2.1.13}$$

The tensor ω describes a rigid-rotation of the body, but no deformations are associated with it. In fact, since ω is anti-symmetrical, the diagonal terms are all equal to zero, while, for the remaining six terms, there exist only three independent components. It is, hence, possible to form a vector Ω, with components:

$$\Omega_k = \sum_{ij=1}^{3} \frac{\varepsilon_{ijk}\omega_{ij}}{2} \tag{2.1.14}$$

where ε_{ijk} is the Levi-Civita tensor. Using the identity:

$$\sum_{k=1}^{3} \varepsilon_{ijk}\varepsilon_{stk} = \sum_{k=1}^{3} \varepsilon_{kij}\varepsilon_{kst} = \delta_{is}\delta_{jt} - \delta_{it}\delta_{js} \tag{2.1.15}$$

it is easy to prove that:

$$\sum_{k=1}^{3} \varepsilon_{ijk}\Omega_k = \sum_{stk=1}^{3} \frac{\varepsilon_{ijk}\varepsilon_{stk}\omega_{st}}{2} = \frac{(\omega_{ij} - \omega_{ji})}{2} = \omega_{ij} \tag{2.1.16}$$

and so it results that:

$$\sum_{j=1}^{3} \omega_{ij}dx_j = \sum_{jk=1}^{3} \varepsilon_{ijk}\Omega_k dx_j = -(\mathbf{\Omega} \times d\boldsymbol{r})_i \tag{2.1.17}$$

This implies that the second term in equation (2.1.11) represents a rigid rotation around the Ω axes, so this term doesn't imply any deformation.

On the other hand, the first term implies a net deformation, and it represents the Strain Tensor. All of its components are dimensionless and depend from the derivatives of the displacement field. These components are of two different types.

The diagonal components determine the way in which displacement along a coordinate axes varies along it: for example, if the displacement occurs only along the x_1 direction ($u_2 = u_3 = 0$) and u_1 changes only along this specific direction, then the only term non-null of the strain tensor is ε_{11}. If $\partial u_i / \partial x_i > 0$ then there is extension along the x_i axes, while if $\partial u_i / \partial x_i < 0$ there is a contraction in length. If the diagonal term ε_{ii} is constant inside a rigid body that is deformed, it represents the change in length per unit length in x_i direction.

The generic non-diagonal terms in the strain tensor, however, represent the changes, along one axes, of the displacement along one different axes (for example, the changes of u_1 when moving along the x_3 axes).

Just as in the case of the stress tensor, even the strain tensor can be represented in a coordinate system where only the diagonal components are non-null. Let's suppose that the displacements in a neighborhood

of a point r can be described by pure deformation ($\boldsymbol{\omega} = \boldsymbol{0}$). In this case the equation (2.1.10) can be re-written as:

$$d\boldsymbol{u} = \boldsymbol{\varepsilon}(r)dr. \tag{2.1.18}$$

The principal strain axes can then be calculated requiring that the variation of the displacement field $d\boldsymbol{u}$ has the same direction of the change of position dr:

$$d\boldsymbol{u} = \lambda dr = \boldsymbol{\varepsilon}(r)dr. \tag{2.1.19}$$

The three eigenvalues of the equation (2.1.19) are known as principal strains ε_1, ε_2 and ε_3. Apart the special case in which $\varepsilon_1 = \varepsilon_2 = \varepsilon_3$ (known as *hydrostatic strain*), an amount of shear strain is always present.

The trace of the strain tensor

$$\Delta = \sum_{k=1}^{3} \varepsilon_{kk} = \sum_{k=1}^{3} \frac{\partial u_k}{\partial x_k} = \nabla \cdot \boldsymbol{u} \tag{2.1.20}$$

is called *dilatation* and is equal to the divergence of the displacement field $\boldsymbol{u} = \boldsymbol{u}(r)$. Dilatation determines, as a consequence of a deformation, the change in volume per unit volume. In fact, into the principal strain axes system, a small element of the body with volume $dV = dx_1 dx_2 dx_3$, becomes the volume:

$$dV' = \left(1 + \frac{\partial u_1}{\partial x_1}\right) dx_1 \left(1 + \frac{\partial u_2}{\partial x_2}\right) dx_2 \left(1 + \frac{\partial u_3}{\partial x_3}\right) dx_3 \cong \left(1 + \sum_{k=1}^{3} \frac{\partial u_k}{\partial x_k}\right) dx_1 dx_2 dx_3 = $$

$$= \left(1 + \sum_{k=1}^{3} \frac{\partial u_k}{\partial x_k}\right) dV = (1 + \Delta)dV \tag{2.1.21}$$

Therefore the relative change in volume for the point in question is given by:

$$\Delta = \frac{dV' - dV}{dV} \tag{2.1.22}$$

and the rotor of the displacement field is:

$$\nabla \times \boldsymbol{u} = \left(\frac{\partial u_3}{\partial x_2} - \frac{\partial u_2}{\partial x_3}\right) \boldsymbol{e_1} + \left(\frac{\partial u_1}{\partial x_3} - \frac{\partial u_3}{\partial x_1}\right) \boldsymbol{e_2} + \left(\frac{\partial u_2}{\partial x_1} - \frac{\partial u_1}{\partial x_2}\right) \boldsymbol{e_3}. \tag{2.1.23}$$

Comparing the equation (2.1.13) with the equation (2.1.23) shows that the rotor of the displacement field $\boldsymbol{u}$ is non-null only if $\boldsymbol{\omega}$ is not identically null, or when a small amount of rigid rotation is present.

2.1.3 – Relationship stress-strain

In an elastic medium, stress and strain are related through a linear constitutive relationship whose more general form is:

$$\tau_{ij} = \sum_{k=1}^{3} \sum_{l=1}^{3} c_{ijkl} \varepsilon_{kl} \tag{2.1.24}$$

The tensor c_{ijkl} is known as the elastic tensor, and the law (2.1.24) is known as Hooke's Law for an elastic medium. It assumes that the medium is perfectly elastic, so there is no energy loss or attenuation in response during deformation. The elastic tensor is a fourth order tensor with 81 (3^4) components. Remembering the symmetry of stress and strain tensors, and introducing some thermodynamic constraints, it can be shown that only 21 components are linearly independent. Moreover, usually the characteristics of a medium change with direction (anisotropic medium), while for isotropic mediums their features don't depend from the chosen direction: using this constraint when referring to the Earth's interior (a good first order approximation in many cases), the elastic tensor is invariant for rotations and the number of linearly independent parameters lowers to only two, related by the equation:

$$c_{ijkl} = \lambda \delta_{ij} \delta_{kl} + \mu \left(\delta_{il} \delta_{jk} + \delta_{ik} \delta_{jl} \right) \tag{2.1.25}$$

where λ and μ are known as Lamè parameters, while the δ_{ij} is the Kronecker delta function. The Lamè parameters are related with the propagation velocity of seismic waves.

Using the equation (2.1.25), the Hooke's law becomes:

$$\tau_{ij} = \lambda \delta_{ij} \sum_{k=1}^{3} \varepsilon_{kk} + 2\mu \varepsilon_{ij} = \lambda \delta_{ij} \Delta + 2\mu \varepsilon_{ij} \tag{2.1.26}$$

The Lamè parameters, hence, determine in a complete way the linear relationship between stress and strain in an isotropic medium. The parameter μ, particularly, is known as shear modulus and represent a measure of the resistance of the material to shear deformations. The parameter λ, on the other hand, doesn't have a simple physical meaning.

Three more constants are used to describe the mechanical behavior of isotropic bodies: the Young modulus, the uniform compression modulus and the Poisson's ratio.

The Young modulus E represents the ratio between extensional stress and the associated extensional deformation for a cylinder pulled from both sides. Its value is:

$$E = \frac{(3\lambda + 2\mu)\mu}{\lambda + \mu} \tag{2.1.27}$$

The uniform compression modulus k gives a measure of how much incompressible a material is, and it is defined as the ratio between the applied hydrostatic pressure and the consequent volume change:

$$k = \lambda + \frac{2}{3}\mu \tag{2.1.28}$$

Finally, the Poisson's ratio represents the ratio between lateral contraction of a cylinder pulled from both sides and its longitudinal extension:

$$\sigma = \frac{\lambda}{2(\lambda + \mu)}$$

(2.1.29)

Apart the dimensionless Poisson's ratio, all of the other parameters are expressed in Pa.

2.2 – Definition and measure of the tilt

To define the slope of a given surface, we must define a reference frame in space. By definition a pendulum is naturally directed along the acceleration vector g, which defines the local vertical. We will therefore take as a vertical reference the same direction defined by the acceleration vector *g*. The direction of the two other components of the reference frame is perpendicular to the vertical, hence them define the horizontal surface: they lies therefore along a free surface of a liquid. Then, one possibility to measure the inclination of a surface is to identify the position of the free surface of a liquid relative to the surface. This is the fundamental principle of the hydrostatic long baseline inclinometer.

All inclinometers measure the change of angle a between the direction defined by the gravity and the normal to the Earth's surface where the inclinometer was installed. We therefore measure the variation of angle between the geoid, or the corresponding equipotential surface, and the base of the instrument.

The change of inclination is measured in a reference frame defined by the geoid and vertical. The geoid defines the main horizontal directions *x* and *y*, while the acceleration vector *g* defines the vertical *z [Horsfall 1977]*. An long baseline inclinometer measures this slope along a base, that can range from a few meters to several hundred meters.

On a long baseline inclinometer, the variation of tilt angle between the base formed by the end-points and the geoid generates the movement of a portion of liquid from a pot to the other. This movement causes a variation in height of liquid positive in the first pot and negative in the second one. These variations in height, equal and opposite in sign at each end, are measured by sensors designed almost entirely of silica.

Figure 2.5 – Effects of the geoid and of the Earth's crust deformation. In (1) it is represented the case without deformation: in this case the geoid surface (dashed line) is parallel with the fluid's free surface. In (2) it is depicted the effect of tilt: in this case α represents the angle between the geoid surface (dashed line) and the fluid's free surface (light blue plane), which acts as a horizontal reference.
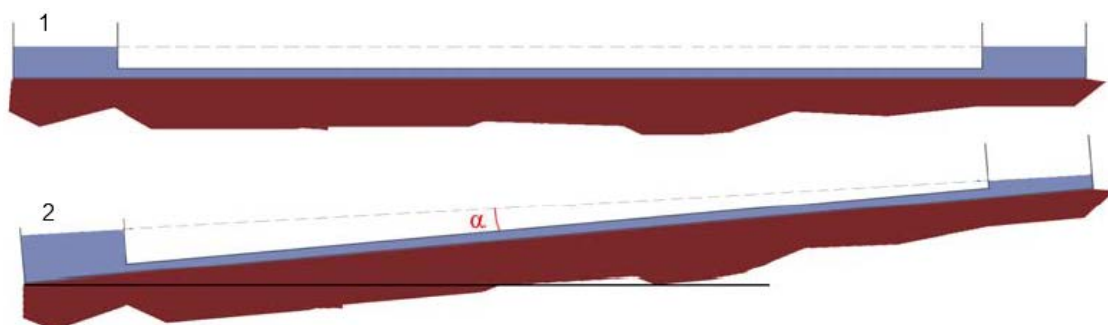
The signal of interest coming from a hydrostatic inclinometer of length *l* is the subtraction of the two signals +*h* and −*h*. From these two values it is possible to establish the tilt of the crust in respect to the equipotential surface identified by the fluid's free surface, starting from the equation:

$$\tan\alpha = \frac{dh}{l} = \frac{\left(+h - (-h)\right)}{l} = \frac{2h}{l} \cong \alpha \qquad (2.2.1)$$

The approximation reported in equation (2.2.1) is valid for small angles (as the case of crustal tilt deformations), while the angle α is represented in Figure 2.5.

The tilt and strain quantities are very similar *[Agnew, 1986]*, and it is not easy to separate them: both are measures of deformation, even if inclination, however, introduces other effects. It establishes the general expression of the tilt vector $\omega = \omega_D + \omega_U$ (according to a purely kinematic description using the tensor notation *[Malvern, 1969]*, where ω_D is the sum of the tilt deformations due to the elastic deformation of the Earth, while ω_U is the change of tilt produced by the lunisolar tidal potential, *[d'Oreye, 2003]*).

The final expression for ω is:

$$\boldsymbol{\omega} = (\boldsymbol{z_0} \cdot \boldsymbol{d_0})(\boldsymbol{d_0} \cdot \boldsymbol{\varepsilon}) - \boldsymbol{d_0}(\boldsymbol{z_0} \cdot \boldsymbol{d_0} \cdot \boldsymbol{\varepsilon})$$

$$+\boldsymbol{z_0} \times (\boldsymbol{d_0}(\boldsymbol{s} \cdot \boldsymbol{d_0}) - \boldsymbol{s}) - \frac{\nabla U_1 - \boldsymbol{z_0}(\boldsymbol{z_0} \cdot \nabla U_1) + \ddot{\boldsymbol{x}} - \boldsymbol{z_0}(\boldsymbol{z_0} \cdot \ddot{\boldsymbol{x}})}{g} \qquad (2.2.2)$$

This equation has five terms, two involving the strain tensor ε, one the rotation *r*, one the change of the lunisolar horizontal potential U_1 and the last produced by the horizontal acceleration $\ddot{x}$. The slope will be affected by all these terms. The vector *s* is defined below.

By adopting a fixed coordinate system, it is possible to propose a Lagrangian description of the relative position of two particles *r(X₁, t)* and *r'(X₂, t)* of an isotropic elastic rigid body. The distance between the two particles is |*dr*|, as seen in Figure 2.4, while $\boldsymbol{d_0} = \frac{dr}{|r-r\prime|}$ is the unit vector directed along the *dr* direction.

Let's now assume that the particle displacements are infinitesimal: they will form at time t the basis *d*, and ${|u|}/{l} \ll 1$, it also requires that $u = r \cdot \nabla u$, this should be verified regardless of the direction of *u*, ∇u must be substantially constant for a distance *l* around the origin X_1 of *r*. This condition implies that we have a uniform strain tensor, even if in practice this is not always satisfied.

Starting from the definition of strain tensor ε stated in (2.1.12), and using the infinitesimal rotation vector:

$$\boldsymbol{s} = \frac{1}{2}\nabla \times \boldsymbol{u} \qquad (2.2.3)$$

it is possible to choose as reference direction the unit vector $\boldsymbol{z_0}$ oriented along the local vertical defined from the vector lunisolar attraction potential ∇U_0, where

$$z_0 = \frac{\nabla U_0}{|\nabla U_0|} \equiv \frac{\nabla U_0}{g} \tag{2.2.4}$$

Under some specific conditions, the equation (2.2.2) can be simplified.

If T is the stress tensor, then on a free surface of a body, $n \cdot T = 0$, where n is the normal to the surface. This is the case when installing a device on the Earth's surface. For an isotropic elastic material this implies that $n \cdot \varepsilon = 0$, and if the normal in respect with the baseline on the free surface equals the generic unit vector, $d_0 = n$, the inclination ω_D produced by the deformation reduces to:

$$\omega_D = z_0 \times (d_0(r \cdot d_0) - r) \tag{2.2.5}$$

and the expression for ω becomes:

$$\omega = z_0 \times (d_0(r \cdot d_0) - r) - \frac{\nabla U_1 - z_0(z_0 \cdot \nabla U_1) + \ddot{x} - z_0(z_0 \cdot \ddot{x})}{g} \tag{2.2.6}$$

An inclinometer placed on the free surface is subject to an inclination that is therefore only proportional to the rotation of the free surface, to horizontal variations of the lunisolar potential and to the local horizontal accelerations of the free surface. In the following of the current work, we won't be interested in the horizontal acceleration component, since this term acts only when the inclinometer is subject to horizontal accelerations produced by seismic waves.

It is, then, possible to relate the equation (2.2.1) with the equation (2.2.6), in the following way:

$$\frac{+h - (-h)}{l} = \omega = z_0 \times (d_0(r \cdot d_0) - r) - \frac{\nabla U_1 - z_0(z_0 \cdot \nabla U_1)}{g} \tag{2.2.7}$$

2.2.1 – Units of measurement

The unit of measurement used in order to measure an angle variation is the degree (°). However, since the measures that we perform with our inclinometers have very small angle variations, a subunit of the degree is often used, it is the arcsecond as *1° = 60' = 3600 a sec*. Usually, the unit chosen to measure angle variations due to Earth's crust deformations is the radians, since it can be quickly connected to the vertical deformation. For inclinometers, it belongs to the International System (IS). Arcsecond and radian can be easily connected: since *2π rad = 360°*, we easily obtain that *1* rad = *206264.806247* a sec or *1* μrad = *206.264806247* ma sec.

There is no sign convention to determine in which way it is changing the tilt with an inclinometer. In usual installations, we always have two main directions: NS and EW directions. For the NS direction, so we have two possible directions, north or south, as well as EW, were there are the west and the east directions. For values of inclinations that will be presented in the following, every time we will state the direction of the tilt. For example when the inclinometer tilts NS positively to the north, it means that the N side subsides in respect to the S side.

2.3 – Tides-induced deformations

The combined effect of the gravitational interaction between Earth and other celestial bodies and the centrifugal force due to the revolution of Earth around the center of mass of the system consisting of the Earth itself and these celestial bodies, results in a viscoelastic deformation involving the lithosphere, hydrosphere and atmosphere. This deformation is known as tide: the largest contribution is provided by lunisolar attraction and features characters periodic or almost periodic: it is modulated in time as the Sun and Moon have different velocities and thus the combination of their distances from Earth is variable. The motion of the celestial bodies is described in an approximate geocentric system: although the mass of the Sun is much larger than the mass of the Moon, the attraction that it exerts on the Earth is about twice the solar attraction, since the Moon is closest to Earth. If we consider only lunar attraction, we would have only one major tide at the lunar zenith on a given meridian, but this won't justify the reason why a swelling would be present at antipode. The previously appointed centrifugal force due to revolution of the Earth-Moon system is the cause of this deformation. Because of these forces, Earth changes its shape: these deformations are governed by the same laws of forces that cause them. The laws that govern these changes, other than instantaneous amplitudes, are calculated in the various components and with a high degree of accuracy, since are known the orbits of Earth and Moon and the values of their masses.

It is important to study tides, since this is the only deformation phenomenon for the Earth for which it is possible to calculate almost exactly the forces. Hence the study of Earth tides – the tides which concern the crust – is important for the determination of some physical properties of the Earth, and may have various applications in geophysics and geodynamics. It is aimed to know the components of the tidal field and their deviation from theoretical models: these deviations may be indicative of crustal deformation and mass redistribution in the subsurface. Thanks to these properties of the tidal signals, they can be used as a comparison for calibration of instruments.
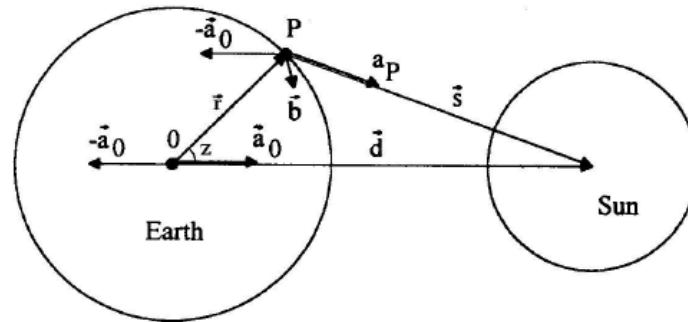
2.3.1 – Tidal acceleration

Any point on the Earth's surface is subject to four forces:

- Gravitational attraction due to Earth's own mass
- Centrifugal force due to Earth's rotation around its own axis
- Gravitational attraction due to other celestial bodies
- Centrifugal force due to the revolution of the system Earth-other celestial bodies around their common center of mass

The latter two forces define the tidal acceleration, which is responsible of tides.

Let's consider now the generic two-bodies system (in our case, this is a good representation for the Earth-Sun or the Earth-Moon systems), as the one depicted into Figure 2.6.

Figure 2.6 – Example of two-bodies system. In this case Earth and Sun are represented schematically: every element in the picture isn't in scale.

Let's consider the point P on the Earth's surface: tidal acceleration measures the sum of acceleration $\boldsymbol{a_p}$ produced by the Sun in P, and the orbital acceleration $\boldsymbol{a_o}$ due to the Earth's motion around the center of gravity (CG) of the two-bodies system. The orbital acceleration approximately equals the gravitational acceleration due to the Earth's mass with opposite sign, and is the same for each point on Earth's surface. The tidal acceleration vector $\boldsymbol{b}$, from Newton's law, is:

$$\boldsymbol{b} = \boldsymbol{a_p} + \boldsymbol{a_o} = \frac{GM}{s^2}\boldsymbol{s} - \frac{GM}{d^2}\boldsymbol{d} \qquad (2.3.1)$$

where M is the celestial body's mass (in this case, Earth's mass), $\boldsymbol{s}$ unit vector of topocentric distance, $\boldsymbol{d}$ unit vector of geocentric distance, $\boldsymbol{b} = \boldsymbol{0}$ in the center of the Earth. Equation (2.3.1) represents the tidal acceleration on Earth's surface due to Earth's rotation around the Sun (or the Moon); this is a vector directed towards the Earth's center, whose length represents the magnitude of the gravity in the chosen point P, and whose direction defines the vertical in that point. However, these elements aren't constant, since solar (or lunar) attraction in the chosen point P changes in time. Of course, even planets affect the Earth's gravitational field, and therefore even planets contribute to tidal acceleration, which should then be computed as a sum of contributes for each celestial body taken in account (Sun, Moon, and each single considered planet), as well as the acceleration produced by the Earth's motion around the CG of the system, but it is clear that – because of their distances and of their relatively small masses – the contributes given by planets is smaller than those given by Sun and Moon, and hence, at a first approximation, these contributes can be discarded. Tidal acceleration induces a viscoelastic deformation of the Earth.

2.3.2 – Tidal potential

Earth tides are the only geophysical phenomena for which it is possible to calculate the forces acting on the system, so it is important to know the form of the tidal potential. In the following, we will write the tidal potential for an Earth's model that has the form of a rotational ellipsoid with mechanical and rheological parameters with the same symmetry. Consider a point P on the Earth's surface: its position can be expressed, in a polar coordinates system with origin in the center of the Earth, as $P(r, \phi, \lambda)$, where r is the radius vector, ϕ is the latitude, λ the longitude. Let's be d the distance of this point from the CG of the two-bodies system. The potential $W(P)$ is thus defined so that:

$$b = \nabla(W) = \frac{\partial W}{\partial r} \tag{2.3.2}$$

with the additional condition that $W = 0$ in $r = 0$.

The potential W for which the equation (2.3.2) is satisfied (*[Wenzel, 1997]*) is:

$$W = GM \left(\frac{1}{s} - \frac{1}{d} - \frac{r \cos z}{d^2} \right) \tag{2.3.3}$$

where z is the geocentric zenith angle (the angular distance of any celestial body from the zenith) and s is the distance between the point P and the perturbing body.

Since W is a function of distance, it satisfies the Laplace equation, and hence it can be expanded in spherical harmonics, as is the case of the gravitational potential, where the angular dependency is now expressed by z, that is the zenithal distance of the perturbing body from the point P: it is a function of the *hour angle* (the angular distance, measured westward along the celestial equator, between the celestial meridian of the point P and the hour circle passing through a celestial body) $H(P)$. The equation (2.3.3), hence, becomes:

$$W = GM \sum_{n=2}^{+\infty} \frac{r^n}{d^{n+1}} P_n(\cos z). \tag{2.3.4}$$

The expansion (2.3.4) depends not only from the n-th degree Legendre polynomial P_n, but even from the ratio r/d. This ratio is equal to 1.6×10^{-2} for the Moon and about 4×10^{-5} for the Sun. The expansion (2.3.4) is rapidly convergent. The tidal potential is usually coded into catalogues where it is chosen $n_{max} = 6$ for the Moon and $n_{max} = 3$ for the Sun. The element that most contributes to the tidal potential is the 2-nd degree term, which represents the 98% of W. If we choose $n = 2$, the tidal potential (2.3.4) becomes:

$$W = \frac{GM}{2} \left[\frac{r^2}{d^3} (3 \cos^2 z - 1) \right] \tag{2.3.5}$$

Instead of using a local coordinates expansion, it is usually chosen an astronomical coordinates expansion to link the zenithal angle with the geocentric coordinates of the point P (ϕ and λ measured westward) and the equatorial coordinates (right ascension α and declination δ), using the spherical equivalence:

$$\cos z = \sin \varphi \sin \delta + \cos \varphi \cos \delta \cos H(P) \tag{2.3.6}$$

where $H(P)$ is the function:

$$H(P) = H - \lambda(P) = \omega t' - \alpha - \lambda(P) \tag{2.3.7}$$

and where H is the hour angle of the external body, t' is the sidereal time (measured by the rotation of the Earth with respect to the stars, rather than relative to the Sun) for a specific meridian (e.g., in this case for

35

the Greenwich meridian), ω is the sidereal period (the temporal cycle that it takes a planet to make one full orbit, relative to the stars). In Figure 2.7 it is represented the coordinates system used.

Figure 2.7 – Spherical astronomical trigonometry: in the current picture is schematically visualized the used spherical coordinates system.
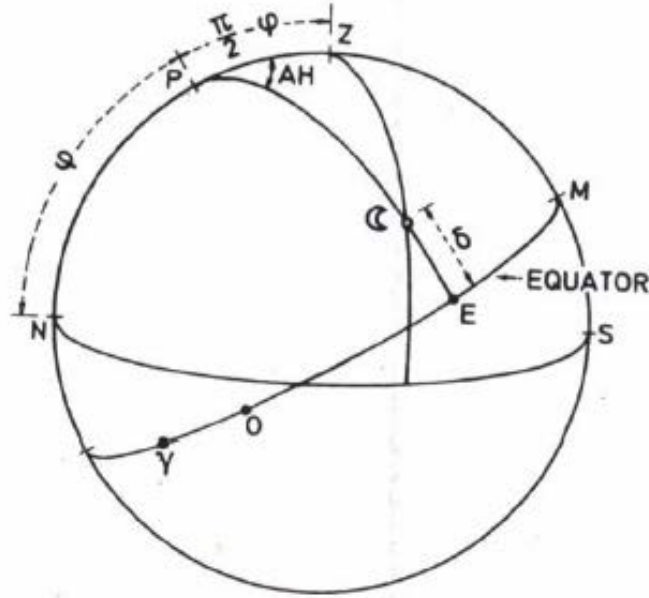
By substituting (2.3.6) in (2.3.4), we have:

$$W(P) = \sum_{l=2}^{+\infty} \sum_{m=0}^{+\infty} W_{lm} r^l P_l^m(\sin \delta) P_l^m(\sin \varphi) \cos mH(P) \tag{2.3.8}$$

where:

$$W_{lm} = \frac{2(l-m)!}{(l+m)!} \frac{GM}{d^{l+1}} \quad (m = 1, ..., l); \ \ W_{l0} = \frac{GM}{d^{l+1}} \tag{2.3.9}$$

and

$$\cos mH(P) = \cos mH \cos m\lambda + \sin mH \sin m\lambda \tag{2.3.10}$$

By expanding the equation (2.3.8) to the 2-nd order, we have the Laplace expansion in three spherical harmonics families:

$$W_2(P) = \frac{3}{4} GM \frac{r^2}{d^3} \Big\{ \cos^2 \varphi \cos^2 \delta \ 2H(P) + \sin 2\varphi \sin 2\delta \cos H(P)$$
$$+ 3 \left(\sin^2 \varphi - \frac{1}{3} \right) \left(\sin^2 \delta - \frac{1}{3} \right) \Big\} \tag{2.3.11}$$

Equation (2.3.11) can be further simplified so that the three constituent of the tidal potential can be dealt with individuality. Let's simplify the equation (2.3.11) as:

$$W = S + T + Z \qquad (2.3.12)$$

where

$$S = \left(\frac{3}{4}GM\frac{r^2}{d^3}\right)\left(\cos^2\varphi \cos^2\delta\, 2H(P)\right) \qquad (2.3.13)$$

$$T = \left(\frac{3}{4}GM\frac{r^2}{d^3}\right)\left(\sin 2\varphi \sin 2\delta \cos H(P)\right) \qquad (2.3.14)$$

$$Z = S = 3\left(\frac{3}{4}GM\frac{r^2}{d^3}\right)\left(\sin^2\varphi - \frac{1}{3}\right)\left(\sin^2\delta - \frac{1}{3}\right) \qquad (2.3.15)$$

Represents, respectively, the *sectorial* tide (equation (2.3.17)), the *tesseral* tide (equation (2.3.18)), and the *zonal* tide (equation (2.3.19)). A visual representation of these tidal families is depicted into Figure 2.8.

Figure 2.8 – Three types of tides: from left to right, sectorial tide, tesseral tide and zonal tide.
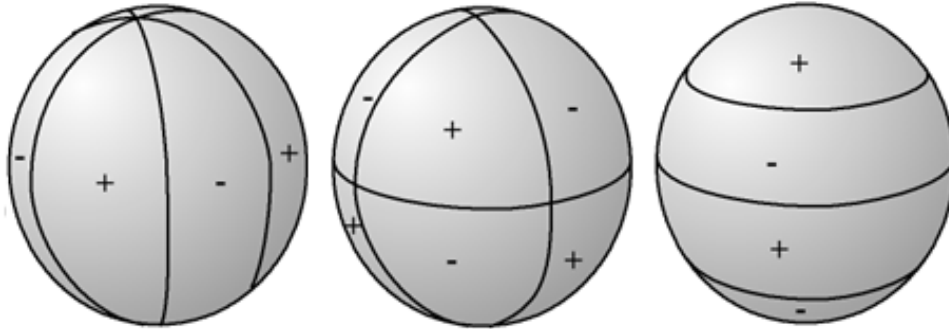
Then, starting from the general expression for the tidal potential, we have obtained the different harmonic representations of tides.

The leftmost image in Figure 2.8 represents the sectorial tide: it has nodal lines (lines where the function is zero) only in the meridians situated 45° to either side of the meridian of the perturbing body. These lines divide the spherical surface into four sectors where the function is alternately positive and negative. The areas where the function W is positive are those of high tides, while the negative areas are those of low tides. This function is hence known as the *sectorial function*, the period of the corresponding tides is *semidiurnal*, and their amplitude has a maximum at the equator when the declination of the perturbing body is zero, while the polar tidal amplitudes are zero. Variation of mass distribution at the Earth's surface subject to the sectorial distribution do not modify either the position of the pole of inertia or the major moment of inertia *C*, which determines the speed of rotation of the Earth. The sectorial tides are at least partly responsible for the secular retardation of the Earth's speed of rotation owing to internal friction and energy dissipation. The amount of energy stored in the internal tide may range from 5×10^{22} erg to 3.5×10^{24} erg.

The second tide, depicted as the central image in Figure 2.8, has as a nodal line a meridian (90° from the meridian of the perturbing body) and a parallel, namely, the equator. It is a *tesseral function* which divides the sphere into areas which change sign with the declination of the perturbing body. The corresponding

tidal period is *diurnal* and the amplitude is maximum at latitude 45°N and 45°S when the declination of the perturbing body is maximum; the amplitude is always zero at the equator and the pole. The variation of mass distribution at the surface of the earth following the tesseral distribution produce positional oscillations of the inertial pole but not of the major moment of inertia *C*. The resultant perturbing potential of polar motion has the same form. This distribution corresponds to the precession-nutational couple which, acting on the Earth's equatorial bulge, tends to tilt the equatorial plane against the ecliptic. A diurnal tesseral wave of the harmonic development of the tidal potential corresponds to each stage in the development of the precession-nutational couple. The effect of this couple may be that the fluid core rotates relative to the mantle.

The last function is the *zonal function* (depicted in Figure 2.8, the rightmost image), which is dependent only on latitude. Its nodal lines are the parallels +35°16' and -35°16'. Since it is only a squared sine function of the declination of the perturbing mass, its period will be 14 days for the Moon, and 6 months for the Sun (*long-periodic*). The variation of the mass distribution at the surface of the Earth conforming to the zonal distribution do not produce any drift of the inertial pole, but do affect the major moment of inertia *C*. We may therefore expect some fluctuations in the Earth's speed of rotation corresponding to the periods given above. The equipotential surface will be lowered 28 cm at the pole and raised 14 cm at the equator. The effect of this permanent tide is a slight increase of the Earth's oblateness, since the difference between the major and minor axes of the terrestrial ellipsoid is 21.37 km.

Figure 2.9 – Coordinate system used in order to describe the tidal components.
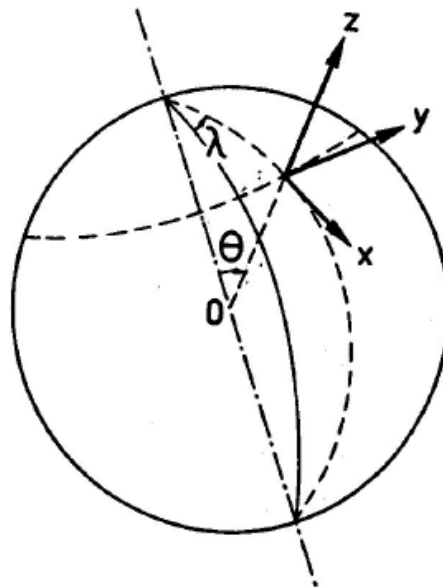
Let's now consider a coordinate system as the one depicted into Figure 2.9. The components of the tidal force are obtained starting from the partial derivatives of the potential in respect with the corresponding variables:

$$O_z = -\frac{\partial W}{\partial r}$$

$$O_X = -\frac{\partial W}{r\partial\varphi}$$

(2.3.16)

$$O_Y = -\frac{\partial W}{r\cos\varphi\,\partial\lambda}$$

where O_Z is the vertical component, O_X is the horizontal component oriented along the NS direction, O_Y is the horizontal component oriented along the EW direction.

Along the O_Z axes acts the gravitational acceleration: the force directed along this axes represents the changes in gravity in the selected point. The other two components represent local changes in tilt. If we consider a Laplace expansion of the tidal potential, we will obtain three trigonometric functions for each tidal family. The vertical direction is the direction of the vector composed by the perturbing forces and the gravitational force. Thus the deviation from the vertical on the Earth's surface is given by the following components:

$$n_1 \cong \tan n_1 = -\frac{1}{ag}\frac{\partial W}{\partial\vartheta}$$

(2.3.17)

$$n_2 \cong \tan n_2 = -\frac{1}{ga\sin\vartheta}\frac{\partial W}{\partial\lambda}$$

2.3.3 – Earth Tides

An equipotential surface is defined as a surface on which the work done to move from one point to another one is zero, since they are both at the same potential. About the Earth, in each point P on its surface, the vector resulting from the composition of the centrifugal force, the gravitational force and the lunisolar force associated to the potential W is normal to an equipotential surface.

Let's be $V = h_1$ the equation for an equipotential surface: h_1, then, can be defined as the distance from a reference surface (which could be, for example, the geoid) for which $V_0 = 0$. The function V is known as *terrestrial potential*.

Gravitational acceleration is:

$$g = -\frac{\partial V}{\partial r}.$$

(2.3.18)

By applying a tidal force, the equipotential surface will be deformed: the point $P(r)$ then becomes $P(r+\xi)$. The Taylor expansion for the terrestrial potential modifies it in:

$$V(r+\xi) = V(r) + \xi\frac{\partial V}{\partial r}.$$

(2.3.19)

The equation for the equipotential surface h_1, then becomes:

$$V(r) + \xi \frac{\partial V}{\partial r} + W = h_1. \tag{2.3.20}$$

This equation is valid for an equipotential surface, thus the varying components must be null:

$$\xi \frac{\partial V}{\partial r} = -W \tag{2.3.21}$$

which, using the equation (2.3.18), becomes:

$$\xi = \frac{W}{g}. \tag{2.3.22}$$

This last equation represents the motion of Earth's surface when the potential W is acting, and is known as *Earth Tide*.

2.3.4 – Estimation of tidal effects

Starting from the general expression for the tidal potential:

$$W = GM \sum_{n=2}^{+\infty} \frac{r^n}{d^{n+1}} P_n(\cos z) \tag{2.3.23}$$

and introducing the average Moon distance from Earth c and the radius of a sphere with the same volume of the Earth:

$$\bar{a} = \sqrt[3]{a^2 b} \tag{2.3.24}$$

it can be defined the Doodson's constant:

$$D = \frac{3}{4} GM \frac{\bar{a}^2}{c^3}. \tag{2.3.25}$$

This constant has the same physical dimensions of a work and represents a mean value for the tidal potential with specific approximations.

Introducing the current definition of the universal gravitational constant G, the equation (2.3.25) can be rewritten as:

$$D = \frac{3}{4} \left(\frac{\bar{g} \bar{a}^2}{E} \right) M_L \frac{\bar{a}^2}{c^3} \tag{2.3.26}$$

where $\bar{g}$ is the mean gravitational value calculated on the surface of a sphere having the same mass and volume of the Earth, E is the Earth's mass, M_L is the Moon's mass. The best value for D is 2.627723 m^2 / sec^2. Using the Doodson's constant, the deformation of Earth's surface due to tides is, then, equal to:

$$\xi = \frac{D}{g} = 0.2676 \text{ m} \tag{2.3.27}$$

while the variation of gravitational acceleration on Earth's surface is:

$$\Delta g = -\left(\frac{\partial W_2}{\partial r}\right)_{r=a} = -\frac{2}{a}W_2(a) = \frac{2D}{a} = 0,08249 \text{ mgal.} \tag{2.3.28}$$

and the periodical deviation from the vertical is:

$$n \sim \tan n = -\frac{1}{ag}\frac{\partial W}{\partial z} = C_{xy}\sin(2z) \tag{2.3.29}$$

with

$$C_{xy} = \frac{2D}{ag} = 8,399 \times 10^{-8} \text{ rad.} \tag{2.3.30}$$

2.3.5 – Decomposition of tidal potential into frequencies

The classification of tidal frequencies in the three categories (semidiurnal, diurnal and. long-periodic, as used in the previous section) is of course valid only in the first approximation. As soon as one starts considering the ratio $\left(\frac{c}{d}\right)^3$, as well as the declination δ and the hour angle H as varying in time, one discovers that the tidal potential variation is a much more complex phenomenon, requiring a more sophisticated. treatment.

The time-varying terms of the three constituents (sectorial, tesseral and zonal) can be rewritten in terms of pure cosine series, using some simple trigonometric formulae. This was first done by Farrell in 1874, but later Doodson *[1921]* also introduced symbols for the individual cosine waves that have been used ever since: he published a harmonic expansion with 386 terms. By observing 100 years of astronomical data, Doodson found six variables which increase linearly in time. These are:

- **Mean lunar day (τ):** $\tau = H + 180°$, it is counted starting from the lower lunar transit
- **Mean tropic lunar longitude (s):** tropic month
- **Mean tropic solar longitude (h):** tropic year
- **Mean tropic lunar perigee longitude (p)**
- **Mean tropic lunar ascending node longitude (N'):** $N' = -N$, this variable has the opposite sign since N is the only variable decreasing in time
- **Mean tropic perihelion longitude (ps)**

The periods of variation of the six variables are given in Table 2-2 with the corresponding hourly speeds. The same table also gives the various lunar periods as functions of these variables.

Table 2-2 – Periods of variation of six variables with corresponding hourly speeds. Please note that the hourly speed σ is obtained observing that the Moon's revolution takes 27,3 days. There is thus every day a lag of 24 h / 27,3 = 50,47 min.

	Hourly speed		
$t_\odot = t - h$	Mean solar day	15° 000000	**1.000000 m.s.d.**
$t = t_\odot + h$	Sidereal day	15° 0410686	**0.997270 m.s.d.**
$\tau = t - s$	Mean lunar day	14° 4920521	**1.035050 m.s.d. (24h 50.47 min)**
s	Tropic month	0° 5490165	**27.321582 day**
h	Tropic year	0° 0410686	**365.242199 day**
p		0° 0046418	**8.847 year** Period of revolution of the mean perigee of the Moon
N'		0° 0022064	**18.613 year** Period of revolution of lunar nodes
p_s		0° 0000020	**20.940 year** Period of revolution of the solar perihelion

These variables allow to consider the various perturbative phenomena due to the variation of Earth and Moon orbits caused by the presence of the Sun.

2.3.6 – Tidal spectrum

The components of the tidal spectrum are obtained starting from the Laplace expansion of the tidal potential (2.3.11), using the six astronomical variables reported into paragraph 2.3.5: in this way, the spectrum can be written as sum of frequencies related with the motion due to interaction among Earth, Moon and Sun.

Sectorial Functions – Semidiurnal Waves

The general expression for the sectorial function is:

$$D \left(\frac{c}{d}\right)^3 \cos^2 \varphi \cos^2 \delta \cos 2H. \tag{2.3.31}$$

Taking in account the lunar effect, we obtain the principal wave with argument:

$$M_2 : 2\left(\frac{\partial \tau}{\partial t}\right) \tag{2.3.32}$$

where we calculate the derivative of the mean lunar day in respect to time. The M_2 tidal constituent has a period equal to 12h 25m 14s. Apart from this constituent, there are a group of couple of waves obtained from the combination of $\cos 2 \left(\frac{\partial \tau}{\partial t}\right) t$ with the other arguments. For example:

$$L_2 : \left[2\left(\frac{\partial \tau}{\partial t}\right) + \left(\frac{\partial s}{\partial t} - \frac{\partial p}{\partial t}\right)\right] \tag{2.3.33}$$

$$N_2 : \left[2\left(\frac{\partial \tau}{\partial t}\right) - \left(\frac{\partial s}{\partial t} - \frac{\partial p}{\partial t}\right)\right] \tag{2.3.34}$$

These are caused by the ellipticity of the lunar orbit. Another couple of constituent is represented by:

$$K_2 : \left[2\left(\frac{\partial \tau}{\partial t}\right) \pm 2\left(\frac{\partial s}{\partial t}\right)\right] \tag{2.3.35}$$

The K_2 constituents have a period of 11h 58m 2s, and are related with the declination.

By performing a complete expansion of both the terms $\left(\frac{c}{d}\right)^3$ and $\cos^2 \delta$, we obtain an infinite number of components, each with frequency distributed symmetrically along $2\frac{\partial \tau}{\partial t}$, that is the frequency for half a mean lunar day.

Taking in account even the solar effects, moreover, we obtain the following constituents:

$$S_2 : \left[2\left(\frac{\partial \tau}{\partial t}\right) + \left(2\frac{\partial s}{\partial t} - 2\frac{\partial h}{\partial t}\right)\right] \tag{2.3.36}$$

the two elliptical waves:

$$R_2 : \left[2\left(\frac{\partial \tau}{\partial t}\right) + \left(2\frac{\partial s}{\partial t} - 2\frac{\partial h}{\partial t}\right)\right] - \left(\frac{\partial h}{\partial t} - \frac{\partial p_s}{\partial t}\right) \tag{2.3.37}$$

$$T_2 : \left[2\left(\frac{\partial \tau}{\partial t}\right) + \left(2\frac{\partial s}{\partial t} - 2\frac{\partial h}{\partial t}\right)\right] + \left(\frac{\partial h}{\partial t} - \frac{\partial p_s}{\partial t}\right) \tag{2.3.38}$$

and the two declinational waves:

$$K_2 : \left[2\left(\frac{\partial \tau}{\partial t}\right) + \left(2\frac{\partial s}{\partial t} - 2\frac{\partial h}{\partial t}\right)\right] \pm \frac{\partial h}{\partial t} \tag{2.3.39}$$

with S_2 constituent with period 12h 0m 0s, R_2 constituent with period 12h 0m 59s, T_2 constituent with period 11h 59m 0s and K_2 constituent with period 11h 58m 2s. Since the pulsation with a period equal to half sidereal day is produced simultaneously by the Moon and the Sun, the contributes cannot be separated and we have a constituent with the same symbol K_2.

Each constituent of Sectorial waves has a period of about 12h: this is the reason why these components are known as Semidiurnal Waves.

Tesseral Functions – Diurnal Waves

The general expression for the tesseral function is:

43

$$D\left(\frac{c}{d}\right)^3 \sin 2\varphi \sin 2\delta \cos H. \tag{2.3.40}$$

In this case the main constituent (for the sectorial waves it is the M_2 term) does not exist, since the mean value for $\sin 2\delta$ is null. The most important terms, hence, derive from the declinational waves with argument:

$$K_{1m} : \left(\frac{\partial \tau}{\partial t}\right) + \left(\frac{\partial s}{\partial t}\right) \tag{2.3.41}$$

$$O_1 : \left(\frac{\partial \tau}{\partial t}\right) - \left(\frac{\partial s}{\partial t}\right) \tag{2.3.42}$$

with K_{1m} constituent with period equals to 23h 56m 4s and O_1 constituent with period 25h 49m 10s.

Similarly, there exist two declinational waves generated by the Sun:

$$K_{1s} : \left(\frac{\partial \tau}{\partial t}\right) + \left(\frac{\partial h}{\partial t}\right) \tag{2.3.43}$$

$$P_1 : \left(\frac{\partial \tau}{\partial t}\right) - \left(\frac{\partial h}{\partial t}\right) \tag{2.3.44}$$

where K_{1s} is the constituent with period 23h 56m 4s and P_1 has period 23h 3m 57s.

Again, as for the case of K_2 constituents generated separately by the Moon and the Sun for the semidiurnal waves, even for the K_1 constituent there are two contributes, due to the Moon and to the Sun. This frequency is due to the sidereal rotation of the Earth, and the Moon contributes for two thirds of the total wave amplitude while the Sun for the remaining third part.

The group of diurnal waves contains even elliptical waves due to Moon or Sun motion:

$$Q_1 : \left[\left(\frac{\partial \tau}{\partial t}\right) - \left(\frac{\partial s}{\partial t}\right)\right] - \left[\left(\frac{\partial s}{\partial t}\right) + \left(\frac{\partial p}{\partial t}\right)\right] \tag{2.3.45}$$

$$J_1 : \left[\left(\frac{\partial \tau}{\partial t}\right) + \left(\frac{\partial s}{\partial t}\right)\right] + \left[\left(\frac{\partial s}{\partial t}\right) + \left(\frac{\partial p}{\partial t}\right)\right] \tag{2.3.46}$$

$$\Pi_1 : \left[\left(\frac{\partial \tau}{\partial t}\right) - \left(\frac{\partial h}{\partial t}\right)\right] - \left[\left(\frac{\partial h}{\partial t}\right) - \left(\frac{\partial p_s}{\partial t}\right)\right] \tag{2.3.47}$$

$$\Psi_1 : \left[\left(\frac{\partial \tau}{\partial t}\right) + \left(\frac{\partial h}{\partial t}\right)\right] + \left[\left(\frac{\partial h}{\partial t}\right) - \left(\frac{\partial p_s}{\partial t}\right)\right] \tag{2.3.48}$$

where the elliptical constituents due to Moon's motion are Q_1, which has period 26h 52m 6s, and J_1, which has period 23h 5m 54s (these two constituents are related, respectively, to O_1 and K_1); while the elliptical constituents due to Sun's motion are Π_1 and Ψ_1 with periods, respectively, 24h 7m 56s and 23h 52m 9s.

Zonal Functions – Long-period waves

The principal wave has a period of 13.66 days, is denoted as M_f (Moon fortnightly) and its argument is *2s*. The most important elliptical wave is the M_m (Moon monthly), with argument $\left(\frac{\partial s}{\partial t}\right) - \left(\frac{\partial p}{\partial t}\right)$. The main waves due to the Sun's motion are the *Ssa* (Sun semi annual), with argument $2\left(\frac{\partial h}{\partial t}\right)$ and the *Sa* (Sun annual), with argument $\left(\frac{\partial h}{\partial t}\right) - \left(\frac{\partial p_s}{\partial t}\right)$.

2.3.7 – Love's numbers

The mechanical response of the Earth to tidal forces is global. Because of the long time scales of the tides, the Earth has the time to equilibrate mechanically to Earth tides. Love computed exactly the response to the Earth tides *[Melchior, 1983]* in the case of an homogeneous elastic Earth. He ignored any secondary effect like the Earth ellipticity, the Earth rotation and the ocean load. The displacement at the surface of the Earth is parameterized by two sets of parameters:

$$u_r = \sum_{n=2}^{+\infty} \frac{h_n}{g} W_n \qquad (2.3.49)$$

$$u_\vartheta = \sum_{n=2}^{+\infty} \frac{l_n}{g} \frac{\partial W_n}{\partial \vartheta} \qquad (2.3.50)$$

$$u_\varphi = \sum_{n=2}^{+\infty} \frac{l_n}{g} \frac{1}{\sin\vartheta} \frac{\partial W_n}{\partial \varphi} \qquad (2.3.51)$$

where h_n are the Love numbers, l_n are called the Shida numbers. These numbers are dependent of the deep Earth structure, assuming a spherical symmetry for the Earth's internal properties ($\rho=\rho(r)$, $\lambda=\lambda(r)$, $\mu=\mu(r)$) Numerical simulations enable to compute the Love and Shida numbers for more realistic structures of the Earth.

By the use of these numbers, it is possible to represent the Earth's deformations due to the tidal potential, which can be expressed as an expansion in spherical polynomials. Moreover, the parameters h_n and l_n define Earth's crust deformation: h_n is the normal deformation, l_n the planar deformation (tilt).

Starting from the definition given above about the parameterization of crustal displacement caused by the tidal potential, it is possible to compute the strain tensor:

$$\varepsilon_r = \varepsilon_{11} = \frac{\partial u_r}{\partial r} = \sum_{n=2}^{+\infty} \frac{h_n}{ga} \frac{\partial W_n}{\partial r} \tag{2.3.52}$$

$$\varepsilon_\vartheta = \varepsilon_{22} = \frac{u_r}{r} + \frac{1}{r}\frac{\partial u_\vartheta}{\partial \vartheta} = \sum_{n=2}^{+\infty} \frac{1}{ga}\left(h_n W_n + l_n \frac{\partial^2 W_n}{\partial \vartheta^2}\right) \tag{2.3.53}$$

$$\varepsilon_\varphi = \varepsilon_{33} = \frac{u_r}{r} + \frac{u_\vartheta \cot \vartheta}{r} + \frac{1}{r}\frac{\partial u_\vartheta}{\partial \vartheta} = \sum_{n=2}^{+\infty} \frac{1}{ga}\left(h_n W_n + l_n \cot \vartheta \frac{\partial W_n}{\partial \vartheta} + \frac{l_n}{\sin \vartheta}\frac{\partial^2 W_n}{\partial \varphi^2}\right) \tag{2.3.54}$$

where values were computed on Earth's surface, with $r = a$.

Chapter 3 – Strainmeters and Tiltmeters

As seen in previous chapters, the strain field is subject to changes due to different kind of forces and sources. One of the main responsible of changes in stress field is obviously the lunisolar attraction treated from a theoretical point of view in Chapter 2. Along with these quasi-periodic forces acting constantly above and below the Earth's crust, transient waves due to earthquakes, magmatic intrusions and other higher-frequencies phenomena must be taken in account in order to completely describe the changes in strain.

Of course, while the tidal response can be expected by the theoretical models and using the experimental observations to refine them, the changes due to transient waves cannot be forecast and must be observed. Geophysical devices can be used to achieve this goal.

Two kind of instruments can be used: strainmeters and tiltmeters. As we have already seen in previous sections, both kind of instruments basically evaluate the same physical quantities, both related with the strain field measured in the place where the devices were installed.

Stress redistribution in situ can be monitored by using borehole strainmeters (a quick description of these instruments was provided in Chapter 1), which have to be considered as local inhomogeneities in Earth's crust, and which, at a first approximation, don't deform the local stress field.

For the current dissertation, instruments were installed in Campi Flegrei caldera and near Mt. Vesuvius volcano: in the following of the current chapter we will give a brief explanation of the geological setting for the selected areas.

3.1– Campi Flegrei and Mt. Vesuvius geological description

Mount Vesuvius and Campi Flegrei lie along the northern shores of the Bay of Naples and bracket the city of Naples to the west and southeast, respectively. Their volcanic activity is related to their location at the intersection of a set of deep and major fractures through which magma can rise.

Mount Vesuvius lies approximately 15 km from the city of Naples and rises 1281 m above sea level within the ramparts of the Mount Somma caldera.

The Campi Flegrei volcanic complex comprises a caldera that formed about 35.000 years ago and is today about 13 km in diameter and includes numerous cones and nested craters, the largest of which has a diameter approaching 15 km and is partly submerged by the sea. The caldera lies about 25 km west of Vesuvius and 5 km west of Naples.

Despite their current dormant stage, Mt. Vesuvius and Campi Flegrei are considered among the most dangerous volcanoes in the world, because of their proximity to the densely inhabited Campanian Plain and city of Naples, where 1.5 million people would be in immediate danger if an eruption occurred.

3.1.1 – Campi Flegrei

The Campi Flegrei caldera (Southern Italy) is a volcano-tectonic depression, framed on the east by Vesuvius and on the west by the volcanic islands of Ischia and Procida. It is a highly populated area (about 400.000 people living inside the caldera itself) located 15 km west of Naples inside the Campanian Plain, a graben-like structure at the eastern margin of the Tyrrhenian Sea. The Campi Flegrei caldera is a nested and resurgent structure created by a subsidence of the Campi Flegrei area due to several collapses during the last 40k years, mainly related to two major collapses that occurred 37k-39k years (the Campanian Ignimbrite, CI) and about 12k years (Neapolitan Yellow Tuff, NYT) ago *[Civetta et al., 1991]*. The oldest rocks of the area, about 60k years, are located along sea cliffs and scarps related to the CI caldera collapse.

The structure of the caldera has been recently investigated by using several geological and geophysical methods *[Zollo et al., 2003]*.

The magmatic system of the Campi Flegrei caldera is thought to include a shallow, large-volume trachytic reservoir, site of differentiation processes, periodically refilled by new magma batches rising from a deep reservoir. The CI eruption extruded about 200 km^3 of trachytic to phonlitic-trachityc magma, and affected the Campi Flegrei and the bays of Pozzuoli and Naples. The NYT phreatoplinian eruption extruded about 50 km^3 of alkali-trachyte to latite magma. The related caldera was centered on the Campi Flegrei and nested within the CI caldera. Successive volcanic activity occurred only within the caldera structure, where numerous explosive eruptive vents are located, and frequently along the rim of the Quaternary explosive caldera. It has been characterized by three "Epochs of Activity", occurrence of explosive eruptions with a return period of thousands of years, creating intracalderic collapses and significant uplifts.

Three isotopically and geochemically distinct magmatic components (similar to the CI trachytic magma or to the NYT latitic-alkalitrachytic magma, and a trachybasalt never erupted before) were erupted as either homogeneous or mixed magma batches. The last eruption occurred in 1538 at western periphery of Campi Flegrei and created a spatter cone (Monte Nuovo, about 130m).

Since the last eruption, like many calderas, the Campi Flegrei caldera suffers notable unrest episodes, including ground deformations unsurpassed anywhere in the World *[Newhall and Dzurisin, 1998]*, seismic

swarms and increases in the degassing activity *[Barberi et al., 1984]*. Its bradyseismic activity, a slow ground movement later recognized in several other volcanic areas, during the last 2000 years is spectacularly enlightened by the peculiar geographic setting and the presence of Roman ruins. In fact, Campi Flegrei caldera is partially submerged, so sea level provides a natural reference level for relative ground movements, and marine deposits on Roman ruins and historical documents have been studied to envisage large, secular subsidence, superimposed by very fast uplifts, not always giving rise to an eruption *[Dvorak and Mastrolorenzo, 1991]*.

The most studied Roman ruin, since its excavation in 1750, is the marketplace (Macellum) in Pozzuoli, the so-called Serapis Temple, whose sinking accurately recorded caldera subsidence since around 1800.

The secular elevation of Serapis Temple is depicted into Figure 3.1.

Figure 3.1 – Secular changes in elevation measured using Serapis Temple in Pozzuoli, according to historical document and sea-level shown near the columns of the temple [Troise et al., 2007]
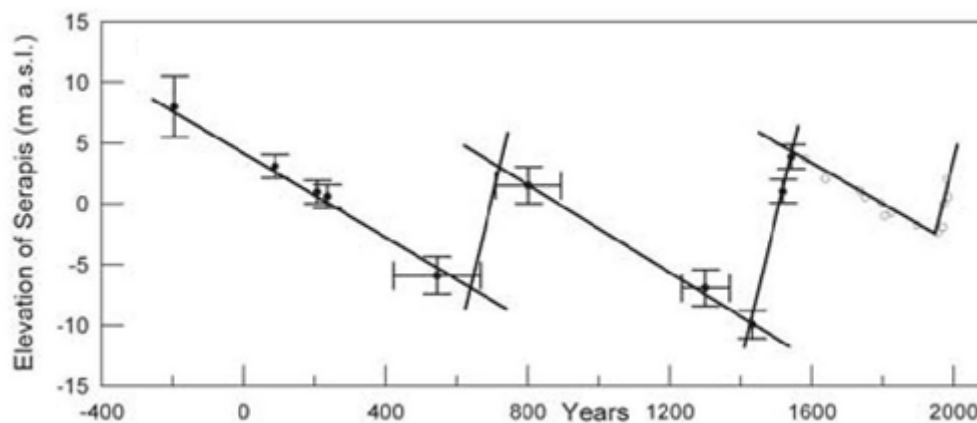
The caldera has been continuously subsiding (at about 1cm per year), from 1538 till 1970. A relevant ground uplift, more than 1m of deformation, occurred in the period 1970-1972 and, after a small subsidence of about 30cm after 1972, a very strong uplift occurred in the period 1982-1984 with a nearly symmetrical uplift rates of 3mm/day bringing a total vertical displacement of about 1.8m, with a maximum of about 2.5m at the town of Pozzuoli (the center of uplift).

The vertical displacement measured in the center of the uplift during the period 1968-2006 is depicted in Figure 3.2, while the last two years of data, magnified, are depicted into Figure 3.3.

49

Figure 3.2 – Unrest episode of Campi Flegrei caldera: measures refer to the uplift of downtown Pozzuoli starting from 1968 to 2006. Two main episodes have been recorded, followed by slow subsidence with superimposed smaller mini-uplifts (occurred in 1989, 1995 and 2000-2001) [Troise et al., 2007]
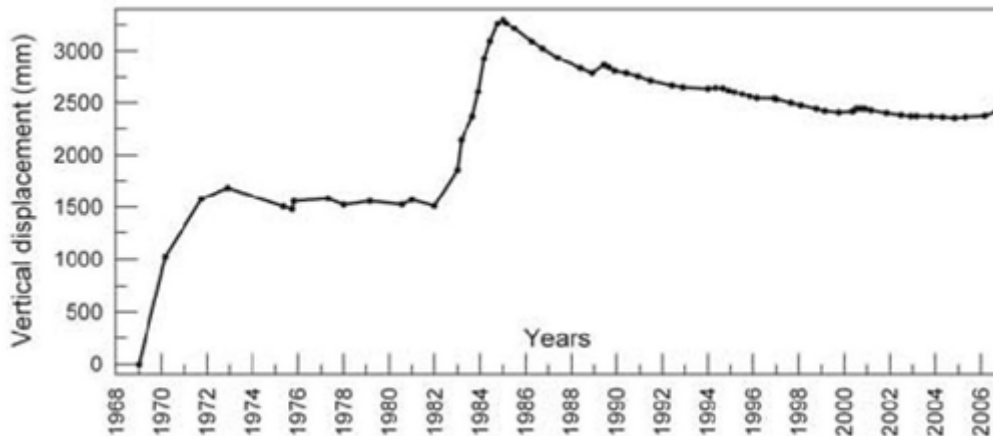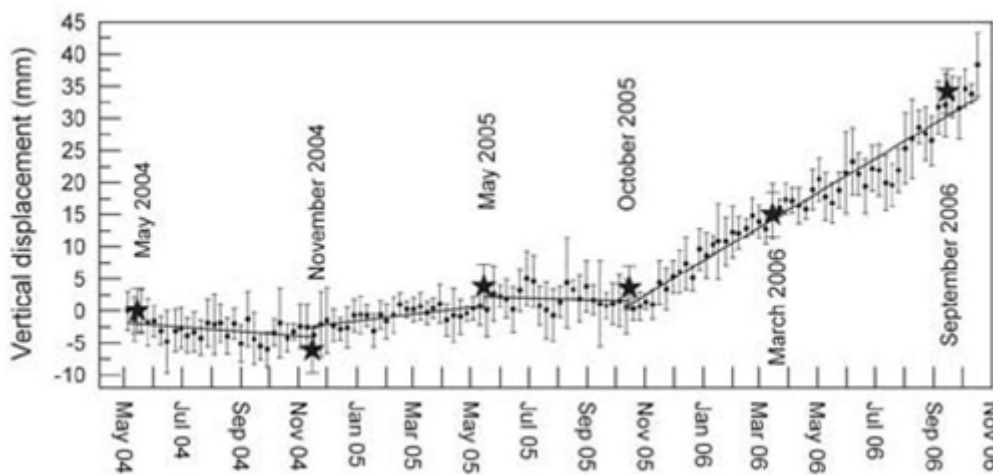

Figure 3.3 – Magnification of the last two years of data reported in previous image: stars represent rate changes in measured vertical displacement, while the vertical labels show month and year of rate change [Troise et al., 2007]

Microseismicity (more than 15.000 shallow earthquakes, maximum magnitude of 4.0, located mostly on land near the Solfatara crater) occurred during the 1982-1984 uplift was mostly confined within depths of 3-4 km *[Aster and Meyer, 1988]*, in the few km thick layer of volcanic deposits filling the caldera and forming an inner basin geometrically consistent with the gravity low anomaly *[De Lorenzo et al., 2001]*.

Starting from the beginning of 1985, seismic activity strongly diminished down to a generally aseismic behavior, and the still continuing subsidence began. It is superimposed by some short uplift phases (miniuplifts during 1989, 1994, 2000, 2004 and 2005), strain rate increase being accompanied by small swarms of microearthquakes [Saccorotti et al., 2001], although ground level remains more than 1m above pre-1970 levels.

The Campi Flegrei caldera has been extensively studied to understand the mechanisms causative of recurrent uplift and subsidence. Pressure generation due to a magma chamber of hydrothermal fluids

[Bianchi et al., 1987; Gaeta et al., 1998] has been suggested. However, possible depths of ground deformation sources, as obtained from the inversion of observed, very concentrated ground deformation pattern, were between 1.5 to 4 km, but he location of a magmatic reservoir at about 4-5 km depth was inferred mainly from the extrapolation at depth of temperature data *[Agip, 1987]* and teleseismic observations *[De Lorenzo et al., 2001; Ferrucci et al., 1992]*. In addition, De Natale et al. *[1997]* showed that the shape of ground deformation during unrests could be due to an overpressurized source with a top also 4 km depth, if ring faults almost free to slip were taken into account. Since seismicity occurs only during uplift episodes at Campi Flegrei, Troise et al. *[2003]* explained earthquake occurrence and location in terms of Coulomb stress changes due to inflation of the shallow magma chamber.

Aster and Meyer [1998] suggested the existence of a region of highly water saturated fractured rocks at 1 km depth, the depth of the main aquifer has been estimated at 1-3 km from seismic tomography and geothermal exploration wells *[De Natale et al., 2001]*, tomographic images by Zollo et al. *[2003]* evidenced no large shallow magmatic bodies, geochemical data *[Tedesco et al., 1990]* did not support the magmatic origin of the 1982-1984 unrest, and correlation between gas emission rate and ground deformation ascribed to fluid intrusion has been envisaged *[Chiodini et al., 2003]*. More recently, seismic tomographic analysis by Vanorio et al. *[2005]* suggested the presence of fractured overpressured gas-bearing formations and excluded the presence of melted rocks at 4 km depth, and confirmed the presence of rocks containing fluids in the liquid phase at 1 km depth.

Even if the role of hydrothermal fluids has been more and more defined (including interactions of the magmatic system with the shallow hydrothermal system) a hybrid of magmatic and hydrothermal single source, fluid migration to and from the caldera hydrothermal system as the only source, and multiple – one deeper magmatic and one shallower hydrothermal – sources *[De Natale et al., 2001; Battaglia et al., 2006; Gottsmann et al., 2006]*, the question about magmatic and / or hydrothermal causative source of the Campi Flegrei ground deformations and microgravimetric changes, and the assessment of its characteristics, is still open.

As explicitly expressed by Gottsmann et al. *[2006]*, deduced unrest source parameters are heavily biased on the considered time interval and continuous ground deformation measurements and gravity monitoring "must provide critical baseline data on the background behavior at the caldera against which 'anomalous' future behavior may be compared for hazard assessment and risk mitigation".

All of the strain changes in Campi Flegrei area are obviously followed by tilt changes too. The region of vertical instability affects a coastline near the port of Pozzuoli extending some tens of km to east and west. In this context, the position where the two tiltmeters were installed was chosen so that it would be possible to monitor tilt changes due to magmatic intrusion in both radial and transversal direction in respect with the (supposed) center of the magmatic chamber. In respect with the center of the uplift episodes, the position of the two tiltmeters is reported into Figure 3.4.

Figure 3.4 – Google Earth location map showing volcanic features, approximate 1982-88 uplift contours [Dvorak and Mastrolorenzo, 1991], tiltmeters and tide-gauges near Pozzuoli.
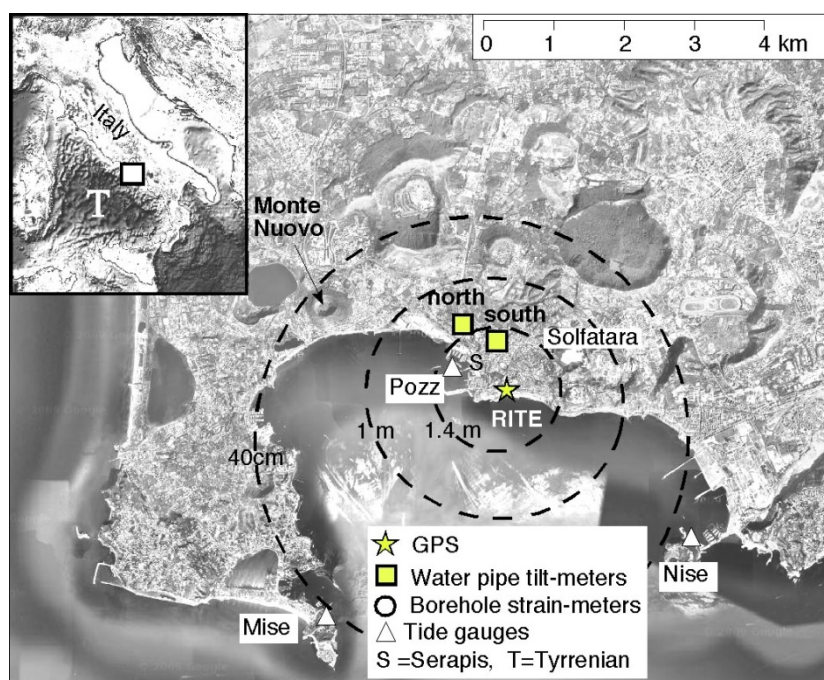
3.1.2– Mt. Vesuvius

Since the last 1944 eruption Mt. Vesuvius is in a quiescent stage. An increase of scientific interest for this volcano dates back in 1981 *[Sheridan et al., 1981]* when the detailed analysis of pumice flows and other pyroclastic products showed clearly the sequences, in the last 19.000 years, of 5 plinian eruptions and a larger number of subplinian events, lastly occurred in 472 and 1631 a.D. Following this eruption the activity has been almost continuous, and divided in 18 Strombolian cycles characterized by effusive and moderately explosive eruptions, the last occurred in 1944. Since 1944 this volcano is in a quiescent stage, with only fumarolic and low level of seismic activity, with the absence of ground deformation episodes. In the last decade a small increase of the magnitude of the largest earthquakes, some felt by population, has been reported *[Bianco et al., 1999; Zollo et al., 2002; Del Pezzo et al., 2003]*. Volcanological models of Plinian eruptions have been modeled through continuous magma filling from a reservoir located in the shallow crust at 3-6 km depth *[Rosi et al., 1987; Civetta and Santacroce, 1993]*. Mount Vesuvius has been the object, in the last decade, of extensive geophysical and volcanological studies *[Gasparini et al., 1998]*. In particular, geophysical tomography has been performed with the objective of improving the knowledge of the deep structure and extent of magma reservoir below Mt. Vesuvius; this knowledge is essential to provide more realistic simulation models of the eruptive activity and is the base for a precise identification of possible precursors of future eruptions. Dense seismic arrays recorded land shots and marine airgun signals generated during experiments carried out in 1994, 1996 and 1997 with the main purpose of defining the geological structures beneath Mt. Vesuvius *[Zollo et al., 1996; Auger et al., 2001]*. The results obtained revealed the presence of a large low P-wave velocity body, resembling to a huge sill, below the volcanic edifice, located at an average depth around 8 km, extending towards East and in the direction of the other volcanic center of Campi Flegrei, covering a surface larger than 300 squared km. The results by Scarpa et al. *[2002]* show a quite heterogeneous geological structure in the upper 5 km below the topographical

surface of Mt. Vesuvius, having an alternation of high and low velocity layers for P-waves, which is linked to remnant of past intrusion bodies.

Ground deformation monitoring of Vesuvius is presently based on a GPS network, extending EDM measurements carried out since 1970. This system can detect slow strain changes but with sensitivity of 10^{-6} and hence with a threshold for adequately monitoring ground deformations which has been questioned as too high by Russo et al. on the basis of feeding rate of magma and modeling the mechanical stability of the volcano.

Routine monitoring of seismic activity on Mt. Vesuvius, like most volcanoes in the World, is carried out by networks of short-period seismometers. The collected data are utilized to determine location and energy of earthquakes, and their time evolution. This approach, especially at some Japanese volcanoes, allowed to establish for each volcano some empirical relations between these seismic parameters and the eruptive activity.

3.2 – Strainmeters

Strainmeters have been in use for several decades for the measurement of strain in the earth's crust. Yet the dominant signal recorded by these instruments during the first months, a relatively large magnitude, long-term accumulation of compressional or extensional strain that is removed prior to interpretation of the residual signal, has never been fully understood, but these long-term trends could be modeled in terms of the poroelastic response of the wellbore to drilling. Using data from several strainmeters in different locations, it can be seen how the trend successfully describes strain accumulation for several months to over a year after installation.

Agnew *[1986]* provides an excellent introduction to the measurement of wellbore strain and the development of volumetric strainmeter instruments. The subsequent development of borehole tensor strainmeters allowed for the measurement of radial strain in specific directions, which enables calculation of both areal and shear strain *[Gladwin, 1984]*. Installation of these instruments involves lowering them into a borehole that was cored or rotary drilled slightly larger than the strainmeter diameter, with centralizers on the tool string to keep the instrument centered. The strainmeter is then coupled to the rock by injection of a layer of expansive grout between the instrument and borehole wall (see Figure 3.4). The sites developed and described in the current work include pressure transducer, temperature sensor, and some are equipped with borehole seismometer located above the grouted strainmeter or broadband surface accelerometers.

Figure 3.5 – Schematic representation of a typical borehole strainmeter installation. Elements are not in scale. (A) represents the atmosphere, while (B) represents the rocks inside the Earth's crust. The installation is done inserting a casing (C) inside the borehole (D) to which the casing is tightened. The lower part of the well is drilled with a lower diameter where the strainmeter (F) is placed. A layer of expansive grout (E) fills the hole.
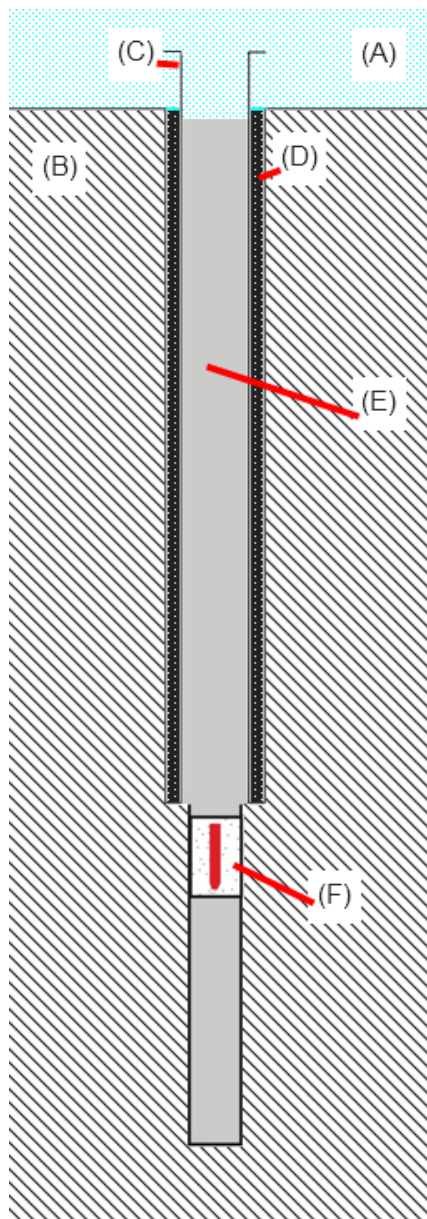
Raw borehole strainmeter data are a combination of numerous signals including but not limited to atmospheric pressure, earth tides, ocean loading, grout curing and thermal equilibration, background noise, and, finally, responses to tectonic events *[Agnew, 1986]*. Atmospheric and tidal signals are on the order of hundredths of a microstrain and can be accurately removed from the strainmeter data using measured or modeled values. They are also used to calibrate strainmeter data and evaluate data quality. The effects of grout curing and temperature perturbations, while not exactly known, are relatively short-term and only occur soon after installation of the instrument, and therefore they are often ignored or removed using a best-fit mathematical function. Noise can be characterized using spectral methods and removed through filtering.

Most tectonic strain signals are relatively small in magnitude. Coseismic offsets, for example, are generally on the order of one microstrain or less *[Johnston et al., 1994]*, and aseismic creep events are on the order of 50 to 100 nanostrain *[Gladwin et al., 1994]*. Long-term tectonic strain accumulation occurs in tectonically active areas like Parkfield, California near the San Andreas fault *[Gwyther et al., 1996]*, and Piñon Flat, California, near the San Jacinto fault *[Gladwin et al., 1987]* and has magnitudes generally less than 1 microstrain per year. Non-tectonic events such as groundwater-induced strain from rainfall events, seasonal recharge, or pumping in nearby water wells may also be observed *[Gwyther et al., 1996; Wyatt and Agnew, 1998]* and have magnitudes generally less than 1 microstrain.

Masking all of these relatively small signals is a much larger long-term trend that amounts to tens of microstrain and persists for months to years after installation. Qualitatively the trends are attributed to "borehole relaxation" or "post-relief recovery" assuming viscoelastic behavior of the surrounding rock *[Gladwin et al., 1987]*, but no quantitative, physical model for them has been offered. Uncertainty in their origin and meaning have led to the conclusion that long-term tectonic strain rates cannot be measured, because they are masked by the trends *[Roeloffs, 2006]*. That is not to say that there is nothing physically meaningful in the long-term trends, just that without a physical model it is impossible to extract anything meaningful from them.

The most common approach for removing the trends involves determining a best-fit curve, a combination of linear and exponential terms, to strain measured as a function of time *[Gwyther et al., 1996]*. Historically, this approach has worked well, particularly for volumetric strainmeters. In this case the form chosen for the trend is:

$$\text{mathematical trend} = F + A_1 e^{T_1 t} + Mt + A_2 e^{T_2 t} \qquad (3.2.1)$$

where t is time and the constants F, A_1, T_1, M, A_2, and T_2 are unique for each gauge. The fit can be carried out using daily data values and a nonlinear regression routine (for example, Marquardt's method).

It is also important to note that a strainmeter is essentially an inclusion, and one that is usually softer elastically than the surrounding rock. As a result, strain measured by a borehole strainmeter is a magnified version of the rock strain. Gladwin and Hart *[1985]* attempted to quantify this effect by deriving elastic solutions for the strainmeter response to a uniaxial far-field stress. They examined three cases: an empty hole (or one in which the strainmeter and grout are elastically the same as the rock), a "one-ring model" where the instrument has distinct elastic properties but the layer of grout between the instrument and the rock is very thin or has elastic properties similar to the rock, and a "two-ring model" where the grout has distinct elastic properties from both the instrument and the rock. For each model, far-field strain is related to instrument strain by derivation of instrument response factors (essentially scaling constants) for both the shear and areal strain components. The response factor magnitudes range roughly from one to four, meaning measured strain is one to four times the strain in the surrounding rock *[Gladwin et al., 1987]*. Since they are based on elasticity, these models do not incorporate any time-dependent effects. Spathis *[1988]* examined the case where the instrument response factors may in fact have some dependence on time.

The ring model approach is the recommended basis for analytical strainmeter data calibration, but it is generally not used in practice because of the difficulty in constraining the elastic parameters (which can number up to nine). Instead, an empirical approach using modeled solid earth tides and ocean loading is employed *[Hart et al., 1996]*. The calibration process involves empirically determining values for the areal and shear response factors such that earth tides measured by the instrument match theoretical, model-derived tides. The data that remain after removal of the trends are calibrated against modeled tides and then used to calculate the local areal and shear strain components *[Hart et al., 1996]*.

In addition to overall instrument calibration, it is sometimes necessary to weight data from particular gauges in order to bring atmospheric pressure, tidal signals, or earthquake signals measured on different gauges into agreement. Unfortunately, this remains an imprecise science, and not uncommonly gauge weights determined using one approach differ from those derived from an alternate approach. The need for individual gauge weights has been attributed to instrument errors, measurement errors, and inhomogeneities in the near wellbore environment *[Hart et al., 1996; Yoshikawa et al., 2001]*.

3.2.1 – Dilatometers

Seismographs are the principal tool used by seismologists in their study of earthquakes and related phenomena. Invented approximately 150 years ago, motion seismographs are today in a highly developed state. Their function is to record faithfully motion associated with propagating stress waves caused by disturbances in the Earth. Seismological measurements are generally made with instruments responsive to displacement, strain, or tilt and to their time derivatives. These instruments are called seismometers, strainmeters and tiltmeters, respectively. The combination of a seismometer or strainmeter with a recorder is generally called a seismograph.

There is a popular belief (or hope) among seismologists that, if earthquakes or their causes are sufficiently understood, prediction or forecasting may be possible. It has suggested that, with sufficiently sensitive and stable strainmeters, changes in the strain field prior to an earthquake might be detected and diagnosed. Because strain decays approximately as distance cubed, great sensitivity is required. Strain and strain rate recording, particularly in the quiet environment of a drilled hole a few hundred meters deep, appear to offer hope of adding to such knowledge through increasing the signal-to-noise ratio.

In older instruments, linear strain was derived by measuring the relative motion between two points in the Earth, or on its surface, and dividing the motion by the nominal separation distance between the points. The linear strain seismograph is largely the result of the work done by Benioff. Early attempts to measure relative motion between two points on the surface of the Earth were made by Milne in Japan and Oddone in Italy, but Benioff's instrument had a higher sensitivity to strain changes.

Benioff's linear strain seismograph was made possible by development of a very sensitive electromagnetic transducer used in conjunction with a galvanometer. This precedent setting transduction system was used earlier in a vertical seismometer and was then incorporated in a strain measuring system. The gage length of this instrument was 20 m and it consisted in one iron pipe (about 5 cm in diameter) supported by twelve pillars. This was the first device to record seismic phenomena of longer period than 100 sec.

Benioff *[1935]* mentions the concept of a dilatation or volume strainmeter in the form of a spherical, liquid filled vessel very near the Earth's surface: motion of a small bellows mounted on a connecting neck or tube was to be monitored with his electromagnetic transducer. Such an instrument was capable of monitoring only areal strain (pure dilatation of surrounding rocks), hence the name of dilatometer. Pekeris *[1940]* suggested the use of dilatometers to study Earth tides: estimated seismic noise and its correlation with Earth tides is shown in Figure 3.5 as a function of frequency. The microseism motion near 10^{-1} Hz corresponds to strain of approximately 10^{-10} ε and Earth tide points near 10^{-5} Hz correspond to stain of about 10^{-8}. Low frequencies like those related with Earth tides cannot of course be evaluated by the use of displacement, velocity or acceleration transducers, which are basically built in order to provide a good and reasonable response to higher frequencies transient waves, just like those produced during a strong motion earthquake. In this case, the only instruments capable of monitoring and recording such low frequencies are borehole volume strainmeters, developed by Sacks and Evertson, and hence known as the Sacks-Evertson strainmeter *[Sacks and Evertson, 1968; Evertson, 1975]*. The principle of the strainmeter is very simple: the interior of a cylindrical pipe of stainless steel is divided into two spaces by a bulkhead, through which a small hole is bored. The sensing oil fills the lower space completely. The upper space is filled partly with oil and partly with gas, usually argon, and oil is free to move between the upper and lower spaces through the hole. The whole instrument is put in a borehole and fixed in place with expanding cement. A strain change in the surrounding rocks strains the instrument and causes sensing oil to go up and down through the hole. This causes an elastic deformation in the bellows set over the hole in the upper space. The deformation is transformed into an electrical signal, which is transmitted to the surface by a cable. An electric heater for calibration of the instrument and a valve for releasing an over-sale condition are also included in the instrument.

The frequency response of the purely mechanical part of the instrument depends mainly on the viscosity and the compressibility of the sensing oil, and in principle the instrument can follow the strain changes with periods from several seconds to infinity. Its sensitivity depends on the amount of oil which goes up and down through the hole in the bulkhead, and therefore, on the volume of the lower space. For the borehole strainmeters used in the current dissertation, the stainless steel pipe is 3mm thick, with an internal radius of 54mmm and a length of about 4m, the lower 3.75m of which is the length of the sensing volume, namely, the oil reservoir.

Figure 3.6 – Seismic noise amplitude vs. frequency diagram. Earth tides have lower frequencies but higher amplitudes in respect with average values of earthquakes. Microseisms represent the lower-bound of seismic waves amplitudes.
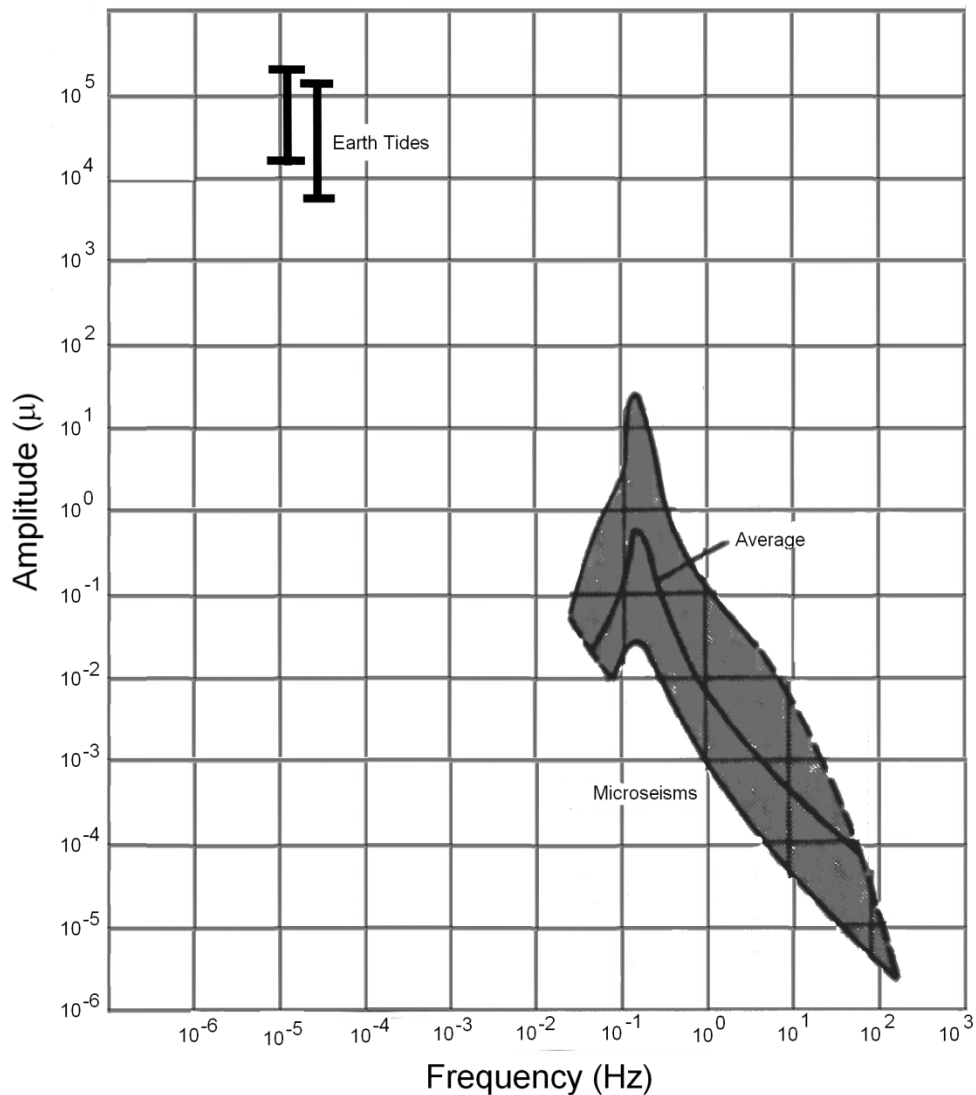
One advantage of the borehole strainmeter is that even one instrument can cover a very wide range of strain periods. Another advantage is that the instrument can be rather easily installed. One problem with the borehole strainmeter is the difficulty in calibrating it. Once the instrument is set underground, it is almost impossible to draw up again. It may be impossible to directly see the condition in which the strainmeter is set. The instrument is calibrated by using Earth tides for the lower frequencies, and local, regional or teleseismic earthquakes for the higher frequencies, as we will show in the following of the current work. Anyway, the sensitivity obtained in this way may not be used directly to derive the strain change in rocks around the instrument. We must take into account what are called cavity effects caused by a vertical borehole, just like the effects on a bar extensometer in a horizontal tunnel (a similar problem alters tilt measurements in tiltmeters, as we will show in the following of the current chapter). It is impossible to solve completely all cavity effects theoretically. Harrison [1976] calculated the effects of a cavity and irregular topography on the strain field using the finite element method, and found that the strain across a long tunnel is affected more than the one along a short tunnel. The same or worse situation exists for the borehole strainmeter, because the borehole strainmeter measures more local strains than an average

extensometer does. While observed strain data are often compared with the theoretical values obtained in an infinite or in a semi-infinite medium, observed strain data should be carefully interpreted, taking into consideration the factors which may disturb the strain field.

In relating the output of the strainmeter to the local or the average strain change in surrounding rocks, we must define the strain carefully. The local strain field must be affected by local structure. If we are interested in the strain field in a broader area, we must consider not only the subsurface structure but also the surface topography. The procedure to connect the strainmeter output to the actual crustal strain will be different depending on what kind of strain we intend to study. We think the best way to measure the strain of our objective area is by comparing strains measured in some other ways with the output from the borehole volume strainmeter in order to determine the empirical coefficient connecting them. Usually this is performed by comparing Earth tides measured by borehole volume strainmeters with the expected tides obtained by using forecasting computer programs.

Another problem is what kind of data we want. The output of a strainmeter that responds to input over a very wide period range include the effects of artificial ground movements, variations in atmospheric pressure, tides, rainfall, underground water movements, changes in underground temperature, earthquakes, and other crustal movements. Usually, only one or two signals are wanted. We must cut out all unnecessary signals from outputs and extract information. Therefore, we must examine how the instrument reacts to each cause. The first causes to study are the effects of the atmospheric pressure and rainfall. In early experiments with Sacks-Evertson strainmeters these effects were investigated *[Sacks and Evertson, 1968; Sacks et al., 1969]*. One result was that the pressure-induced noise is at least an order of magnitude larger than the usual Earth noise in the period range of from one hour to three minutes, and that the signal-to-noise ratio is remarkably improved by suitable processing. Rainfall and water movement in a local aquifer or joint system can cause a more serious effect on the strain field, with observed strain changes much greater than expected for an elastic medium, sometimes by a factor of several hundreds. These changes have time lags and their mechanism is not known very clearly *[Sacks et al., 1969]*, though these conclusions may not apply everywhere. The data processing will be different for each place where the instruments are installed.

The borehole strainmeter is sensitive to DC and this gives a possibility of catching, if any exist, the precursors of a great earthquake, but even changes due to magmatic intrusions into magmatic chambers near great volcanoes. The borehole network installed near Mt. Vesuvius and in the Campi Flegrei region is mainly intended for this latter purpose. Besides this, the borehole strainmeter gives important data for the study of slow earthquakes . It has shown that slow and normal earthquakes are characterized only by their different time scales, that fore-slowquakes, the main-slowquake and after-slowquakes exist, and that stress drops of fore- and after-slowquakes are different. It was also shown that stress redistribution by slow earthquakes may prepare for the next earthquake. This stress redistribution will play an important role in earthquake prediction, but it has also been suggested that stress redistribution does not always begin long before the occurrence of a great earthquake *[Sacks et al., 1978, 1981]*.

The dilatometer is a peculiar kind of strainmeter, which measures a single component (dilatation) of strain: it is depicted into Figure 3.6, where it is illustrated its basic principle of operation. The sensing volume is filled with an (ideally) incompressible degassed fluid (silicone oil). The sensing volume is nearly filled with solid aluminum to decrease the volume of oil: this lowers the thermal sensitivity of the sensor and decreases loss of sensitivity due to the oil's compressibility. A second bellows-differential transformer-valve assembly is added to ensure no data loss when the valves are opened to equilibrate the instrument, since only one valve can be open at a time. As the cylinder is deformed, oil is forced in or out of the attached bellows; the top surface of the bellows (B1 and B2) correspondingly move up or down. That motion is monitored by differential transformers (DT1 and DT2). For a given strain, the bellows moves a distance proportional to the sensing volume divided by the bellows cross-sectional area. That ratio is very large (~40,000) and so the instrument provides high hydraulic (noise free) gain. This results in the instrument's having great sensitivity. To keep the strainmeter within its operating range over indefinite time intervals, a valve is opened for a few seconds as needed to allow oil to flow to or from a reservoir (R) that is decoupled from the strain field.

Figure 3.7 – Schematic representation of the basic principles for the Sacks-Evertson strainmeter. The strainmeter is connected to the rock by grout so that the resilient body of the instrument is compressed and can then accurately follow subsequent changes in deformation of the surrounding rocks.
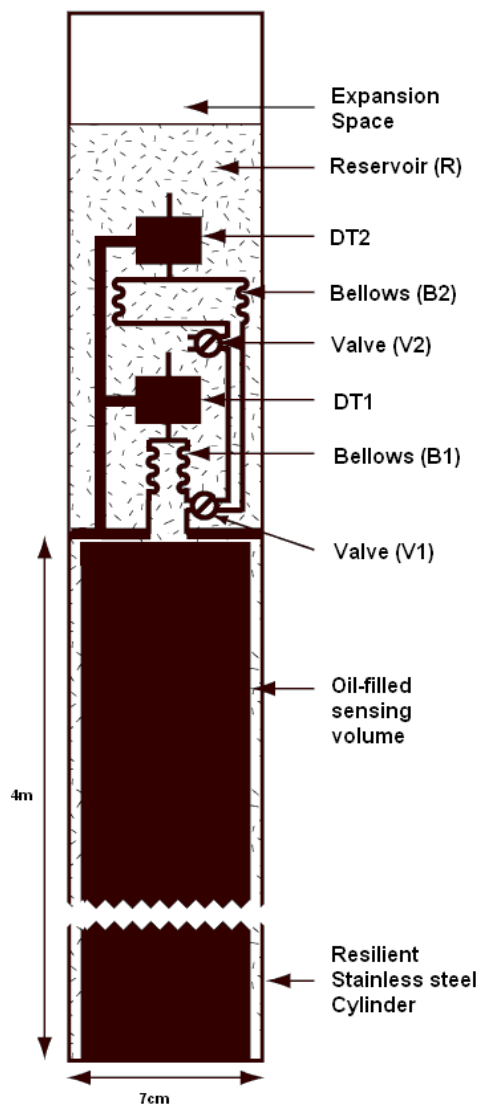
The primary signal for strain changes is from a DT (DT1) monitoring the position of a 2 cm-diameter bellows (B1). The B1-DT1 subunit frequency response to strain is constant from 0 to >10 Hz. The sensitivity is ~10^{-12} in strain with a maximum range of ~10^{-5}. The design allows for larger changes by incorporating a valve (V1) controlled by the electronic package. When V1 is opened, oil flows from or into the sensing volume allowing B1 to return to the equilibrium position. The combination of V1-B1-DT1 was the complete subunit for monitoring the strain changes in the original Sacks-Evertson design. It is expected that the instrument will experience a long-term strain rate so that B1 will continue to move slowly away from the equilibrium position. Both to preserve dynamic range for short-term excursions and to obtain lower noise performance, the bellows are maintained close to equilibrium. If the B1 signal level is higher than a specified value, the electronic control unit will open V1 and then close it again.

Because the instrument response remains constant over the seismic frequency range (order of hertz), the bellows experiences the strain changes caused by seismic waves. For large or nearby earthquakes, such strain changes may exceed the maximum range of B1. The electronic control unit continuously checks that B1 is in a safe operating range. If the strain level becomes >60% maximum, V1 is immediately opened to prevent damage. Since this may happen when an earthquake occurs, it could be possible to lose valuable data while the valve is open. To avoid such data loss, a second monitoring subunit has been installed inside the instrument. The exit port from V1 does not connect directly to the oil reservoir but, rather, to a second, larger-diameter bellows (B2). The position of that 5 cm-diameter bellows is monitored by a second DT (DT2); a second valve (V2) allows oil to flow between B2 and the unstressed reservoir (R). Whenever V1 is opened and closed, V2 will subsequently be opened after a time delay. Additionally, the output from DT2 is continuously checked and it is kept close to its equilibrium position using the same logic as for DT1. During normal operation the control system does not allow both valves to be open at the same time. Thus the sensing volume is always closed from the reservoir so that we are constantly recording the strain changes. Of course, the sensitivity of the DT2 is reduced by a factor of ~7. Under the common open condition, there is normally no substantial change in the strain condition; only during the emergency high-level condition are we likely to have significant strain changes. But having a temporary gain decrease is of no real concern since the primary sensitivity is so high. When both valves are closed (the usual state during operation), B2-DT2 is monitoring the volume of a fixed mass of oil which is decoupled from the Earth's strain field. DT2 output then gives a measure of temperature change at the installation depth. The system parameters are such that instruments are able to measure temperature changes with a sensitivity of about 10^{-5}°C.

If the volume of oil entering in a bellows due to a strain change is much smaller than the total volume of oil moved by the strain change itself, the fluid inside the bellows can be considered a purely incompressible liquid, hence oil density inside the bellows doesn't change with the pressure acting on the whole strainmeter. The sensing volume, so, is given by:

$$v_s = v_s^0 (1 + D) \tag{3.2.2}$$

where v_s^0 is the oil volume in the sensing area of the instrument when no deformations are occurring, while *D* is the dilatation measured by the instrument. The bellows volume is:

$$v_b = v_b^0 + A_b q \qquad (3.2.3)$$

with v_b^0 volume of the resting bellows, A_b effective area of the bellows and q displacement of its free side. Since it is assured the conservation of mass before and after deformation, we obtain:

$$\left(\frac{\rho}{1 + p_s/k_s}\right) v_s^0 (1 + D) + \rho(v_b^0 + A_b q) = \rho(v_s^0 + v_b^0) \qquad (3.2.4)$$

where ρ and k_s are, respectively, the density and the bulk module of the oil, while p_s represents the pressure to which is subject the oil, which is:

$$p_s = \frac{k_b}{A_b} q + \frac{128 \eta L_t A_b}{\pi b_t^4} \dot{q} \qquad (3.2.5)$$

where the first term derives from the pressure produced by the bellows with elastic constant k_b, while the second is produced by the pressure along the capillary tube, assuming a laminar flow; L_t is the length of the whole instrument, b_t its diameter and η the dynamical viscosity of the fluid. If $p_s \ll k_s$, from (3.2.4) and (3.2.5) we obtain:

$$q\left(1 + \frac{k_b v_s^0}{A_b^2 k_s}\right) + \dot{q}\left(\frac{128 \eta L_t v_s^0}{\pi b_t^4 k_s}\right) = -\frac{v_s^0}{A_b}. \qquad (3.2.6)$$

For long period, the term in $\dot{q}$ is negligible, while the value:

$$K_H = \left(1 + \frac{k_b v_s^0}{A_b^2 k_s}\right)^{-1} \qquad (3.2.7)$$

represents the correction for the fluid compressibility inside the sensing volume.

The capillary tube that connects the lower part with the bellows plays a fundamental role: it protects the instrument from the high accelerations caused by a nearby earthquake, since it behaves as a low-pass filter attenuating the responses at high frequencies. The cut-off frequency depends on the size of the duct and on the viscosity to the liquid. It can be proved *[Evertson, 1977]* that the cut-off frequency is:

$$f_t = \frac{b_t^4 k_s}{256 K_H \eta L_t v_s^0}. \qquad (3.2.8)$$

Usually, the cut-off frequency is about 1 Hz.

The instrument response depends even on the relation between the deformation of the instrument D and that of the surrounding rocks Δ. For a perfectly flexible instrument, the equations for an empty hole show that *[Evertson, 1977]*:

$$D = \left(\frac{2 - \nu}{1 - \nu}\right) \Delta \qquad (3.2.9)$$

where ν is the Poisson module of the surrounding rocks. An approximate solution *[Evertson, 1977]* of the problem of an elastic tube cemented into a well shows that the areal strain is 90% of the volumetric strain that there would be in an empty well, then the above equation remains valid even when an instrument lies inside a well.

In general, the deformation measured by the dilatometer could not be the same exerted by the surrounding rocks. The reason is that the crustal rocks where the instrument is inserted into, are porous and filled of fluids. An increase in pore pressure causes an expansion of the rock, a decrease produces a contraction. The pore flow induces deformation even if no fluid is exchanged with the dilatometer, thus the response of the dilatometer coincides with the deformation of the surrounding rocks only if no fluids is involved in strain changes. In case pore pressure is actually present, the deformation of the instrument Δ^{inst} is *[Segall et al., 2003]*:

$$\Delta^{inst} = C_1(\Delta^\infty - C_2 p^\infty) \tag{3.2.10}$$

where Δ^∞ e p^∞ are, respectively, the deformation and the pore pressure far from the instrument, and C_1 and C_2 depend from poroelastic properties of the rocks.

Consider a cylindrical hole in a block of poroelastic material (Figure 3.7). If the block is compressed rapidly the pore pressure will increase and the hole will contract elastically. If the exterior boundaries of the block are held fixed and the fluid is allowed to drain the rock will contract. However, as the rock shrinks the borehole must expand, since the exterior boundary is fixed. Thus, the far-field strain is zero, the rock locally undergoes a volume decrease, but the borehole undergoes a volume increase.

Figure 3.8 - Thought experiment to illustrate the effect of pore-fluid flow on a dilatometer response (a). A block of fluid saturated rock with a cylindrical hole is compressed (b). With the external displacements fixed the fluid is allowed to drain. As the fluid drains the rock contracts and the hole expands (c) [Segall, 2003].
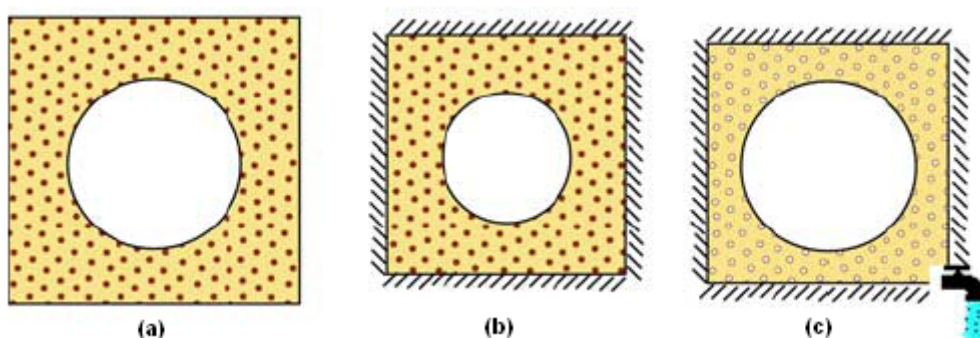
The frequency response of the mechanical section of the instrument depends on the viscosity and compressibility of the sensing oil and, in principle, the instrument can follow the strain changes with periods starting from few seconds to infinity. Its sensitivity depends on the amount of oil which goes up or down through the hole in the partition wall, and hence from the volume of the lower part, allowing strainmeters to record strain signals with frequencies belonging to a wide range.

Strainmeter installation is relatively simple, while its calibration is harder because of the impossibility of completely know rocks surrounding the instrument and the bad coupling rock-instrument: in this case, in fact, the measured strain field won't be the true rocks strain field, but however a value averaging it with the strain field caused by the grout.

The local strain field measured by the strainmeter can, moreover, be modified by various external factors: change in barometric pressure, rainfalls, local groundwater, anthropogenic activities.

In designing and implementing dilatometers, it must be taken into account the coupling of the instrument to the surrounding rocks and the characteristics of materials used, both for effects of temperature and, in volcanic environments, for possible effects of the presence of corrosive media. Dilatometers are placed in wells to isolate them as much as possible by temperature changes: as an example, just consider that, for periods of order of the day, an instrument placed 1 m below the Earth's surface records signals with an attenuation of temperature effects ranging from 50 dB up to 100 dB, while a well insulated instrument placed on the surface has an attenuation of only 30 dB. For longer periods (one year or so), attenuation is reduced to 2-6 dB for meter in depth: for an installation depth of 30 m, we could find attenuation for temperature effects of 70-170 dB.

Seismic phenomena in the Earth above 1 Hz can be measured very well with seismometers, while the lower frequencies are less prone to be measured with accelerometers or velocity transducers expressly created for strong motions or transient waves. For frequencies less than 1 Hz, there is a peak in Earth noise (microseisms) at about 0.17 Hz. Earthquakes frequencies can extend from above 1 Hz down to the lowest frequency of free oscillations of the Earth, at about 3.5×10^{-4} Hz. Long period seismometers, used for studying frequencies below 0.1 Hz, are self-noise limited by their response to thermal disturbances even in very good subsurface vaults. It is especially in the frequency range below 0.1 Hz that strainmeters become valuable.

The lowest frequency alternating phenomena known to be of interest is the approximately 12 hours for the M_2 and 24 hours for the O_1 lunar and solar induced Earth tides. Therefore, we will examine the frequency range from 10^{-5} Hz to 1 Hz when measuring waves within this frequency range. For any strainmeter operating within 30 m or so of the surface, a least detectable strain of 10^{-12} seems adequate because of Earth noise. For an upper limit for borehole strainmeters, 10^{-5} is easily achieved. The combination of valve – bellows – differential transformer allows the measurement of secular strain: annual changes in Earth strain of much interest, are measured by DT, which can record them within a wide range. Lower measured limit varies according to how good is the coupling instrument-surrounding rocks, signal-to-noise ratio in the installation region, fluid and aquifer presence, as well as the instrument inner structure: anyway, minimum strain values depend from the background ambient noise. Seismic / geodetic frequencies are as follow: above 0.5Hz main source is represented by body waves as well as local sources (machinery, wind blowing through the trees, and so on); from 0.5Hz down to 0.05Hz, main source is represented by microseisms; form 0.05Hz and 10^{-3}Hz, noise is due to crustal deformation caused by barometric pressure. Below 10^{-5}Hz, we are in range frequencies related with waves with a wavelength of the order of the week, month or

higher, which are related with astronomical motions or thermoelastic deformations, changes in pore pressure, wandering fluid in the rocks. Lower frequencies represent the secular strain of the Earth.

3.2.2 – The Strainmeters array near Mt. Vesuvius and Campi Flegrei caldera

The network of strainmeter installed near Mt. Vesuvius and Campi Flegrei caldera has been developed thanks to the joint efforts of prof. R. Scarpa, from Università degli Studi di Salerno (Italy), along with prof. S. Sacks and prof. A. Linde, from the Carnegie Institution of Washington DC (USA).

The Campi Flegrei area and Mt. Vesuvius are already instrumented by the Osservatorio Vesuviano – Istituto Nazionale di Geofisica e Vulcanologia (INGV). Since many years, distance changes (in an EDM network), leveling (referenced to benchmark I in Naples), gravity, GPS and seismic data are recorded.

Starting from 2004, the DIVNA (Dilatometers at Mt. Vesuvius – Naples) project started in the Campi Flegrei – Vesuvius volcanic areas. The project was designed to complement the seismic and geodetic monitoring system of the Osservatorio Vesuviano through the installation of a small network of 6 borehole (about 200m deep) stations, each one instrumented with a Sacks-Evertson volumetric strainmeter, as well as a broadband 3-components seismometer (some sites were equipped with a Teledyne Geotech KS2000BH borehole seismometer, while the remaining where equipped with a Guralp CMG-3T surface seismometer). Data logging, recording and telemetry is assured through the use of a Kinemetrics Quanterra Q330 24-bit A/D data-logger for each station. Every data-logger is equipped with a Kinemetrics Baler14 external storage system, buffering up to 20Gb data in MSEED packets, providing recording and storage capabilities to each station.

Signals coming from the network are centralized at two different data acquisition centers, formed by high capacity storage units (HP MSA 1500, 2.7TB), through ADSL telephonic lines, allowing an almost-real time data analysis. A cluster HP Proliant DL140 consisting of 15 PC HP 3.4GHz dual processors 3GB RAM, working with parallel Red Hat Linux software, is used for real-time signal processing.

Each borehole station is far several kilometers from other stations, and the network covers many strategic distances from Campi Flegrei and Vesuvius volcanoes.

The first installed strainmeter, was a prototypal instrument, which has been installed during October 1998 in the Vesuvius region *[Scarpa et al., 2000]*, and was named Q01: it was installed south of the Vesuvius cone, in Camaldoli Della Torre village.

The network is depicted into Figure 3.6, while more details about their installation are provided into Table 3-1.

Figure 3.9 – Sacks-Evertson volumetric strainmeter network installed by Università degli Studi di Salerno around the Campi Flegrei – Mt. Vesuvius volcanic areas near Naples, Southern Italy.
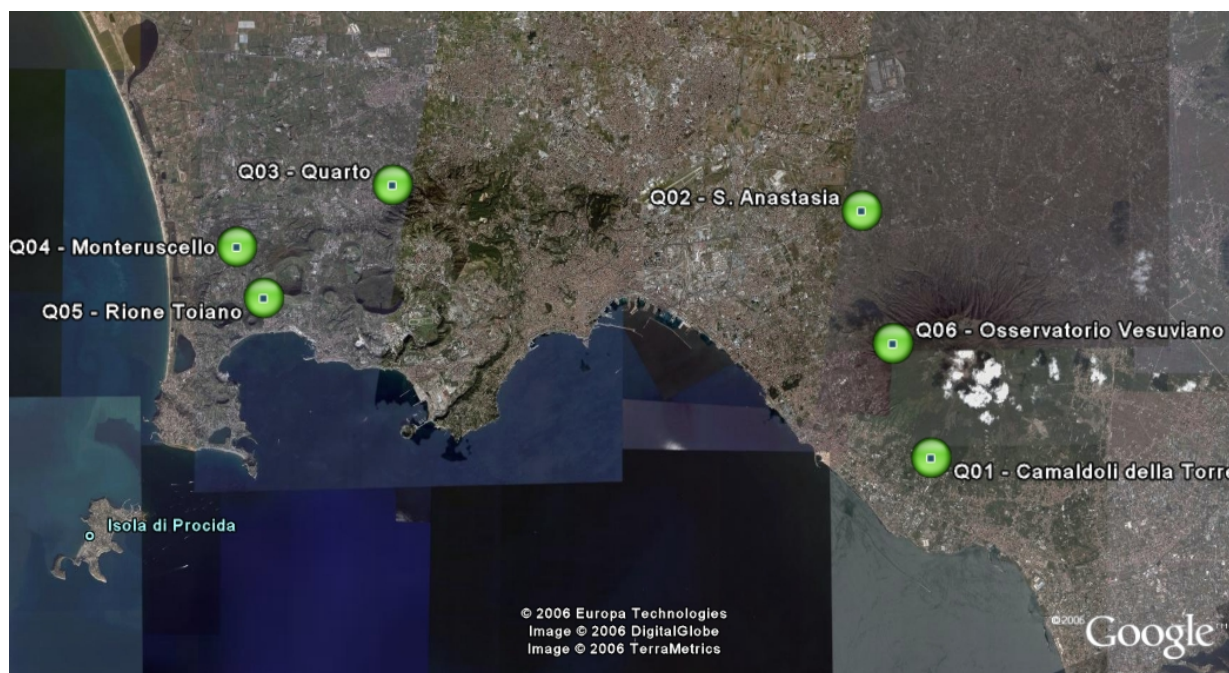

Table 3-1 – Strainmeters locations

Location	Lat N	Lon E	Depth (m)	Lithology	Place
Camaldoli della Torre / CMDT Q01					
	40° 46.771	14° 24.527	123	Volcanic sediments and lavas	Acquedotto Vesuviano
S. Anastasia / SANA Q02					
	40° 42.590	14° 22.870	150	Volcanic sediments and lavas	Sede Protezione Civile
Quarto / QUAR Q03					
	40° 53.121	14° 09.336	180	Tuffs	S.M.S. C.E. Gadda
Pozzuoli – Monteruscello / MRUS Q04					
	40° 51.752	14° 04.824	140	Tuffs	S.M.S. A. Diaz
Pozzuoli – Rione Toiano / RITO Q05					
	40° 50.634	14° 05.615	120	Tuffs	S.M.S. S. Quasimodo
Osservatorio Vesuviano / OSVE Q06					
	40° 49.650	14° 23.800	150	Volcanic sediments and lavas	Sede Storica OV

The Sacks-Evertson strainmeters (about 7cm in diameter, 4m in length) provide two output signals, obtained by two different hydro-mechanical amplifiers. The high-sensitivity output integrates the volumetric change in the strained reservoir. The low-sensitivity one is connected to the strained reservoir only when the instrument is sensing a rapid and strong strain change, thus measuring strain. Usually the low-sensitivity channel measures the pressure in a closed cell, that is proportional to local temperature. The temperature resolution is a few micro-degrees. Air pressure is also measured. Nominal resolution of the Sacks-Evertson strainmeter is about 10^{-11} strain units, nominal dynamic range is $10^{-11} - 10^{-3}$. Low-frequency calibration of installed strainmeters is obtained by comparison with Earth tides *[Hart et al., 1996]*. A preliminary calibration of the recorded signal provides a sensitivity of the instruments 2×10^{-11}. Seismic signal, high- and low-sensitivity strain signals are continuously recorded, and sampled at 100Hz.

3.3 – Tiltmeters

An improved Michelson tiltmeter uses three or more water depth sensors along a half-filled water pipe (100-500 m long) to provide independent measures of tilt to test for signal coherence resulting from Earth-attachment noise. The primary tilt signal is derived from the two ends, but two signals with half the tilt amplitude can be formed by differencing combinations of end and central transducers. The multiple vertical displacement sensors permit instrumental noise to be distinguished from real tectonic tilt. The system yields data of comparable quality to dilatometers or borehole strainmeters at periods 20 minutes to DC.

3.3.1 – Precise tilt measurements

The geometry of the Michelson tiltmeter *[Michelson and Gale, 1919]* found favor in the 1970s from investigators seeking a tiltmeter with sub-microradians long-term stability and immunity to tilt noise near the Earth's surface *[Wyatt et al., 1984; Agnew, 1986]*. A Michelson tiltmeter is characterized by a reference datum consisting of continuous equipotential surface between water and air in a horizontal pipe in isothermal, constant volume conditions, such as may be approximated in underground pipes. The 100-500 m long water pipe described is horizontal and rigid and has an internal diameter of 15 cm. Two orthogonal 500 m pipes provide a complete measurement of the tilt vector.

Because of the large volume coefficient of thermal expansion of fluids and gasses particular attention must be paid to minimizing the influence of environmental temperature changes on the measured tilt signal. Of the various arrangements adopted for measuring tilt relative to the local geoid, that adopted by Michelson provides the greatest immunity to moderate thermal variations occurring along the path of the pipe. Filled tube systems, though providing higher frequency response, must be maintained precisely level and at uniform temperature to achieve similar noise levels *[Beaven and Bilham, 1977]*.

In Michelson's original design, interferometric sensors at each end provided a photographic measure of height change of a buried vault relative to the water surface. The availability of lasers permitted fringe-counting electronics to be incorporated into later designs *[Bilham et al., 1979; Plumb et al., 1979]*, and had the advantage of a sub-micron digital output, but the disadvantage of losing fringe-lock during local earthquakes due to disturbance of the water surface *[Behr, 1992]*. A white-light, fringe-follower microprocessor-controlled, interferometer has been incorporated into the tiltmeter at Pinion Flat Observatory *[Wyatt et al., 1984]* to overcome the ambiguity resolution inherent in monochromatic interferometers, and to provide an absolute measure of the height of the water surface provided by a screw-thread micrometer. A float system was introduced to monitor tilt in the Long Valley tiltmeter in 1994, which following a satisfactory demonstration of stability and sensitivity was replicated in Acapulco in 1999 *[Kostoglodov, 2002]*. The present design also uses float sensors whose vertical positions are monitored by Linear Variable Differential Transformers (LVDT) with a range of ±6 mm and a nominal noise level of 0.1 μm. In Figure 3.9 it is depicted the actual scheme for the LVDT-float sensor.

Figure 3.10 – Schematic view of float sensor. A flexure strip holds the float and LVDT core precisely centered. Mechanical instability of the reservoir does not contribute directly to measurement noise. The transducer has a range of 3 mm or ±6 mm depending on the pipe length.
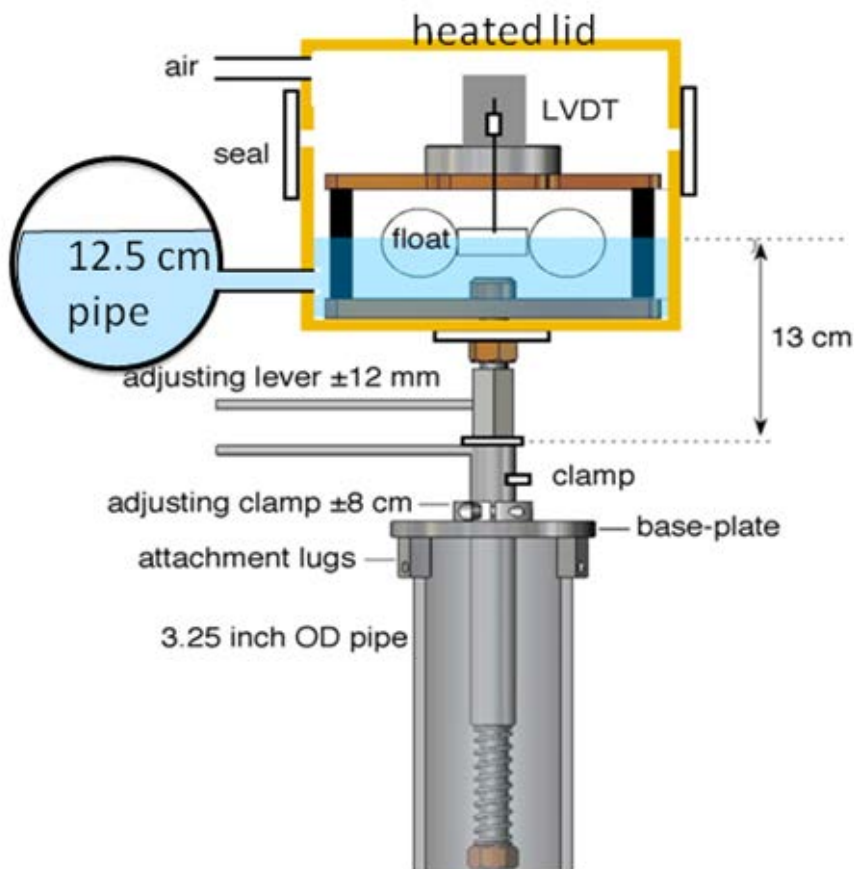

The tiltmeter is referenced to the Earth in three places using steel piles driven to refusal (see Figure 3.10 for further details). A back-hoe or an engineering quality pile driver is used to drive the pile for this critical monumentation. Minimum pile length is 5 m, and the maximum may be as much as 50 m, with a corresponding increase in wall thickness. The minimum recommended diameter pipe used for 10 m piles is 7 cm with 5 mm wall thickness. Deeper piles need to be larger and thicker. By fastening the measurement sensors directly to the top of these piles (as shown in Figure 3.9), the water pipe and reservoir materials are excluded from the measurement loop, and sub-micron measurements become possible. In the current design a coarse adjustment of ±8 cm is available, plus a fine adjustment of ±12 mm to an accuracy of 0.3 mm.

The water and air paths from the horizontal water pipe are leg to each sensor via short flexible tubes attached by shut-off valves. Typically these tubes are 1-2 cm in diameter. An inspection window and built in light emitting diodes (LEDs) permit sensor centering to be checked without disturbing the instrument.

The sensors are typically accessed within a 1.5 m diameter subsurface, vertical hollow, corrugated steel vault driven into the ground around each pile. Brick or cement-cylinder vaults are also possible. In practice the sensors rarely need to be accessed after installation, and when they do, adjustment can usually be accomplished in less than a few minutes.

In a high resolution recording system, 16 bit data are acquired from the LVDT that senses the water height at rate of 16 samples per second and is digitally filtered with a 64 s time constant. In the low resolution version 12 bit data are sampled each second and averaged, stored and / or transmitted at 10 minutes intervals. The high sampling rate suppresses pipe and float resonance which would otherwise result in aliasing of the recorded data. The fundamental resonance of the water in the 500 m pipe is ~23 minutes, consistent with gravity-wave propagation with a water depth of approximately 6 cm. A 100 m pipe has a resonance of ~4 minutes, and 40 m pipe ~2 minutes. Filled tube tiltmeters in contrast can be designed to be critically damped with 500 m, 100 m or 40 m path lengths using pipe diameters of less than 1.5 cm, and fundamental resonances of less than 1 minute.

Figure 3.11 – An important feature of the tiltmeter is the introduction of a central transducer at the mid-point of each water pipe. This arrangement yields two independent measures of tilt in the water pipe, a property that permits signal coherence to be estimated. Data are sampled at 1 s intervals and digitally averaged. They are then transmitted to a local computer once each minute via a radio modem, or are transmitted directly to a cell link at hourly intervals for retrieval from a data website.
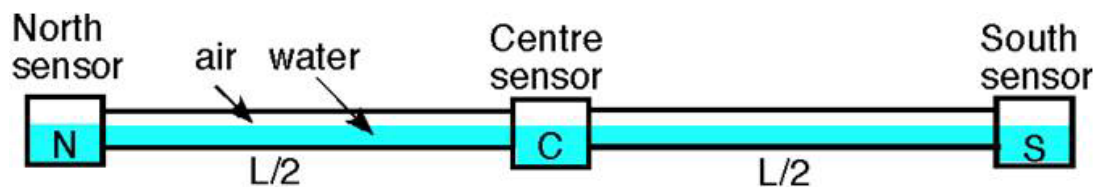
Each sensor of the 16 bit system can be operated from solar power and because the data are transmitted to a central recorder via radio modem no cables link the sensor vaults. A central computer located less than 5 km from the sensor records these data every 10 s to 1 minute, and a telephone modem or internet link permits the data to be accessed remotely.

In the low resolution system a 12 bit data logger feeds a cell phone transmitting system whose data are available for public or private access on the web within a few minutes to less than 2 hours of acquisition. This second system has advantages for public relations purposes requiring transparency in operation, since the calibration data can be placed in the ASCII data header and the data are available to all interested parties immediately. The telemetry method enables the sampling rate, filtering time constants and transmission rate to be modified remotely (transmission every 10 minutes if needed), and also permits the user to set alarm levels remotely.

Tiltmeters data quality is very high. Sub-microradian stability is typically available within days of start-up. Noise level largely depends on the site – hard-rock sites being quieter (<50 nrad at 20 s), and sedimentary basins near large cities or railroads being noisy. Thin layers of sediment over bed rock provide the ideal combination of pipe-installation ease and monument stability.

3.3.2 – Measuring water height changes through the use of the LVDT

Linear displacement is movement in one direction along a single axis. A position or linear displacement sensor is a device whose output signal represents the distance an object has traveled from a reference point. A displacement measurement also indicates the direction of motion.

Linear variable differential transformers (LVDT) are used to measure displacement. LVDTs operate on the principle of a transformer. As shown in Figure 3.11, an LVDT consists of a coil assembly and a core. The coil assembly is typically mounted to a stationary form, while the core is secured to the object whose position is being measured. The coil assembly consists of three coils of wire wound on the hollow form. A core of permeable material can slide freely through the center of the form. The inner coil is the primary, which is excited by an AC source as shown. Magnetic flux produced by the primary is coupled to the two secondary coils, inducing an AC voltage in each coil.

Figure 3.12 – General LVDT assembly
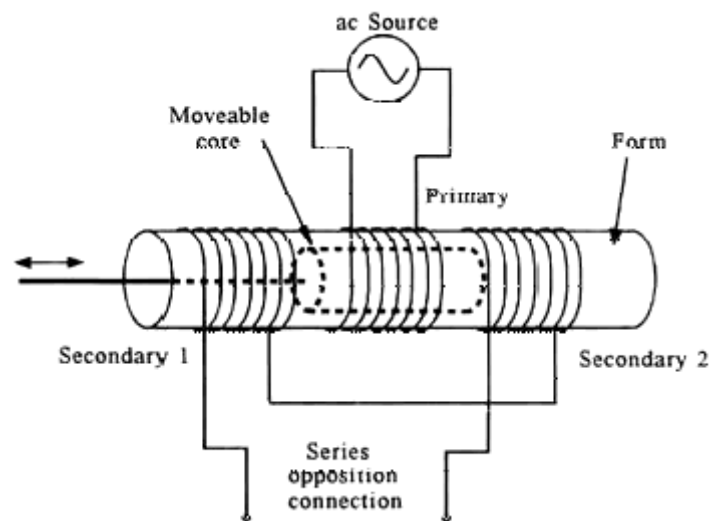
The main advantage of the LVDT transducer over other types of displacement transducer is the high degree of robustness. Because there is no physical contact across the sensing element, there is no wear in the sensing element.

Since the device relies on the coupling of magnetic flux, an LVDT can have infinite resolution. Therefore the smallest fraction of movement can be detected by suitable signal conditioning hardware, and the resolution of the transducer is solely determined by the resolution of the data acquisition system.

An LVDT measures displacement by associating a specific signal value for any given position of the core. This association of a signal value to a position occurs through electromagnetic coupling of an AC excitation signal on the primary winding to the core and back to the secondary windings. The position of the core determines how tightly the signal of the primary coil is coupled to each of the secondary coils. The two secondary coils are series-opposed, which means wound in series but in opposite directions. This results in the two signals on each secondary being 180 deg out of phase. Therefore phase of the output signal determines direction and its amplitude, distance.

In Figure 3.12 it is depicted a cross-sectional view of an LVDT. The core causes the magnetic field generated by the primary winding to be coupled to the secondaries. When the core is centered perfectly between both secondaries and the primary, as shown, the voltage induced in each secondary is equal in amplitude and 180 deg out of phase. Thus the LVDT output (for the series-opposed connection shown in this case) is zero because the voltages cancel each other.

Figure 3.13 – Cross-sectional view of a LVDT core and windings
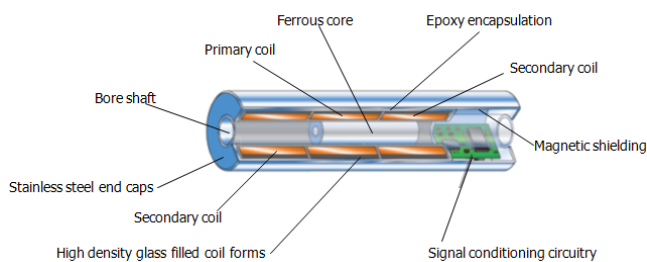
Displacing the core to the left causes the first secondary to be more strongly coupled to the primary than the second secondary. The resulting higher voltage of the first secondary in relation to the second secondary causes an output voltage that is in phase with the primary voltage. Likewise, displacing the core to the right causes the second secondary to be more strongly coupled to the primary than the first secondary. The greater voltage of the second secondary causes an output voltage to be out of phase with the primary voltage.

To summarize, the LVDT closely models an ideal zeroth-order displacement sensor structure at low frequency, where the output is a direct and linear function of the input. It is a variable-reluctance device, where a primary center coil establishes a magnetic flux that is coupled through a center core (mobile armature) to a symmetrically wound secondary coil on either side of the primary. Thus, by measurement of the voltage amplitude and phase, one can determine the extent of the core motion and the direction, that is, the displacement. The Figure 3.13 shows the linearity of the device within a range of core displacement. Note that the output is not linear as the core travels near the boundaries of its range. This is because less magnetic flux is coupled to the core from the primary. However, because LVDTs have excellent repeatability, nonlinearity near the boundaries of the range of the device can be predicted by a table or polynomial curve-fitting function, thus extending the range of the device.

Figure 3.14 – Proportionally Linear LVDT Response to Core Displacement
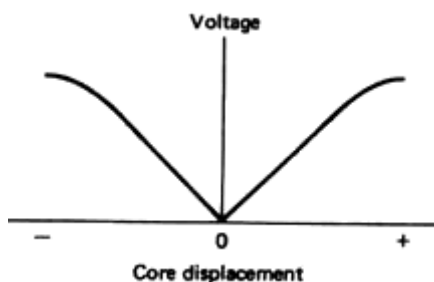
Because the output of an LVDT is an AC waveform, it has no polarity. The magnitude of the output of an LVDT increases regardless of the direction of movement from the electrical zero position.

In order to know in which half of the device the center of the core is located, one must consider the phase of the output as well as the magnitude as compared to the AC excitation source on the primary winding. The output phase is compared with the excitation phase and it can be either in or out of phase with the excitation source, depending upon which half of the coil the center of the core is in.

The signal conditioning electronics must combine information on the phase of the output with information on the magnitude of the output, so the user can know the direction the core has moved as well as how far from the electrical zero position it has moved.

LVDT signal conditioners generate a sinusoidal signal as an excitation source for the primary coil. This signal is typically between 50 Hz and 25 kHz. The carrier frequency is generally selected to be at least 10 times greater than the highest expected frequency of the core motion. The signal conditioning circuitry synchronously demodulates the secondary output signal with the same primary excitation source. The resulting DC voltage is proportional to core displacement. The polarity of the DC voltage indicates whether the displacement is toward or away from the first secondary (displacement left or right).

The induced voltage is proportional to the displacement of the core, as stated by the equation *[Neubert, 1975; Herceg, 1976]*:

$$\Delta V_i = K_l q \left(1 - \frac{q^2}{L^2} \right) \tag{3.4.1}$$

where q is the displacement of the core from the center of the LVDT, K_l is the sensibility of the LVDT (voltage / distance), L is the length of the primary coil. This equation has been obtained choosing a high magnetic permeability of the core, a small space among coils, and both ends of the core are inside the secondary coils. The voltage ΔV_i can be considered linear in respect to the core displacement if $q \ll L$. In this case:

$$\Delta V_i \cong K_l q. \tag{3.4.2}$$

3.3.3 – The Tiltmeters network near Campi Flegrei

Starting from March, 2008, near the Campi Flegrei caldera, two long baseline tiltmeters were installed thanks to the cooperation of Università degli Studi di Salerno (Italy), represented by prof. R. Scarpa, and the Cooperative Institute for Research in Environmental Science – CIRES at University of Colorado at Boulder, represented by prof. R. Bilham.

The Campi Flegrei area, hence, was equipped with two tiltmeters to completely overlook, record and analyze the strain tensor.

The two instruments installed form a small array of water-pipe tiltmeters with lengths between 28 m and 278 m in tunnels near the region of inflation and defilation associated with subsurface magma chamber activity. The objective of the measurements is both to monitor volume changes in subsurface magma system, and also to monitor possible changes in the ensemble rheology of the magma and its confining rock. The first requires instruments immune to local sources of non-tectonic noise, and the second requires sensors capable of monitoring onshore tilts resulting from the rich spectrum of tidal and seiche loading in the Bay of Pozzuoli at 1 to 20 cycles per day.

The array of tiltmeters installed contains two instruments, the North Tiltmeter (PTNO) and the South Tiltmeter (PTNS). An in-scale representation of instruments is depicted into Figure 3.15.

Figure 3.15 – Placement of the two instruments in respect with the Pozzuoli town, and their current length. Instruments are in scale.

Instruments have a total of 12 sensors, and are formed by 5 pipes (two for the PTNO instrument, and three for the PTNS one), with a total length of 577 m. Their installation has been done into former Italian Navy tunnels, at a mean depth of 15 m, which is particularly useful both for seismic noise reduction and thermal stability. The measured resolution for the four main pipes is reported into Table 3-2.

Table 3-2 – Tiltmeters features

Resolved Component	Length (m)	Period (minutes)	Resolution
NS North Tunnel	285.4	7.5	0.07 nrad
EW North Tunnel	99.3	2.7	0.22 nrad
NS South Tunnel	58	1.8	0.33 nrad
EW South Tunnel	43	1.8	0.8 nrad

An example of installation is depicted into Figure 3.16, while geometric characteristics of both tiltmeters are reported into Figure 3.17.

Figure 3.16 – In this picture it is shown the North tiltmeter installed near Pozzuoli: on the wall it is visible the pot where the NN sensor is installed. Picture points southward.

Figure 3.17 – Geometric characteristics for the two tiltmeters installed near Pozzuoli.
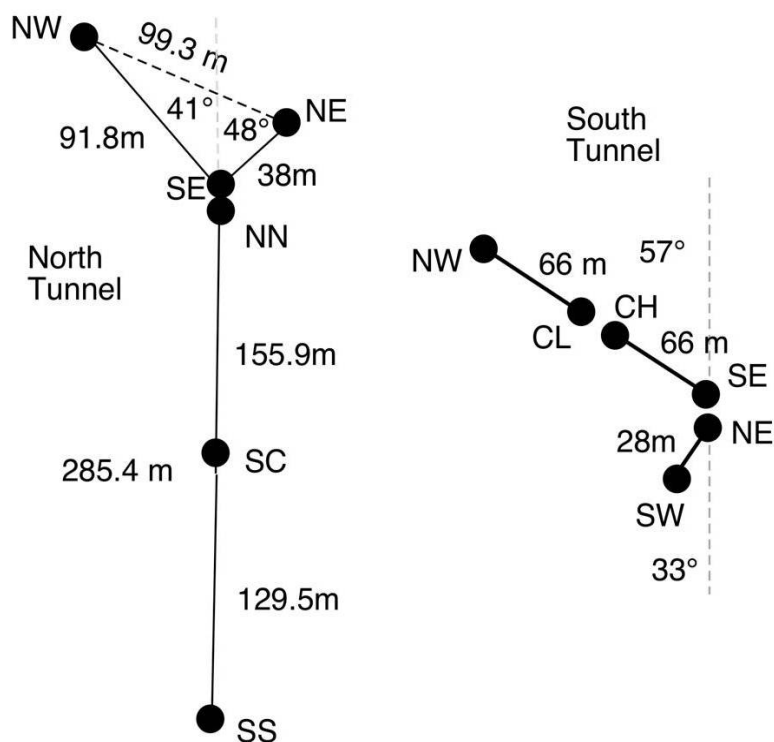
In respect with the strainmeter array, the tiltmeters are much more closer to the center of the caldera.

Chapter 4 – Data analysis and conclusions

As seen in previous chapters, strainmeter (or, using a more correct term, dilatometer) and tiltmeter data can be used to monitor Earth's crust deformations: these can occur for many different reasons (crust subduction near subduction zones, Earth tides, changes in barometric pressure, local or teleseismic earthquakes, and other), but near volcanoes deformations can occur even because of magmatic intrusion in magmatic chambers which modify the local strain field, which can then be measured by both kinds of instruments.

Analysis of data coming from strainmeters installed in volcanic regions has already led to noticeable results evidenced by the seismological community: the most important and even most studied set of data comes from the Hekla volcano, located in Iceland. Various studies *[Linde et al., 1993; Agustsson et al., 2000]* have shown how it is possible to have a correct forecast for a future volcanic eruption by using the data coming from strainmeters. A small network of Sacks-Evertson strainmeters was installed in southern Iceland in 1979 with the objective of monitor strain changes and the volcano Hekla was in the study area: the nearest installed site (BUR) was 15 km away from the volcano. At the time of the 1980 eruption, only analog chart records of strain were available and these had significant gaps, but the eruptions in 1991 and 2000 were both well recorded on telemetered digital records. Analysis of the January 1991 eruption was reported by Linde and others *[1993]*. All the more distant strainmeters showed extensional strain changes during the approximately two days during which the eruption was most active; however, the nearest station (BUR) drew a more complicated record, with large rapid contraction during the first two hours followed by expansion for the next two days. From an expanded time scale plot, it was clear that the strain changes at BUR started about 30 minutes before the eruption. The February 2000 eruption of Hekla *[Agustsson and others, 2000]* was somewhat smaller than that in 1991, but the strain records were remarkably similar, indicating that both eruptions took place with essentially the same geometry: when strain changes were recognized to be similar to those recorded nine years before, a warning was sent to the nearest airports, and flights were suspended, which led to a considerable money and life saving.

On the basis of the Icelandic experience, a similar approach was tried even in Campi Flegrei / Vesuvius volcanic region, in order to achieve similar results and build a forecasting and early warning system in case of imminent volcanic eruptions.

The network of installed instruments has been described in previous chapters, while in the current section we will focus on the acquisition and analysis of strain and tilt data recorded by the installed strainmeters and tiltmeters.

Data analysis will be divided into two section: in the first part, we will analyze data coming from the strainmeter network, while in the second part the data recorded by the two long baseline tiltmeters will be examined.

4.1 – Strain data analysis

For the strain data analysis, we can start by using a known signal. Since the inducing potential can be easily identified, the deformation signal due to Earth tides can be used as a reference signal to know strainmeter response in the diurnal and semi-diurnal range in order to calibrate them.

Calibration is useful to correctly interpret deformation data, even if it could be a task hard to achieve. The instrument usually is calibrated in laboratory prior than its in situ installation, but instrument deformations don't represent true local rock deformation. Well, cement and instrument itself constitute an inhomogeneity in rocks which distort local strain field.

The comparison of the tidal signal recorded by the instrument and the one generated through numerical simulations could not provide a proper calibration of the instrument: in fact the instrument's output, which responds to signals over a wide frequency range, includes signals of various types (anthropogenic, atmospheric , weather, changes in subsurface temperature, ocean loading, and so on) which can be a source of noise for the deformation signal within the tidal frequencies range. A correct calibration, hence, is obtained only if it is known the source of noise and which could be its effects. Once noise effects are known, it is possible to remove them from the recorded data, by using a specifically developed software. In our analysis, barometric pressure and thermal effects are taken in account.

4.1.1 – Tidal simulation software

Some of the analysis methods were developed during 1970s: harmonic representation of experimental signals, which uses a frequency domain switch of input data, used the Cartwright – Tayler – Edden theory. Mean square techniques have been used so long to design numerical filters in order to divide true tidal signal from noise, but this step is hard to achieve when noise lies in the same frequency range of tidal harmonics.

A non-harmonic method was deployed by Munk and Cartwright *[1966]*. Unlike traditional harmonic methods for tidal analysis, this method expresses the tide as the sum of past, present and future values taken from a relatively small number of input functions that vary over time. This method has the advantage, compared to the harmonic method, to provide the possibility of separating the admittance of the different species of tidal spherical harmonics and may represent the effects of noise caused by changes in regional and local weather.

Currently one of the most used method for the tidal analysis uses a combination of harmonic and non-harmonic techniques, and is used even by the tidal analysis software mostly used by the scientific community, the BAYTAP-G program. Basically, the harmonic method is used for the tidal components, while the non-harmonic method is used to express nonstationary processes, like barometric pressure and thermal effects.

Another Earth tide analysis program is the package ETERNA *[Wenzel, 1996]*, which allows the adjustment of tidal and meteorological parameters from Earth tide observations, the computation of Fourier spectra, and the visualization of observations, residuals and spectra. The pre-processing program (PRETERNA) uses a remove-restore technique: first all known signals, that is, computed model tides and air pressure influence sampled at 5 min intervals, are removed, then the remaining signal is destepped, deskipped, and degapped, and the known signals are then added back.

Both BAYTAP-G and ETERNA always require evenly sampled data. They assume Gaussian distribution of the fit residuals and give excellent results when this a priori hypothesis is approximately correct. This is not a problem when analyzing 'usual' records, but both codes are sensitive to the presence of outliers, as in the case of strong signals such as slow earthquakes or eruptions. If data contaminated by some event are removed, computed tides and atmospheric effects relevant to the time span in which the event occurred could be inaccurate and affect modeling and physical interpretation.

The analysis of deformation data in seismically active regions, such as Campi Flegrei or Mt. Vesuvius regions, Amoruso et al. *[2000]*, realized a new procedure based on a non-linear regression technique: an hybrid model which includes both harmonic and non-harmonic terms was embedded into the Analisi program, which allows to analyze data set as a whole, even if there are gaps inside data.

As usual in power spectra estimations and as already done by several authors *[Agnew, 1981]*, an evenly spaced sequence is first pre-whitened by generating a first-differences sequence or by applying a nearly equal ripple derivative (NERD) filter, whose transfer function more closely approximates that of a time derivative. Pre-whitening is recommended since deformation noise is usually red, that is, its power spectral density increases as frequency decreases. Low-frequency noise is the most difficult to deal with since it has a statistically non-null mean value: pre-whitening lower low-frequency noise, making fitting more reliable. As regards rapidly changing signals such as spikes and steps, the former are rendered symmetrical with respect to the underlying signal, reducing their effects on the fitting procedure, while the latter are transformed into spikes, which are highly dangerous if a least-squares procedure is used, but have only a small effect if a large-tailed distribution of residuals is assumed. In this case a different error function is minimized making the statistical estimation of the parameters less sensitive to large departures of a small number of data points from the idealized assumptions for which the estimators are optimized. If gaps in the experimental evenly spaced time sequence exist, it is first divided into segments of data without gaps. Each segment is independently pre-whitened, all the segments are then appended one after the other, and the resulting record is analyzed as a whole.

The computed time sequence to be fitted to the experimental one is a sum of

1. one or more polynomials, all of the same degree, but with different adjustable coefficients inside the parts into which the input sequence can be divided, for example, in the case of an abrupt change of slope or curvature;
2. up to five FIR filtered environmental sequences with unknown filter coefficients;
3. steps of variable amplitudes at known times;
4. ramps of variable amplitudes at known time intervals;
5. tidal harmonics of variable amplitudes, whether a simple sum of sine and cosine terms with the frequencies of the largest tides chosen according to the Rayleigh criterion, or wave groups from the Cartwright – Tayler – Edden or Tamura *[1987]* potential developments, together with quadrature terms.

4.1.2 – Preliminary analysis

Tides are induced by periodic, measurable forces: these characteristics of the tidal signal are very important, and allow to reproduce it by using numerical simulations, which involve a direct measurability even of the deformations related with tides themselves. On the other hand, from a dilatometer perspective, its high sensibility allows to record deformations generated by tides. The first scope of the current report, is, hence, to verify if sensibility of instruments installed in Campi Flegrei / Mt. Vesuvius is high enough to record strain associated with Earth tides. Once this has been verified, it will be possible to confront the tidal spectrum of recorded signal compared with numerical simulations. This kind of analysis is carried on through the following steps:

1. Choice of data set with specific characteristics, suitable for the subsequent analysis;
2. Data correction (detrending, degapping, despiking, and so on);
3. Data resampling (this step is done only when original sampling rate is too high in respect with searched frequencies);
4. Power spectrum of data sets;
5. Generation of theoretical tides and associated power spectrum;
6. Comparison of experimental and theoretical power spectra.

The above steps are needed in order to calibrate instruments, at least in tides frequency range. A complete calibration of dilatometers can be achieved only by performing calibrations in various frequency ranges, mainly one for the tidal frequency range (about $10^{-4} \div 10^{-5}$ Hz) and one for the seismic range ($1 \div 10^{-1}$ Hz): usually, in fact, changes in local strain field vary with frequency. In the current report, anyhow, we will focus mainly on the tidal ranges, hence only this kind of calibration will be explained and carried out, but the techniques used in this case are very similar to those needed in order to achieve calibration in other frequency ranges.

Choice of data set suitable for analysis

Due to gaps in strain data (mainly caused by data loss, electrical issues, errors in data-logging, and other similar concerns) it wasn't possible to perform analysis on data sets longer than three months. For the calibration, seven data sets where analyzed for the Quarto instrument, starting from January, 1st 2005, to

March, 31st 2006, while Rione Toiano and Monteruscello stations where analyzed both for one data set, coming from the first trimester of 2006.

An example of strain data is depicted into Figure 4.1.

Figure 4.1 – Example of a straingram measured at Quarto station (Q03). The original time series was sampled at 1 s, the one shown in the figure has been down-sampled at 1800 s.
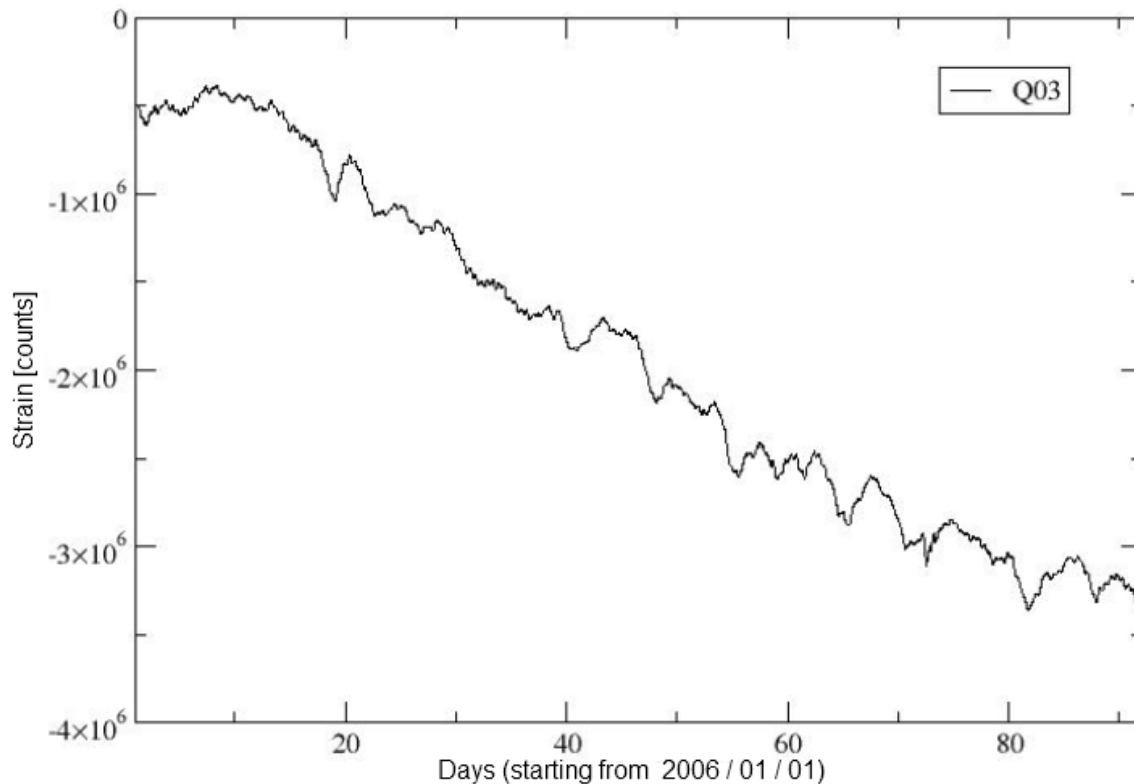
A typical straingram contains a superposition of waves with different frequencies, due to various phenomena, some of which could even not have a geophysical meaning (anthropogenic activities, electronic issues, opening and closing of valves in the instrument – this latter is a source of noise for the recorded signal, which could modify the frequency content of signal). The opening and closing of valves can be removed from the originally recorded signal by adopting a semi-automatic procedure which uses a linear interpolation procedure in order to re-join data sets before and after the opening (or closing) of valves. Similar procedures have been adopted to degap (missing data) or despike (electronic problems) recorded data.

After correcting data from spurious artifacts, time series have been down-sampled, because original sampling frequency is equal to 1 Hz. The down-sampling of data sets is required for both a simpler manipulation of straingrams and for purely theoretical reasons: since tidal components of interest – among all of those with lowest frequencies – have magnitude of the order of 10^{-5} Hz, low-pass filters and decimation procedures were applied to time series. Signals have been re-sampled with a higher sampling interval Δt which still resolves the maximum frequency needed in order to avoid aliasing issues: the maximum required frequency corresponds to semidiurnal components (2.3×10^{-5} Hz). It is possible to use a 1800 s (i.e., half an hour) sampling interval, since $\Delta t = 1800$ s $\Rightarrow f_{max} = 2.3 \times 10^{-4}$ Hz » 2.3×10^{-5} Hz. It is

important to note that each time series must be long enough to be down-sampled according to previous choices. Length of some data set wasn't compatible with the schema proposed above, hence, in those cases, lower Δt were chosen, or shorter data sets were discarded.

Finally, once data have been correctly down-sampled, a transformation of data has been performed in order to switch from time domain to frequency domain, by using Discrete Fourier Transforms (DFTs) algorithms. The power spectral density (PSD) of decimated time series was calculated, using a mobile window whose length depends on the total number of samples contained into the chosen data set: the PSD must be calculated, in fact, keeping in mind that the window used must contain a sufficient number of periods of the analyzing wave. The length of the moving window, hence, determines the smallest resolvable frequency and the resolution of the PSD itself. Deformation signal is a data set sampled at equal interval Δt, chosen so that the maximum resolved frequency – known as Nyquist's frequency – is higher than the maximum component frequency of the signal being sampled. If N is the number of samples in the chosen data set, then it is possible to estimate the Fourier transform only for discrete values of f:

$$f_n = \frac{n}{N\Delta t} \ge 0 \Rightarrow n = 0, \dots, \frac{N}{2}.$$

(4.1.1)

For each f_n, hence, we have an estimate of the power spectral density $P(f_n)$ which does not match the expected value, since f_n represents the mean value measured from n to $n+1$. Increasing the number of data for the sampled function (i.e., lowering the sampling interval) the estimate of $P(f_n)$ is enhanced, but the approximation error is not completely removed, since it doesn't depend from N. Moreover, the minimum distance for two frequencies is related with the total length of the data set T, following the equation:

$$\Delta f = \frac{1}{T}.$$

(4.1.2)

Next step in data analysis for calibration of strainmeters is the generation of the theoretical tides and their power spectral densities. Theoretical tides have been generated using a software which calculates the areal deformations (the same kind of superposition of components of the strain tensor measured by the dilatometers installed in Campi Flegrei and Mt. Vesuvius regions) in a specific point the Earth, once known latitude, longitude and height in respect to the reference geoid, starting from the harmonic development of the tidal potential coefficient contained into Tamura's catalogue *[1993]*. Theoretical tidal deformation is obtained assuming a spherically stratified Earth, non-rotating and without oceans. Once theoretical tides have been obtained for the same locations where dilatometers are installed and for the same time period of the chosen data sets, the power spectral density for the theoretical sets has been computed.

A comparison between the power spectral density of the experimental data set and of the theoretical tide has been performed, for the 12 hours components. The PSD for the theoretical tide is expressed in $(n\varepsilon)^2$/Hz: comparing it with the PSD of the chosen data set it is possible to gain information about the dilatometers sensitivity, obtaining the scale factor for the experimental data.

4.1.3 – Calibration of dilatometer data

In the following of the current paragraph, the results obtained for the dilatometers installed in Campi Flegrei and Mt. Vesuvius are shown: the comparison has been carried out for the 12-hours tidal component.

Data sets for the calibration have been chosen during the year 2006, not far from the installation of instruments in boreholes. Data quality varies from one instrument to another, and mainly depends from the quality of the installation. Strainmeters installed near Mt. Vesuvius record data of lower quality due to the worse coupling between the instrument and the borehole where it has been installed: this is caused by the surrounding rocks, which are usually the product of earlier eruptions (sediments and volcanic lavas, highly disaggregated). On the other hand, tuffs in which Campi Flegrei strainmeters were installed are much more cohesive and permit a far better coupling of the instrument with the rocks.

Mt. Vesuvius dilatometers

The data sets recorded at Mt. Vesuvius instruments (Camaldoli della Torre, Ercolano and S. Anastasia) belong to the period October – December 2006.

Two data sets coming from Camaldoli della Torre have been analyzed: the first one, of 16 days in length, starts on 2006/10/16 and lasts on 2006/10/31, while the second one is 13 days long, and goes from 2006/11/10 to 2006/11/22. From the spectral analysis for both data sets no 12-hours peaks was found: this is related with the poor rocks-instrument coupling and the result is that no calibration has been possible in this case. In Figure 4.2 it is shown the data sets used, while in Figure 4.3 it is depicted the PSD for the longest data set compared with the PSD calculated for the theoretical tides generated for the same time period.

Figure 4.2 – Deformation at Camaldoli della Torre station for chosen data sets.
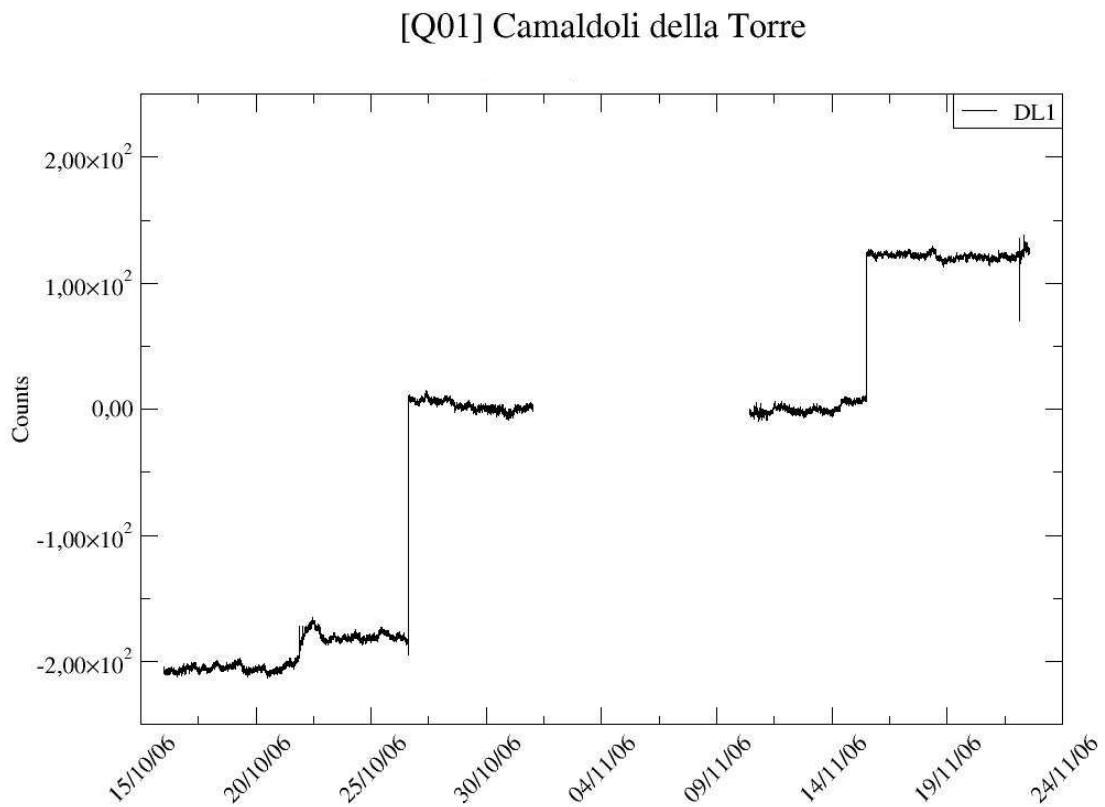
Figure 4.3 – Comparison of PSDs at Camaldoli della Torre for recorded data (black) and theoretical tide (grey)
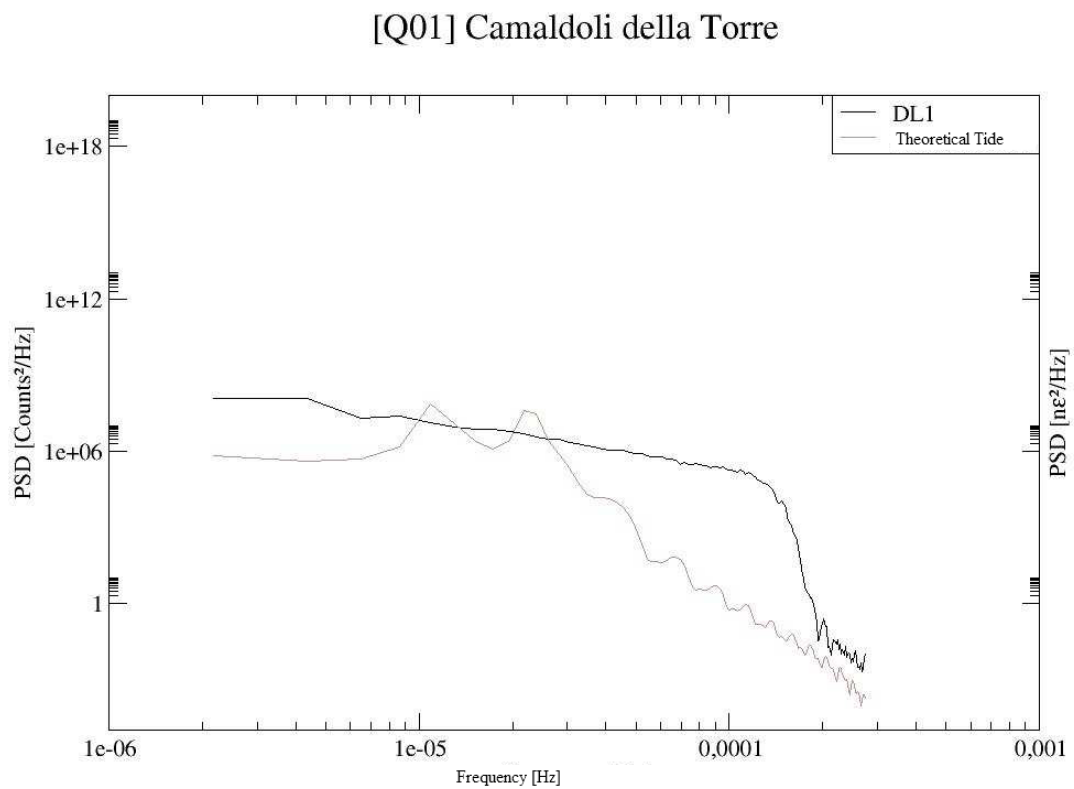
For S. Anastasia instrument, two data sets were used, one of 28 days (2006/08/01 – 2006/08/28) and one 16 days long (2006/09/04 – 2006/09/16). The measured PSD shows two small peaks for 24-hours and 12-hours tidal groups, very biased by local noises, but anyway somehow visible. Comparing these values with the peaks coming from the theoretical tides, it has been possible to calculate the scale factor used to pass from counts to nanostrain. Remembering that straingrams were recorded using a gain factor equal to 30, the final relation count-strain is:

$$1 \text{ count} \sim 4 \times 10^{-11} \text{ strain} \tag{4.1.3}$$

The Figure 4.4 shows recorded deformation for chosen data sets, while Figure 4.5 depicts the PSDs for both experimental data and corresponding theoretical tides for the longest period.

Figure 4.4 – Deformation at S. Anastasia station for chosen data sets.
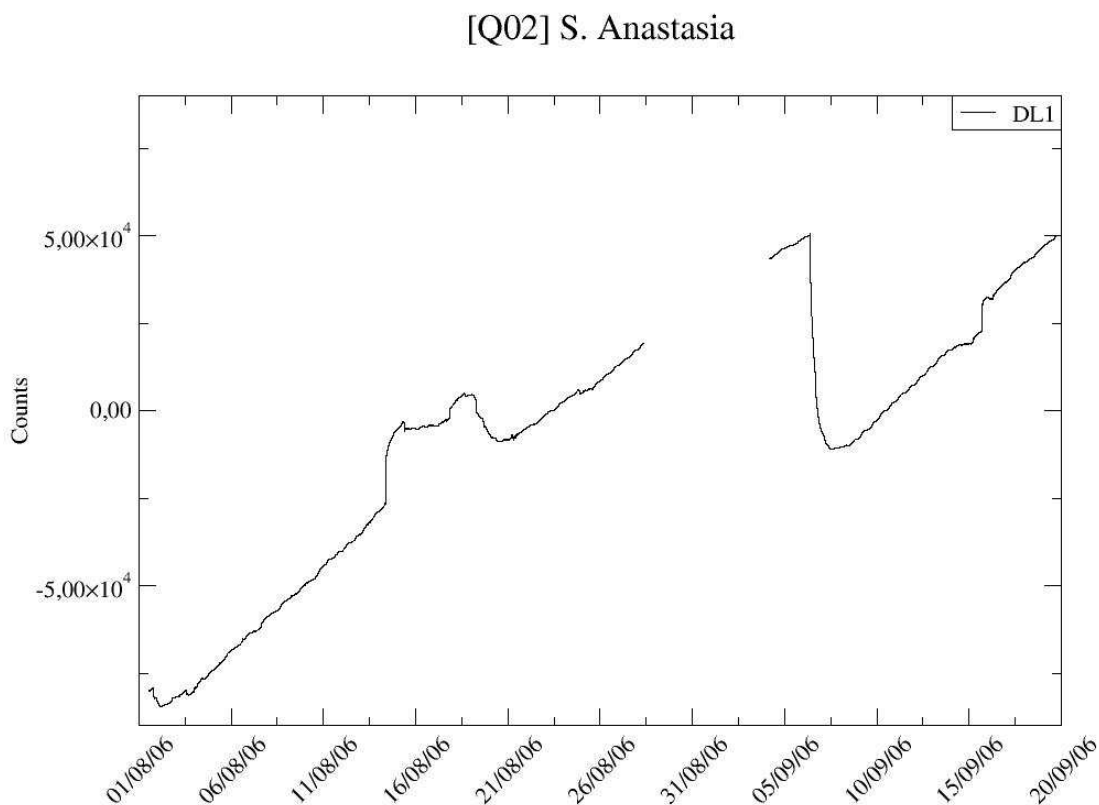
Figure 4.5 – Comparison of PSDs at S. Anastasia for recorded data (black) and theoretical tide (grey)

[Q02] S. Anastasia
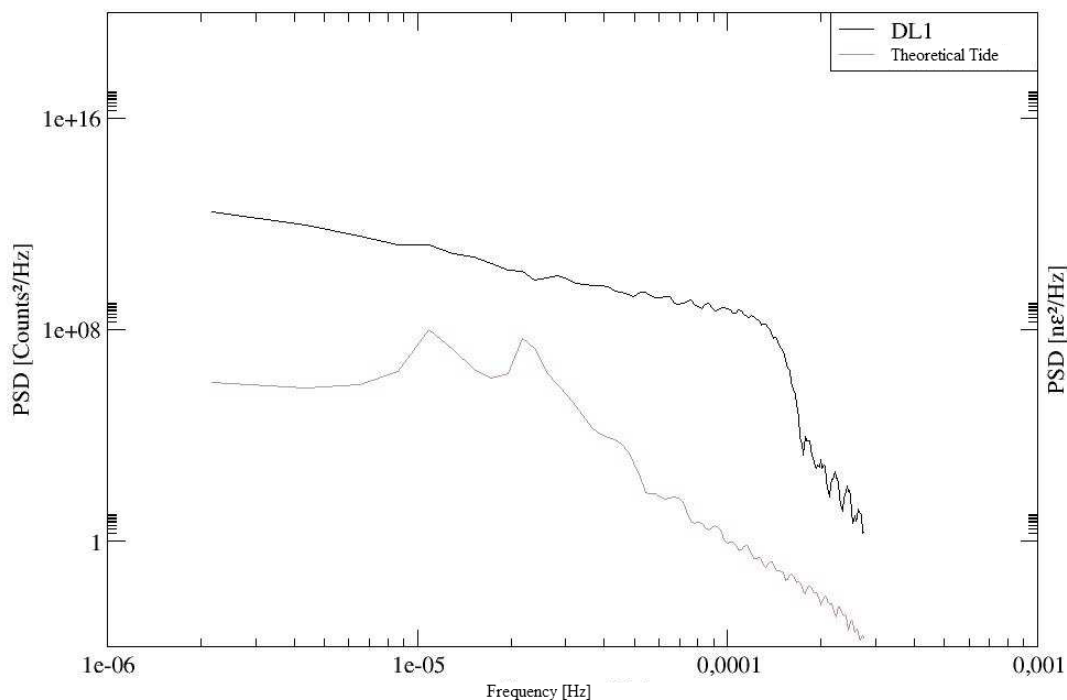
The Ercolano instrument is installed near the original Ossevatorio Vesuviano on the Mt. Vesuvius. From this station four time series were taken in account: the first starts on 2006/09/01 and ends on 2006/09/13 (13 days in length); the second starts on 2006/10/12 and ends on 2006/10/31 (20 days); the third starts on 2006/12/01 and ends on 2006/12/09 (9 days); the fourth starts on 2006/12/10 and ends on 2006/12/31 (22 days).

Just like in the previous case, even for the Ercolano instrument the PSD was measured for both experimental and theoretical data. In this case it was possible to find a relation between counts and strain:

$$1 \text{ count} \sim 6 \times 10^{-11} \text{ strain} \tag{4.1.4}$$

Even in this case we shows data and PSDs: in Figure 4.6 there are depicted the four data sets recorded by the instrument, while the Figure 4.7 shows the comparison between PSDs.

Figure 4.6 – Deformation at Ercolano station for chosen data sets.

[Q06] Osservatorio Vesuviano - Sede Storica
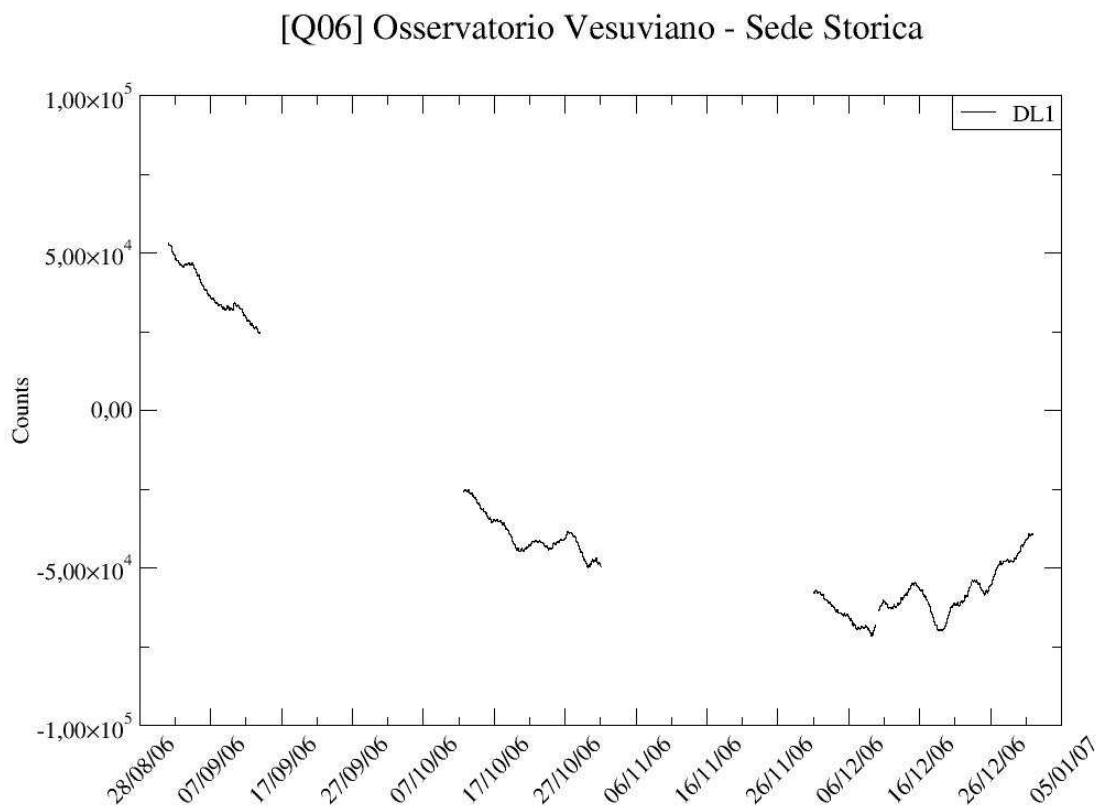
Figure 4.7 – Comparison of PSDs at Ercolano for recorded data (black) and theoretical tide (grey)

[Q06] Osservatorio Vesuviano - Sede Storica
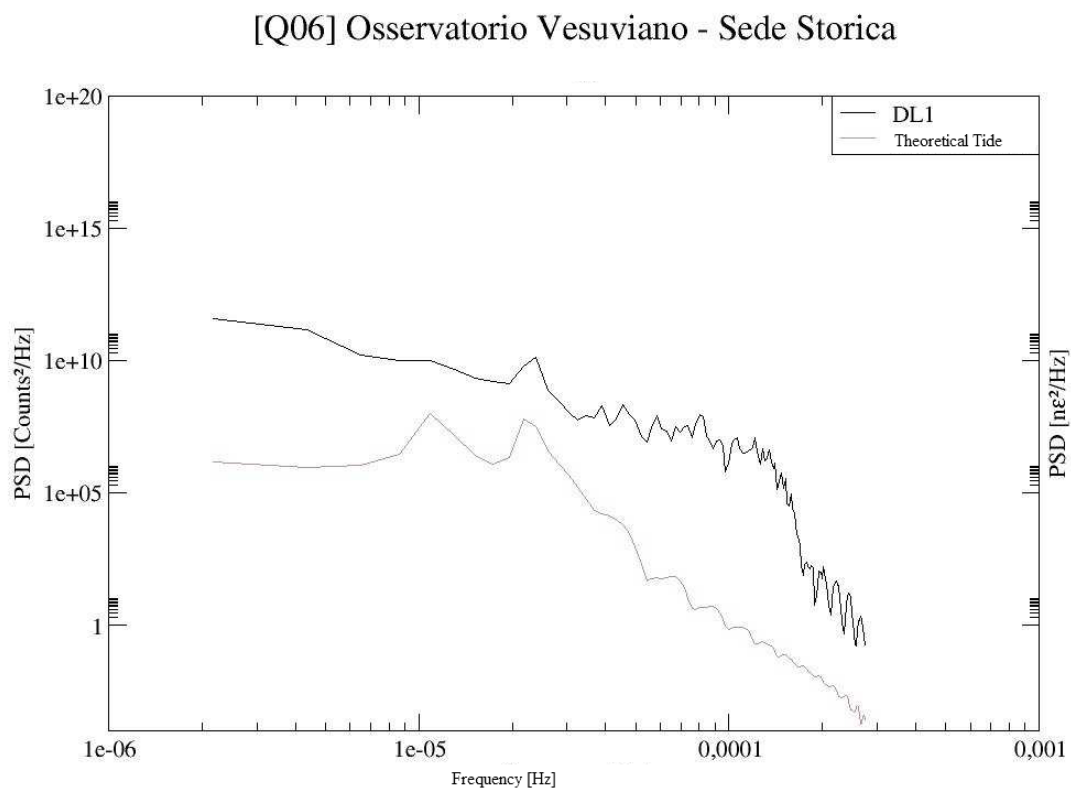
Calibration of instruments installed near Mt. Vesuvius, then, results in a effective sensitivity for dilatometers of the order of 10^{-11} strain for Camaldoli della Torre and Ercolano instruments.

For the Monteruscello instrument, it was taken in account a data set which starts on 2006/02/23 and lasts on 2006/03/29, 34 days in length.

In this case, no clear peaks are visible in the spectrum of the experimental data, which could be related much more with an increase in local noise than a bad coupling of the instrument with the surrounding rocks. A compressive strain trend is, anyway, clearly visible in the reported data.

In Figure 4.8 it is depicted the strain measured for the selected data set, while in Figure 4.9 it is reported the comparison of PSD calculated for experimental and theoretical data.

Figure 4.8 – Deformation at Monteruscello station for chosen data sets.
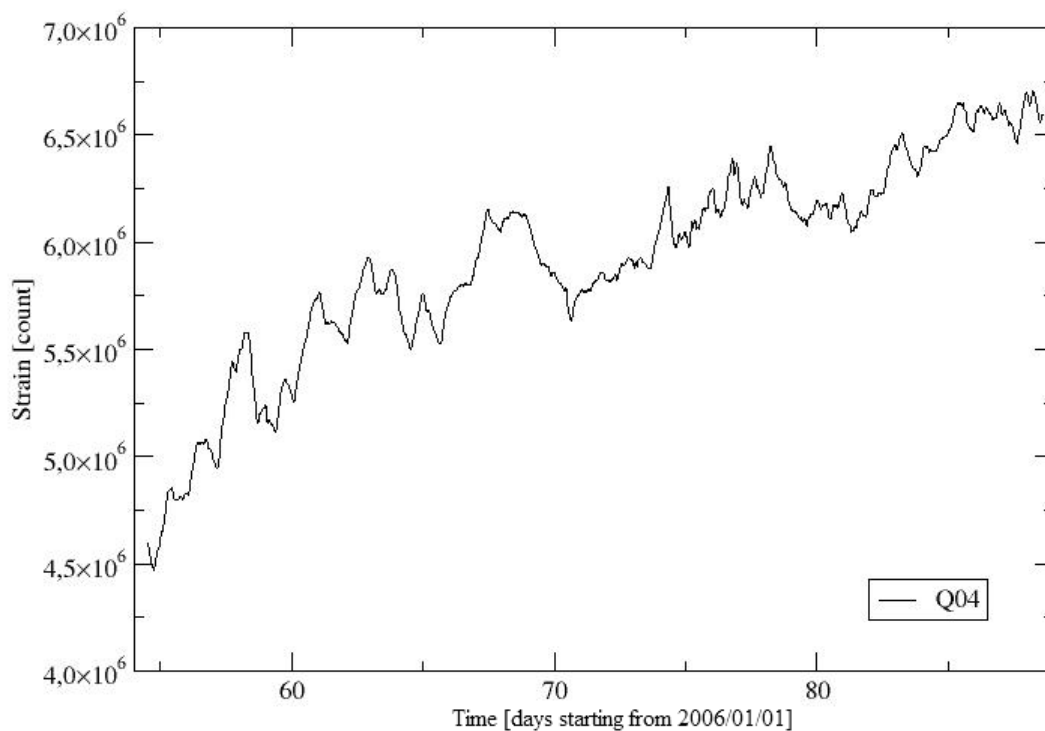
Figure 4.9 – Comparison of PSDs at Monteruscello for recorded data (black) and theoretical tide (red)
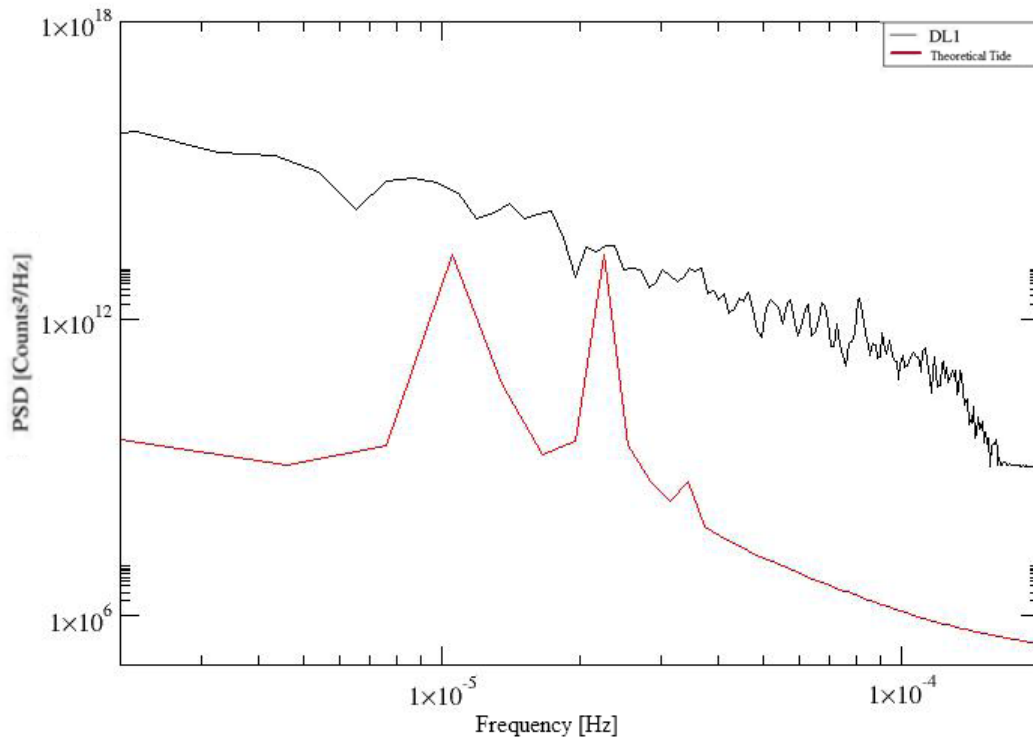
From the Rione Toiano time series it has been analyzed only one data set, which starts from 2006/01/01 and ends to 2006/03/31 (90 days).

In the spectrum for the selected data set it is clearly visible one peak for the 12-hours component and one peak for the 24-hours component. Moreover, thanks to the length of the data set, it is easily identifiable even a peak which corresponds to the 8-hours component of the measured tides. From the spectrum it is possible to estimate that the signal-to-noise ratio is about equal to 5, by comparing the amplitudes of the 12-hours component with the noise. By superimposing the PSD for the theoretical tides with the PSD measured using experimental data, we found that the scale factor is:

$$1 \text{ count} \sim 3 \times 10^{-11} \text{ strain} \tag{4.1.5}$$

where we took in account the gain factor set to 30 for the recorded data.

Even in this case, Figure 4.10 and Figure 4.11 depict, respectively, the data set analyzed and the comparison between data and theoretical tide of the PSDs.

Figure 4.10 – Deformation at Rione Toiano station for chosen data sets.
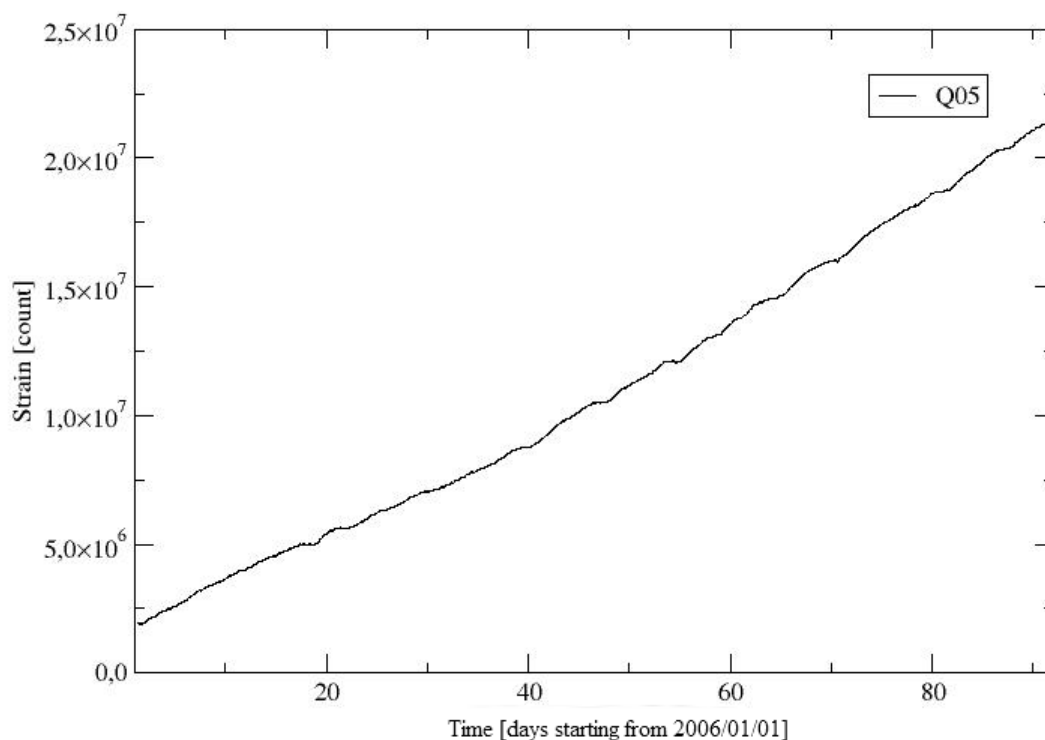
Figure 4.11 – Comparison of PSDs at Rione Toiano for recorded data (black) and theoretical tide (red)
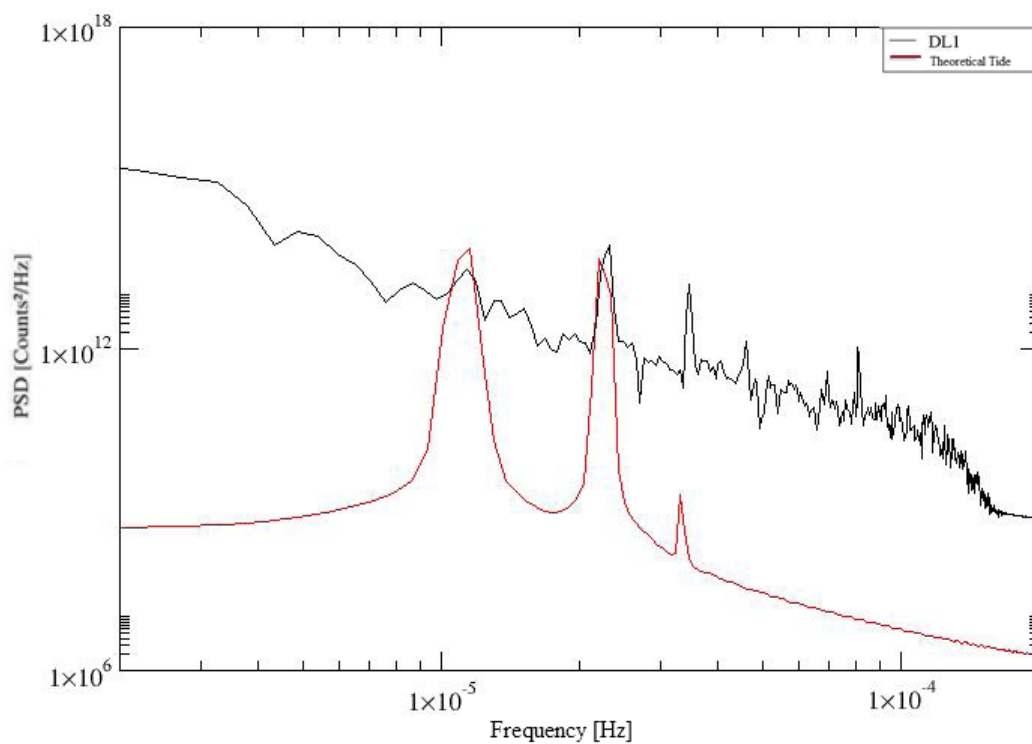
The last instrument analyzed is the dilatometer installed in Quarto. In this case the chosen time series are the following: from 2005/01/01 to 2005/01/18 (14 days); from 2005/01/31 to 2005/02/14 (15 days); from

2005/03/05 to 2005/03/31 (26 days); from 2005/04/19 to 2005/05/23 (34 days); from 2005/05/06 to 2005/07/20 (56 days); from 2005/07/23 to 2005/10/19 (88 days); from 2006/01/01 to 2006/01/31 (90 days). In the first four data sets the 12-hours peak wasn't found in PSDs. Even in this case it is possible to assume noise with a frequency similar to tides.

The data set which starts on 2005/05/06 and ends on 2005/07/20 (56 days), a PSD with a moving window of 15 days didn't give a peak for the M2 tidal component. From the straingram, however, it is possible to identify some spurious artifacts, probably due to electronic problems: these items weren't deleted because they have the same tidal frequency: the straingram is depicted in Figure 4.12, while the corresponding PSD is reported into Figure 4.13.

Figure 4.12 – Deformation at Quarto station for chosen data sets.
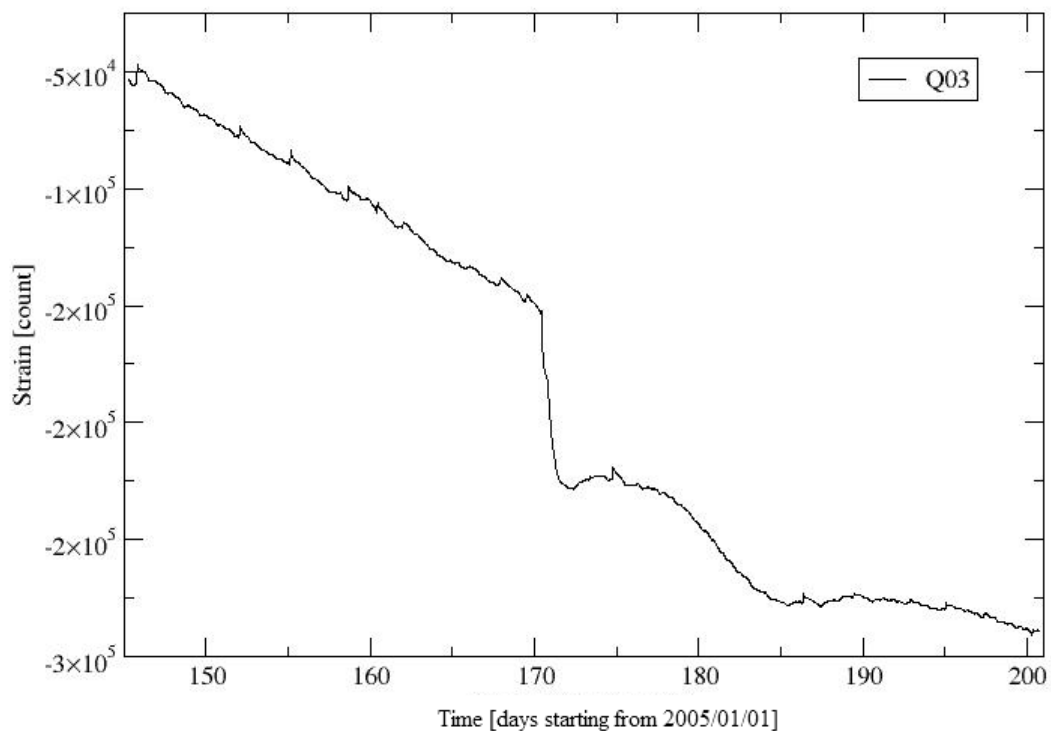
Figure 4.13 – Comparison of PSDs at Quarto for recorded data (black) and theoretical tide (red) for the period 2005/05/06 – 2005/07/20
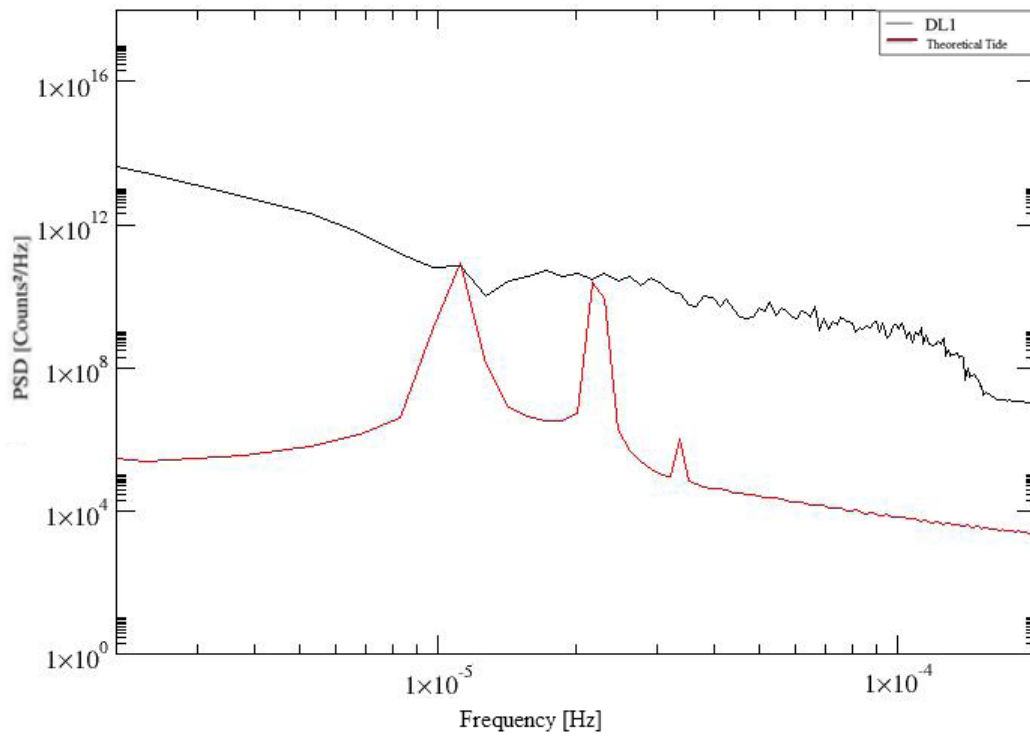
From the following data sets, however, it is possible to find better results. The set which starts on 2005/07/23 and ends on 2005/10/19 has been analyzed by performing a PSD with a moving window of 21 days. In the spectrum depicted in Figure 4.14 it is possible to identify the 12-hours tidal component with a signal-to-noise ratio of ~6. The relation count-strain in this case is equal to:

$$1 \text{ count} \sim 5 \times 10^{-11} \text{ strain} \tag{4.1.6}$$
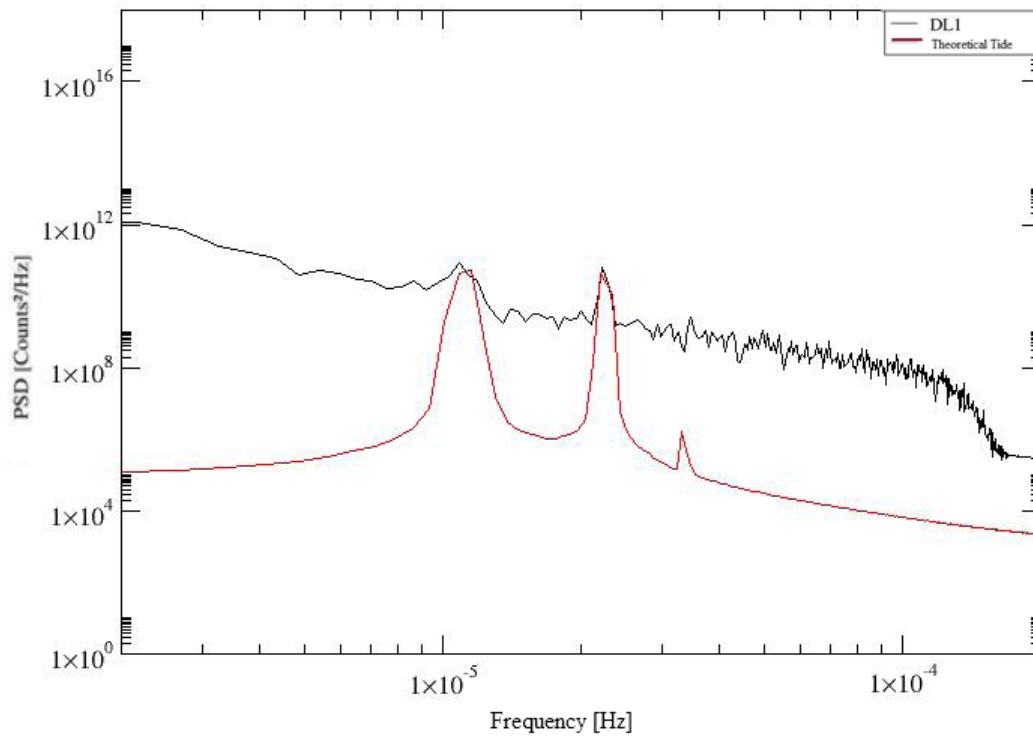
The last data set analyzed for the Quarto instrument starts on 2006/01/01 and ends on 2006/03/31 (90 days). In the PSD, calculated using a moving window of 21 days we found again the 12-hours tidal component, which returns a relation count-strain equal to:

$$1 \text{ count} \sim 6 \times 10^{-11} \text{ strain.} \tag{4.1.7}$$

dividing the obtained value by the gain factor of 30. The PSD graph is depicted in Figure 4.15.

Figure 4.15 – Comparison of PSDs at Quarto for recorded data (black) and theoretical tide (red) for the period 2006/01/01 – 2006/01/31
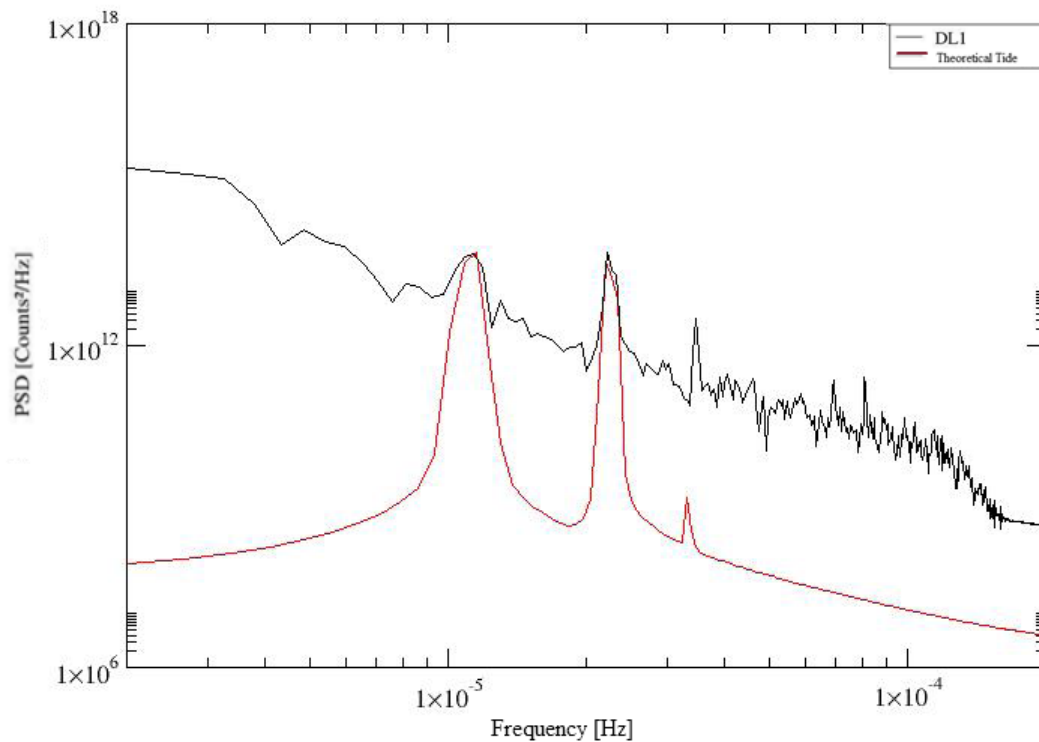
From this information it seems like the coupling improves with time: this could be related with an improvement of the coupling between instrument and surrounding rocks.

4.1.4 – Tidal Analysis

Starting from the above preliminary analysis, we can use the instruments which have good sensitivity to Earth tides in order to analyze them on experimental data. Data will be analyzed only for instruments with a good coupling with the surrounding rocks, which means that the three instruments at Mt. Vesuvius need improvements to be used for this kind of analysis. On the other hand, the instruments installed at Campi Flegrei satisfy the needed parameters. Of course, only some data sets will be taken in account: the chosen time series will be improved by removing gaps, electronic noises, and all of the other sources of noise which could alter the data set. Moreover, barometric pressure and thermal effects which alter data sets will be removed too. The software Analisi will be used to achieve these purposes.

Firstly, the correct data sets have been chosen, among those shown in the previous section. Then data has been pre-whitened: this is a mandatory step, since deformation associated noise is red – i.e., its PSD increases when frequency decreases – and low frequency noise has a statistical mean value not null. The pre-whitening generates prime differences of the data set, which reduces low frequency noise and makes fits more reliable.

Figure 4.16 – Strain (black) and barometric pressure (green – in arbitrary units) recorded at Quarto station for the period 2005/09/22 – 2005/10/19.
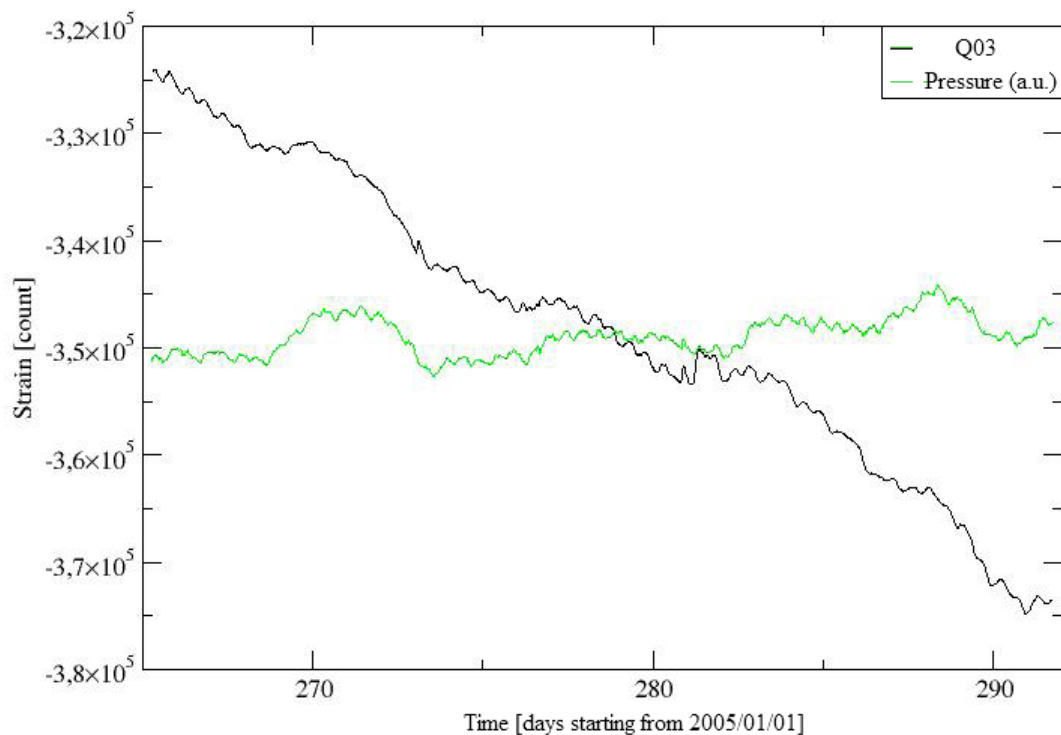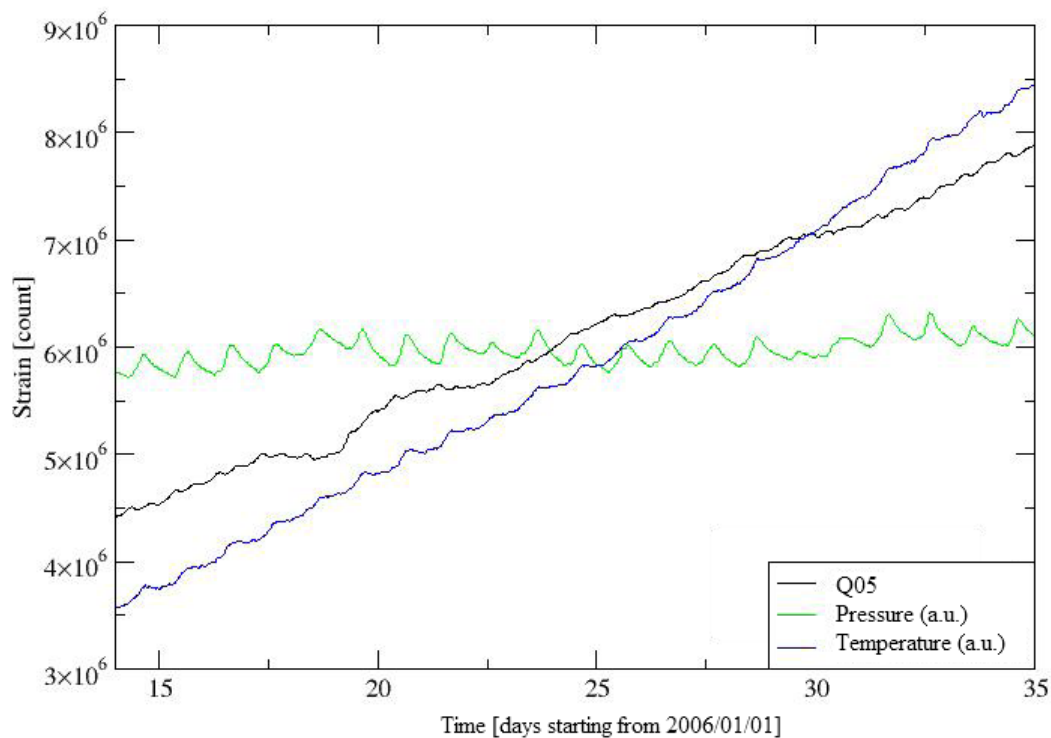

Figure 4.17 – Strain (black), barometric pressure (green – arbitrary units) and temperature (blue – arbitrary units) recorded at Rione Toiano for the period 2006/01/14 – 2006/02/06.

Strain data and environmental time series pre-whitened are the input sets for the Analisi software, which returns the amplitude ratios and the phase differences of the estimated tidal coefficients for the experimental data. The input data have been previously detrended, subtracting barometric pressure and

93

thermal effects. Data sets must have a minimum length in order to resolve the desired number of tidal harmonic components, since the maximum resolvable distance in frequency between two neighboring harmonics is given by the inverse of the period T of acquisition: for a data set of 8 days in length, it is possible to resolve 3 tidal groups; from 8 to 16 days, 5 tidal groups; from 16 to 180 days, 12 groups; from 180 to 364, 14 groups; and so go on. Each group is identified by the number of the harmonic component which closes the group itself, and moreover the lower the number of groups resolved, the greater the number of the components that contribute to each group. We will consider the relationship between the amplitudes for the 12-hours tidal group, and from this relationship we will derive the scaling factor, and even information about the actual sensitivity of the instrument.

4.1.5 – Results

Here are the results of the Analisi software for two of the three stations of the Campi Flegrei, Quarto and Rione Toiano, since from our preliminary analysis, for the considered period, the Monteruscello dilatometer is not able to see the deformations caused by Earth tides.

Quarto

For the Quarto station, we analyzed three time series. The first starts on 2005/09/22 and ends on 2005/10/19 (27 days): this is a subset of one of the time series previously mentioned, and the choice is due to the fact that the atmospheric pressure data in this time range was available. Similarly, we chose for the same reason two more series (2006/01/18 – 2006/02/04 [17 days] and 2006/03/10 – 2006/03/30 [20 days]) from another data set. Atmospheric pressure data were recorded from the meteorological station of Licola for the first data set, while the second and third data sets had associated the barometric pressure measured by the pressure sensor contained into the electronic equipments of the station itself. Pressure data are measured in counts, and series were down-sampled at 1800 seconds.

The PSDs depicted into Figure 4.18 show how the pressure effects have a frequency range which overlaps the tidal frequency range. The ratio of the recorded tidal signal with the theoretical data signal gives the following value for the relationship count-strain:

$$1 \text{ count} \sim 5 \times 10^{-11} \text{ strain} \tag{4.1.8}$$

The Analisi software results are summarized in Table 4-1, where are shown all of the resolved tidal groups. We were able to resolve 5 tidal groups (and not 12), because of the noise level of strain signals and of the environmental signals. The value corresponding to the 12-hours component are contained into the group 296. The inverse of the Amplitude for this group gives an approximate value of:

$$1 \text{ count} \sim 4 \times 10^{-11} \text{ strain} \tag{4.1.9}$$

Table 4-1 – Table of the relationship of the amplitudes and phase shifts for the tidal groups coming from Analisi in the period of time ranging from 2005/09/22 to 2005/10/19 for the station of Quarto

Group	Amplitude	Phase (degrees)
113	22.3213	-170.08
205	13.9414	-150.84
296	22.4325	-146.22
360	19.3745	163.04
377	57.1123	-31.54

Figure 4.18 – PSDs comparison among the experimental strain data (black), the theoretical tide (red) and the atmospheric pressure (green – millibar) recorded in Quarto for the data set 2005/09/22 – 2005/10/19
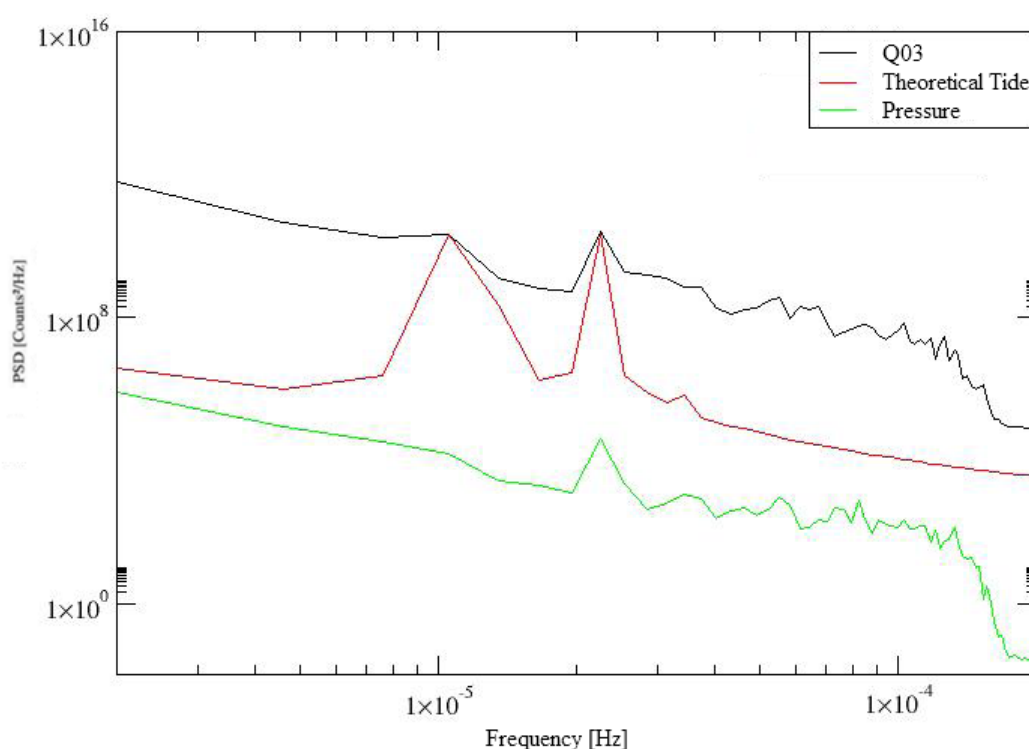
The second time series taken in account lasts 17 days and ranges from 2006/01/18 to 2006/02/04. Comparing the PSD of the M2 tidal component (Figure 4.19) between the experimental signal with the theoretical signal, we found a count-strain value:

$$1 \text{ count} \sim 6 \times 10^{-11} \text{ strain} \qquad (4.1.10)$$

while the inverse of the amplitude for the group 296 (Table 4-2) gives:

$$1 \text{ count} \sim 3 \times 10^{-11} \text{ strain} \qquad (4.1.11)$$

Table 4-2 – Table of the relationship of the amplitudes and phase shifts for the tidal groups coming from Analisi in the period of time ranging from 2006/01/18 to 2006/02/04 for the station of Quarto

Group	Amplitude	Phase (degrees)
113	18.3398	-169.27
205	19.0572	-148.47
296	21.5728	-145.05
360	27.7744	142.69
377	137.6120	-121.43

Figure 4.19 – PSDs comparison among the experimental strain data (black), the theoretical tide (red) and the atmospheric pressure (green – millibar) recorded in Quarto for the data set 2006/01/18 – 2006/02/04
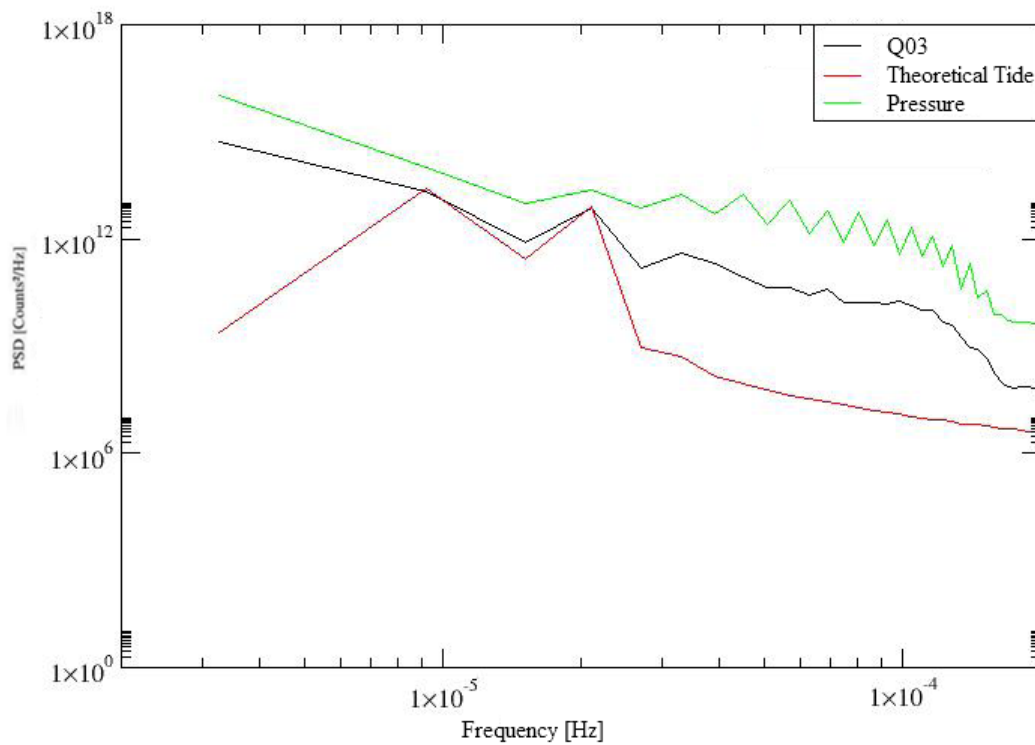
The last time series analyzed for Quarto starts on 2006/03/10 and ends on 2006/03/30, for a total length of 20 days. Comparing the PSD of the M2 tidal component (Figure 4.20) between the experimental signal with the theoretical signal, we found a count-strain value:

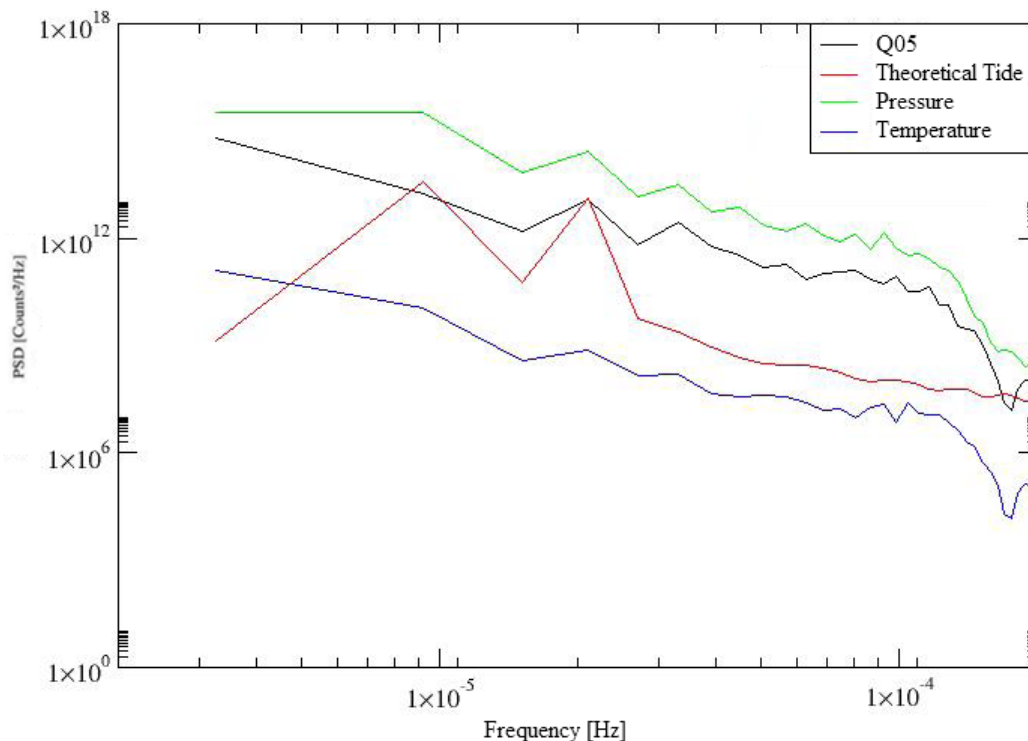$$1 \text{ count} \sim 3 \times 10^{-11} \text{ strain} \qquad (4.1.12)$$

while the inverse of the amplitude for the group 296 (Table 4-3) gives:

$$1 \text{ count} \sim 6 \times 10^{-11} \text{ strain} \qquad (4.1.13)$$

Table 4-3 – Table of the relationship of the amplitudes and phase shifts for the tidal groups coming from Analisi in the period of time ranging from 2006/03/10 to 2006/03/30 for the station of Quarto

Group	Amplitude	Phase (degrees)
113	10.5779	-139.78
205	37.0338	-160.11
296	20.4300	-153.42
360	18.4726	148.75
377	118.7175	-116.34

Figure 4.20 – PSDs comparison among the experimental strain data (black), the theoretical tide (red) and the atmospheric pressure (green – millibar) recorded in Quarto for the data set 2006/03/10 – 2006/03/30
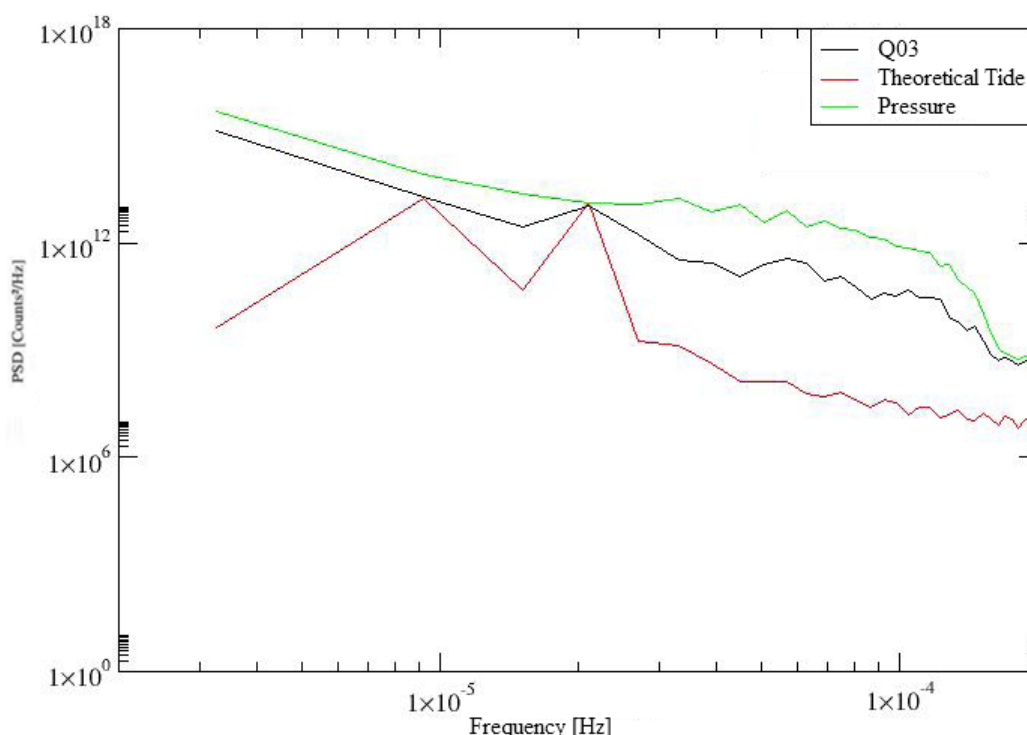
Rione Toiano

For the Rione Toiano station two time series were analyzed. The first one starts on 2006/01/14 and ends on 2006/02/04 (21 days total length), the second one starts on 2006/02/09 and ends on 2006/02/28 (19 days). Both series have been corrected by using barometric pressure and thermal effects. Pressure has been recorded by the pressure sensor integrated into the electronic of the instrument and is measured in counts. Thermal effects are measured by the dilatometer itself, using the second valve (DL2), whose diameter is bigger than the main valve (DL1): the ratio is equal to $\frac{DL1}{DL2} \cong \frac{1}{80}$, so it measures smaller changes in strain than the main valve: these changes are usually related with thermal changes, hence the thermal measurement which are of interest since the dilatometer is installed in a region sensitive to the changes in temperature. Even thermal data are expressed in counts, and all of the data have been down-sampled at 1800 seconds.

The first data set starts on 2006/01/14 and ends on 2006/02/04, for a total length of 21 days. Comparing the PSD of the M2 tidal component (Figure 4.21) between the experimental signal with the theoretical signal, we found a count-strain value:

$$1 \text{ count} \sim 3 \times 10^{-11} \text{ strain} \qquad (4.1.14)$$

while the inverse of the amplitude for the group 296 (Table 4-4) gives:

$$1 \text{ count} \sim 6 \times 10^{-11} \text{ strain} \qquad (4.1.15)$$

Table 4-4 – Table of the relationship of the amplitudes and phase shifts for the tidal groups coming from Analisi in the period of time ranging from 2006/01/14 to 2006/02/04 for the station of Rione Toiano

Group	Amplitude	Phase (degrees)
113	13.0035	-159.00
205	24.2684	136.86
296	14.4823	-167.13
360	40.4826	139.77
377	245.9885	-0.25

Figure 4.21 – PSDs comparison among the experimental strain data (black), the theoretical tide (red), the atmospheric pressure (green – millibar) and the temperature (blue) recorded in Rione Toiano for the data set 2006/01/14 – 2006/02/04

The second data set starts on 2006/02/09 and ends on 2006/02/28, for a total length of 19 days. Comparing the PSD of the M2 tidal component (Figure 4.22) between the experimental signal with the theoretical signal, we found a count-strain value:

$$1 \text{ count} \sim 3 \times 10^{-11} \text{ strain} \qquad (4.1.16)$$

while the inverse of the amplitude for the group 296 (Table 4-5) gives:

$$1 \text{ count} \sim 9 \times 10^{-11} \text{ strain} \qquad (4.1.17)$$

Table 4-5 – Table of the relationship of the amplitudes and phase shifts for the tidal groups coming from Analisi in the period of time ranging from 2006/02/09 to 2006/02/28 for the station of Rione Toiano

Group	Amplitude	Phase (degrees)
113	3.3087	-108.77
205	24.2510	118.63
296	12.7341	-171.10
360	35.1519	110.17
377	171.1791	81.42

Figure 4.22 – PSDs comparison among the experimental strain data (black), the theoretical tide (red), the atmospheric pressure (green – millibar) and the temperature (blue) recorded in Rione Toiano for the data set 2006/02/09 – 2006/02/28
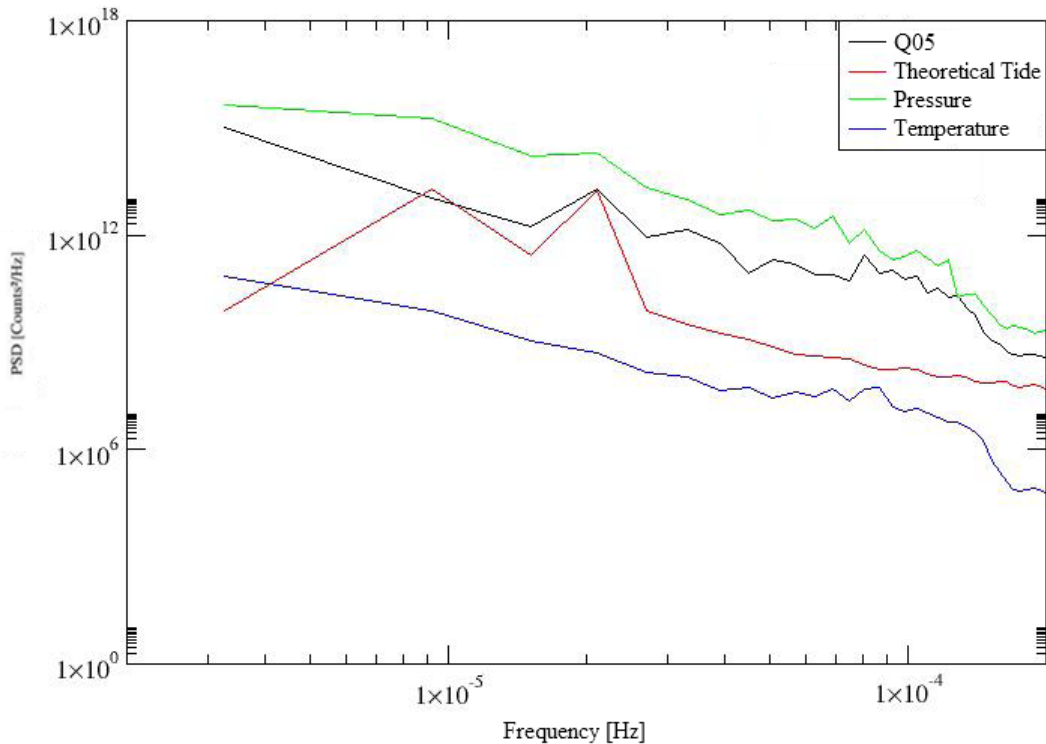
4.1.6 – Calibration Conclusions

From the above results it is possible to state that the effective sensitivity for the instruments is of the order of 10^{-11} strain for the dilatometers installed in Quarto and in Rione Toiano, regarding the time series chosen for our analysis. Since thermal and barometric effects are recorded by dilatometers and lies in the same frequency range of tidal components, the Analisi software was useful in order to get rid of these kind of signals.

4.1.7 – Evidences of the 2004-2006 mini-uplift at Campi Flegrei caldera

The installed network of borehole strainmeters and broad-band seismometers is expected to contribute to the knowledge of the magma feeding system, allowing sampling of seismic and deformation signals from the deep transport, storage, and recharge systems, and constitute one of the best known short- and middle-term instrument combinations with potential for eruption forecasting. So, the main goal of the array of dilatometers installed at Campi Flegrei is to improve estimates of the depth of the pressure source in case of unrest, and possible detection of ground deformation accompanying small pressure variations due to increased bubble formation, hydrothermal fluid motions, and/or magmatic ascent in the pre-unrest stage. The high sampling frequencies of these strainmeters is moreover of great value in identifying the possible occurrence of long-period (LP) or very-long-period (VLP) volcanic earthquakes, having important implications for mass transport in volcanic system.

The most recent uplift in Campi Flegrei started in November 2004, after the installation of the network, and includes two episodes up to present (in 2004, and 2005), +0.6 ÷ +1.6 mm/month and +2.3 ÷ +3.1 mm/month respectively, as revealed by GPS data *[Pingue et al, 2006]*.

Figure 4.23 – Time evolution of the strain low passed at 10^{-2} Hz recorded at Campi Flegrei dilatometers in the period July 2004 – June 2010. The figure below show the temperature trend, which is stronger at Rione Toiano (Q05 – ARCO) station but almost negligible at Quarto and Monteruscello dilatometers.
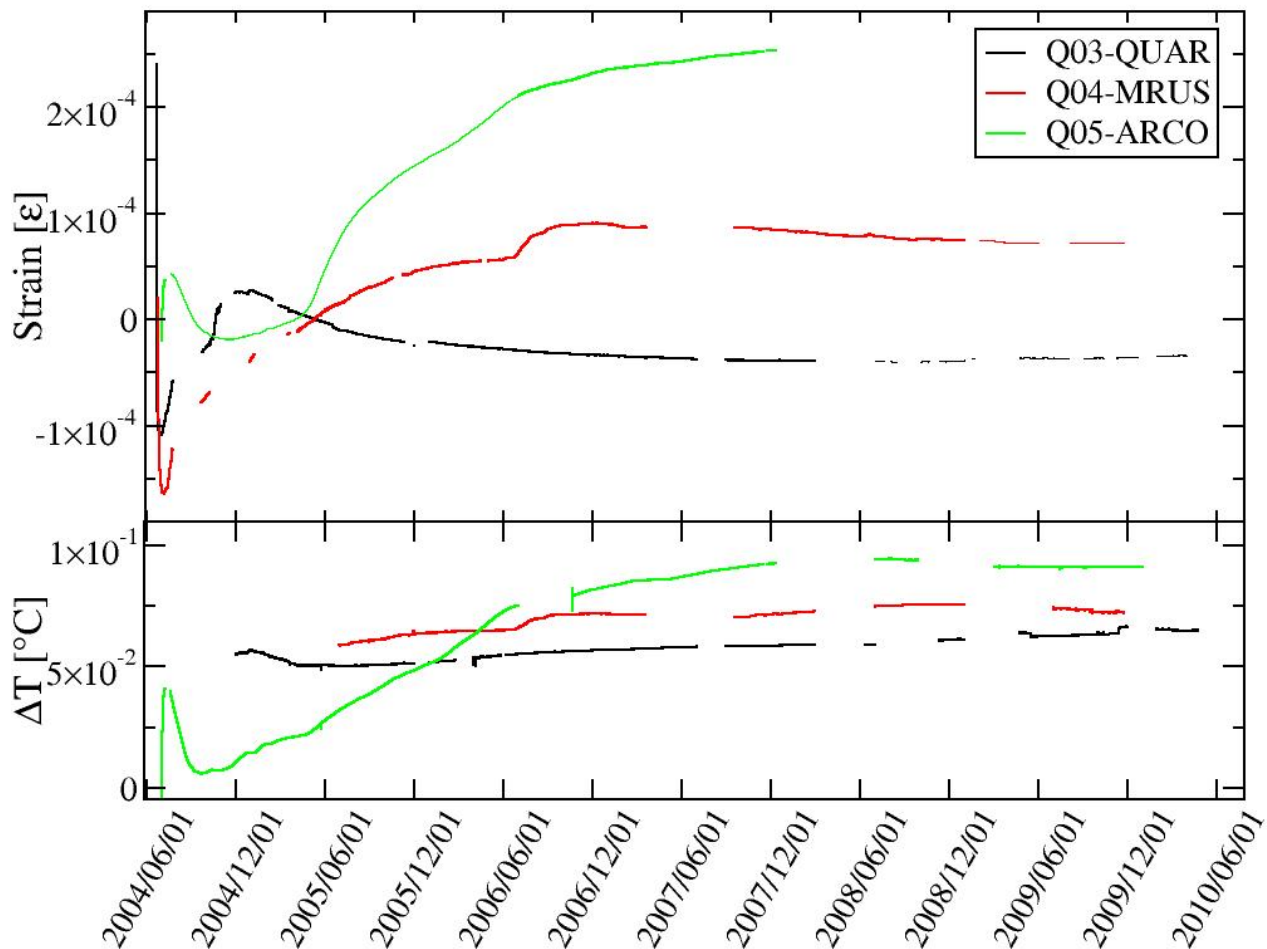
The time series of the strainmeter signals, starting from the installation, are in Figure 4.23, and show overall stable trends. Data recorded during the first few months are heavily affected by strains associated with curing cement. Data interruptions in the first months of operations are due to some problems in the electronics (battery charger, data logger, etc.), mainly at Quarto and Monteruscello sites (the most sensitive and stable sites, as seen in previous paragraphs).

Strain records at Toiano station, which has the strongest signals and is the closest (about 3 km) to the center of uplift, show some slope changes (10^{-6} /week) that may be related to miniuplift episodes. Changes in strain rates occurred in October 2004 and May 2005, and preceded the two seismic swarms in March and October 2005 by about 4 months, consistent with the observations of the 1982-1984 crisis and the latest miniuplift episodes. Another seismic swarm occurred during October 2006 and is followed by an increase of strain of comparable order observed at Monteruscello during late June (unlikely Toiano was not recording at that time).

Associated with these stain rate changes at Toiano are intriguing temperature changes. Ambient temperature at the strainmeter depth (~120m) is very high, close to 60 deg °C, presumably due to influences of the hydrothermal system. Numerous studies (e.g., *Battaglia et al.* and references therein) have suggested that fluid flow is an integral component of the mechanism for repeated episodes of uplift and subsidence in the Campi Flegrei region.

At Toiano temperature increased at a rate about 15 millidegrees/month over about one hundred days. Thermal stability at Quarto and Monteruscello is greater by almost two orders of magnitude. These changes provide the potential for novel insight into the source processes.

Work is in progress on interpretation of observations and modeling of source mechanisms. The strain and GPS data appear to be consistent with pressure increase in a source centered under the uplift peak together with a second shallower source located not too distant from Toiano. The temperature increase and the strain changes at Toiano are likely to be direct evidence for magma chamber induced fluid migration.

In summary, the network has detected changes that appear to be related to the process originating a new cycle of miniuplift of the Campi Flegrei volcanic area. This is very promising for the future. Progress in modeling the source(s) responsible for present unrest episodes, i.e. answering the still open question about magmatic and/or hydrothermal causative source of the Campi Flegrei ground deformations and microgravimetric changes, should aid hazard assessment at Campi Flegrei.

4.1.8 – Slow events and surface waves recorded by Campi Flegrei instruments

Dilatometers installed at Mt. Vesuvius and Campi Flegrei recorded many slow events. A great number of slow events were found through all of the data recorded from the three Campi Flegrei stations, as depicted in Figure 4.24.
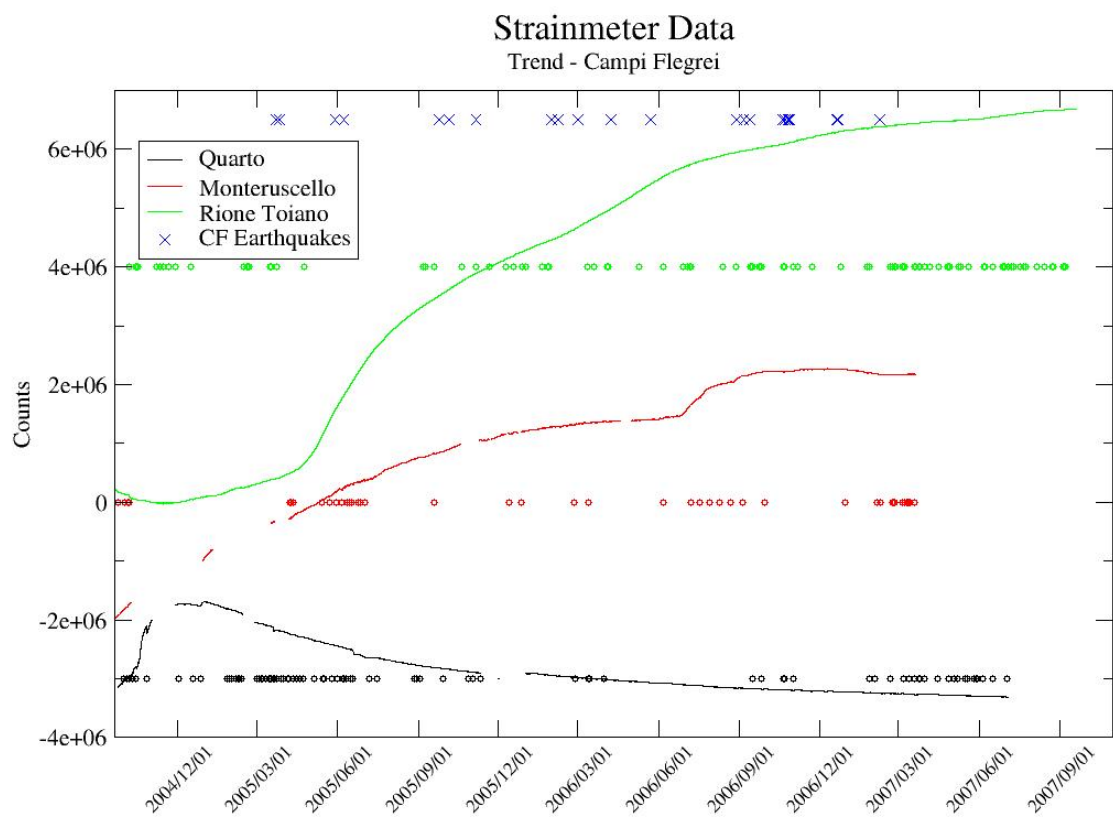
Slow events recorded have rise times of minutes to hours (see Figure 4.25), at least two sets of which (occurred in October 2004 and May 2005) show some general, though not specific, temporal correlation. Slow events are not correlated with air pressure changes and rain.

Some slow events recorded from the three Campi Flegrei instruments seem to be correlated: maybe a stress diffusion could be related with events recorded at slightly different time at the sites.

Figure 4.25 – Straingram of a typical slow event. The event seems to be the same, recorded at slightly different time at the three stations.

Slow Event Comparison

Strain Data
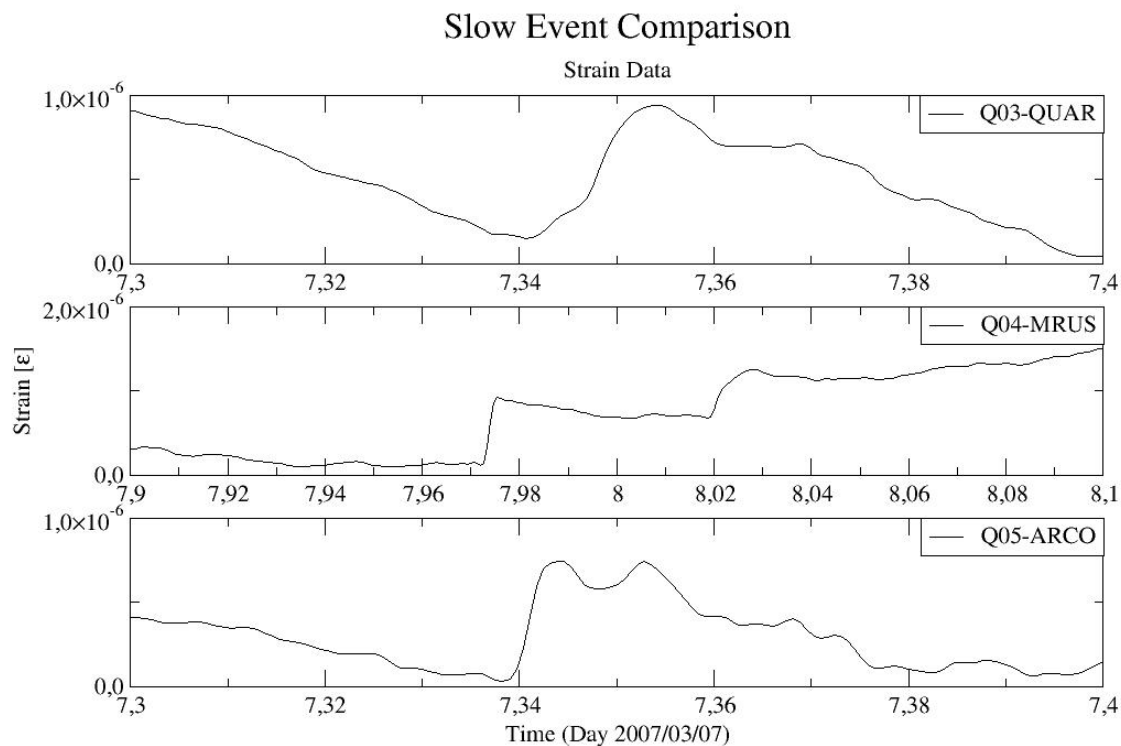
Clear records of surface waves are recorded from the dilatometers installed in Campi Flegrei too. A typical example is the straingram which shows the record from November 11th 2006 Kuril Islands earthquake: it has been obtained at all the three sites of the network (Figure 4.26).

Figure 4.26 - Example of straingrams of the Kuril Islands 15.11.2006 (M=8.3) earthquake

Kuril Islands Earthquake (M = 8.3)

2006/11/15 - Strainmeter Data
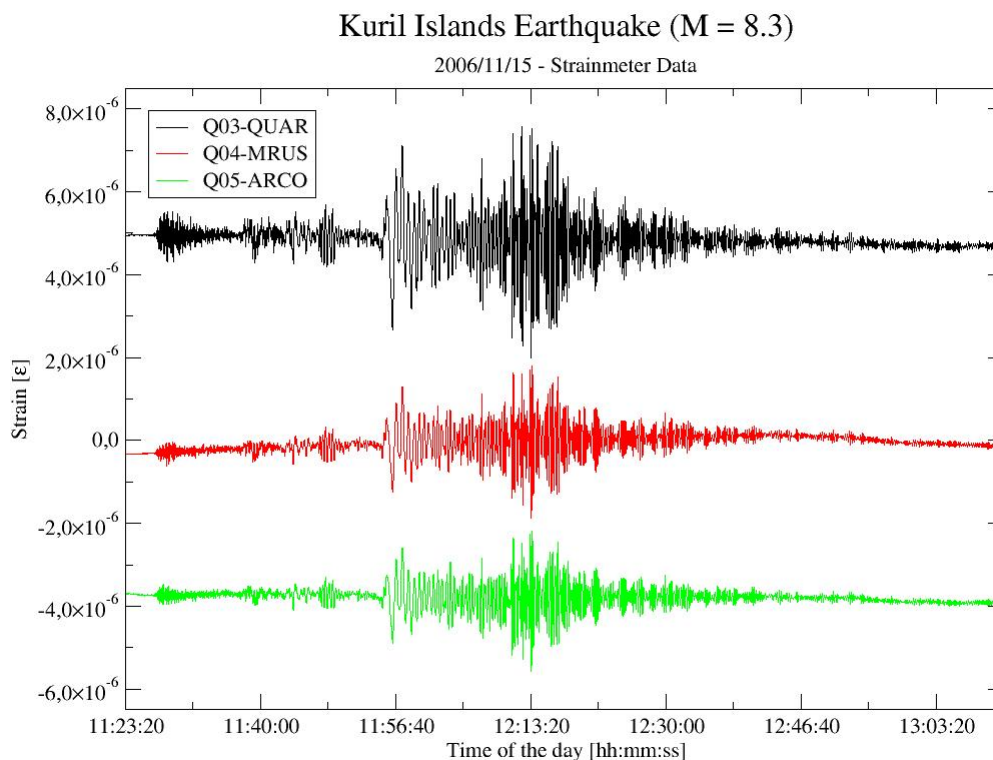
4.2 – Tilt Data Analysis

In the current paragraph tilt data analysis will be described. This is mainly a preliminary data analysis related with data sets coming from the two long baseline tiltmeters which don't overlaps each other because of different installation time.

4.2.1 – Data integrity

Although each sensor is calibrated to 1% before deployment, and the absolute calibration may be verified by subsequent micrometer calibration, a number of tests of the in-situ calibration of the data are possible with a water pipe tiltmeter. These are unique to long baseline tiltmeters and are unavailable to other forms of long period strain or tilt measurement. For real tilts, the signals at each end of the tiltmeter are identical and out of phase [Bilham et al., 1982]. Conversely, water level changes caused by volume changes (leaks or uniform thermal expansion) are identical at each end, and in phase *[Plumb et al., 1977]*. Both attributes may be exploited to test the relative calibration of the sensors, an important feature since an error in calibration in the presence of water level changes attributable to leaks or to thermal expansion would otherwise be manifest as long term tilt.

Figure 4.27 – An independent verification of relative calibration and hydraulic connectivity obtained by adding 2 litres of water near the central transducer of the North/South pipe. Water oscillations cease after approximately 30 minutes. The observed mean increment in water level (75.8μm) is not identical on all three sensors due to tidal tilt of the tunnel during the time taken to attain equilibrium.
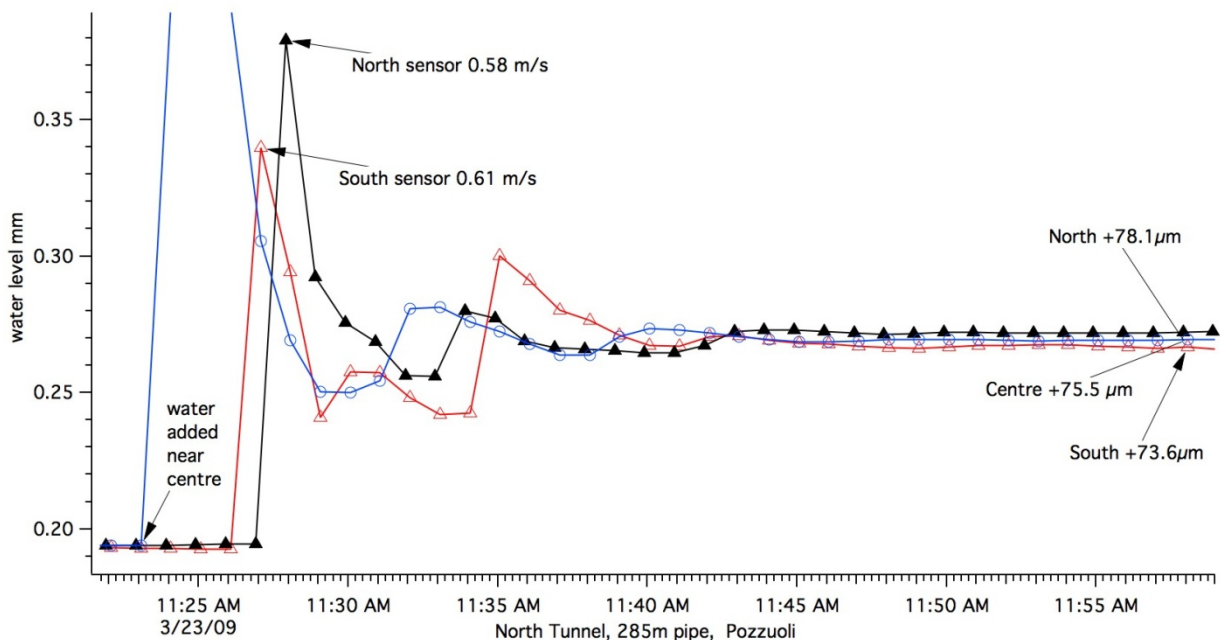
A simple verification on relative calibration accuracy is to remove or to add water from the centre of the pipe. The resulting change of water level takes several minutes to spread throughout the pipe, preceded by a gravity wave propagating at a velocity of $\sqrt{gh}$ where h is the average depth of the water in the pipe (≈3 cm). Observed velocities in Figure 4.27 are ≈0.6 m/s. The wave takes approximately 3.7 minutes to travel to the two ends from the center of the 285 m pipe, and this wave, a miniature tsunami, is reflected and takes a further 7.5 minutes to arrive at the far end of the pipe from where it is again reflected. The wave

attenuates to an undetectable level after three reflections. This incremental calibration test works well if seiches and tides are small, which is not the case in Pozzuoli, however, if the central transducer is midway, the water level excess at one end will equal the water level depression at the other. After 30 minutes in the example shown in Figure 4.27, the mean water level change recorded at the two ends is within 0.5% of that recorded at the centre.

Figure 4.28 – Power spectra and ratios at discrete frequencies (seiche periods in minutes) from two weeks of data from each sensor of the north-south pipe (September 2009). The higher noise level in the south sensor is attributable to thermal fluctuations near the entrance of the tunnel.
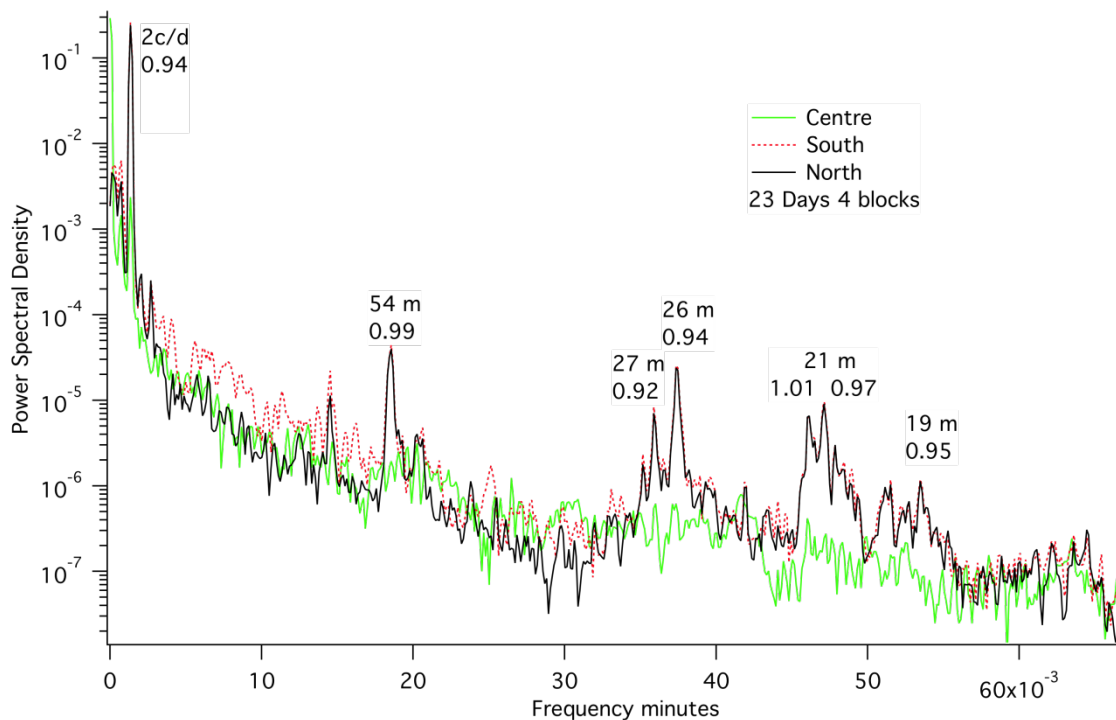
A second test of tiltmeter integrity suited to a noisy environment such as the Pozzuoli coastline can be undertaken retroactively by examining the amplitude of discrete frequencies in the data. A rich spectrum of tidal and seiche species is available to undertake this analysis. The largest amplitude signals are the diurnal and semidiurnal tides, followed by harmonics at 3 and 4 cycles per day, and seiches at periods of 2 hours in the Tyrrhenian Sea. Spectral analysis of the two ends and centre of the 285m long tiltmeter is shown in Figure 4.28. As expected the power spectral ratios (North/South amplitude squared) at discrete periods in the data are indicated for prominent spectral peaks and suggest that the mean amplitude of oscillatory tilts is larger at the southern end than the northern end. The origin of this discrepancy can be interpreted in one of two ways: a probable 2% inflated calibration of the southern sensor, or a possible flexure of the Earth's surface at the south sensor at tidal periods.

4.2.2 – Data

The first water pipe was installed in one of the tunnels in March 2008 but leaks in this pipe, power outages and vandalism interrupted data acquisition until April 2009. Additional pipes and sensors were installed in early 2009. Two months of data from the longest tiltmeter are illustrated in Figure 4.29 to demonstrate the potential fidelity of the tilt measurements. The data from the triple sensor pipe permit three combinations of

tilt to be compared – a 156-m-long northern half, a 129-m-long southern half, and the 285-m-long total length of the tiltmeter. The semidiurnal M2 tide with a peak amplitude of ≈220 nrad was used to normalize the calibration of the three time series. Seiches in the transmitted data with amplitudes two orders of magnitude lower than the tide (Figure 4.28) were suppressed in these data prior to transmission.

Figure 4.29 – Three combinations of tilt transmitted via the Iridium satellite telemetry link normalized to the amplitude of the M2 tide. A weather front associated with high winds caused a transient temperature increase of 2°C in the tunnel 13 March. Differences between the three tilt estimates of up to 20 nanoradians are attributable to temperature expansion of the end mounts.
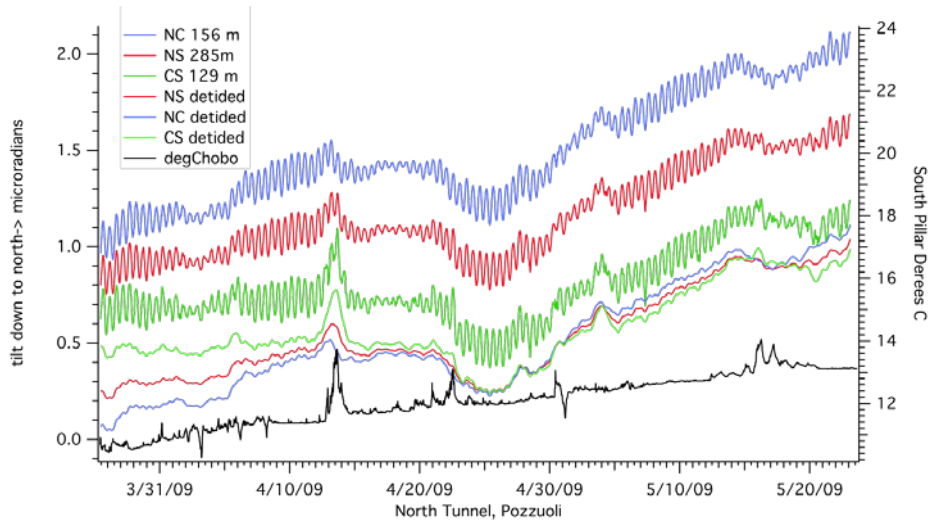
Figure 4.30 – August/September data (above) and October/November data (below) from the sensors of the North tiltmeter.
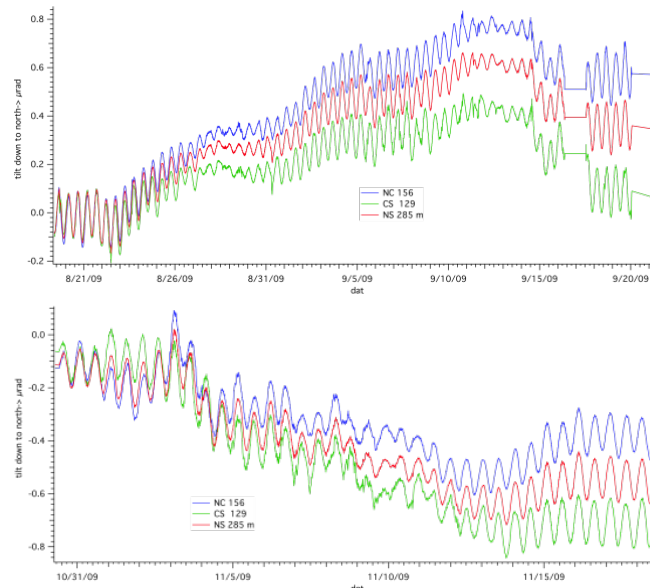
The sensitivity of the north-south tiltmeter to temperature variations in the tunnel is aggravated by the slope of the tunnel which requires the central- and south- mounts to be 1m and 1.7 m higher respectively than the north mount, which is snug with the tunnel floor. We note that the central-south tilt combination is the most sensitive to this effect (220 nrad/°C) corresponding to a differential height change of ≈28μm/°C between the

ends. If this is entirely caused by thermal expansion of the steel/concrete pillar its thermal coefficient is approximately 1.4 x10^{-5}/°C. This form of thermal influence must be suppressed analytically by direct measurement of the pillar temperature since seasonal variations in temperature in the tunnel exceed 6°C which would otherwise be perceived as a seasonal 1.2 µradian annual signal. In the data shown in Figure 4.29 the mean slope of the three tilt channels (an apparent tilt of ≈0.5 µrad down to the north) is influenced by this seasonal expansion. After correction for ensemble thermal coefficient for the entire tiltmeter we found we could reduce the tilt April May tilt change to less that 50 nrad.

### 4.2.3 – Sea level coherence near Pozzuoli in the northern Bay of Naples

The three tide gauges on the Bay of Naples that were installed to monitor relative motions of the land relative to the sea surface, also record a rich spectrum of ocean tides and harmonic resonances of the sea surface (seiches) in the Bay of Naples. A 6 week span of sea level data was subjected to spectral analysis to examine the source of harmonic loading to the sea floor. Power spectra (Figure 4.28) show four tidal species that decay slightly in coherence with decreasing period: diurnal, semidiurnal, 3 c/d and 6 c/d. Coherent sea level variations occur at nine dominant periods for seiches between 3 hours and 0.7 hours. For periods less than 40 minutes some coherence is evident, but the spectral energy density varies significantly between the three gauges symptomatic of recording short wavelength resonances near harbours.

Sea level variations that are most effective at both loading the magma chamber and tilting the shoreline are those with the same amplitude throughout the Bay of Pozzuoli. To identify these periods we took the mean ratio of the sea level amplitude between Mise and Pozz and Nise and Pozz, and plotted only those values within 10% of unity. The ratio is large (and meaningless) for those periods where coherence is poor. We find as may be expected that the longest periods show the best coherence and the most similar variations in sea level. The spectral power in Figure 4.31 is proportional to amplitude squared, and hence a ±10% difference in the plotted ratio, represents a ±3.2% difference in amplitude.

The semidiurnal tide is the largest dilatational forcing function near Pozzuoli. Its amplitude is 5-10 times larger than the diurnal 1c/d and the 3c/d and 6c/d harmonics. Moreover, at semidiurnal periods sea-level variations are identical at the three tide gauges. The 3c/d and 6c/d tides both show departures from unity. Seiche periods at 2.5, 2.1, 1.4, 1.1, 0.9, 0.8 hours and specral lines at 0.6 and 0.7 hours show good coherence, but the ratio in many cases departs from unity, indicating the sea-surface slopes at these periods, presumably the result of antinodes within the Bay. Periods less than 40 minutes are coherent but vary significantly in amplitude from one tide gauge to the other.

Previous studies of seiches in the Bay have identified a resonance of 5.7 hours and another of 55 minutes attributable to the Tyrrenium Sea *[Speich and Mosetti, 1988]* and periods of 58, 48, 22 and 17.8 minutes reported from tide gauges in the Bay *[Caloi and Marcelli, 1949]*. Our data capture these and numerous other seiche periods. Hydrographic models of the Bay of Naples are unable to reproduce seiches with periods greater than 1 hour.

Figure 4.31 – Sea level spectra and coherence tide gauges near the tiltmeters in Pozzuoli. Colored curve indicates the power spectrum from the three tide gauges. The grey area indicates periodic fluctuations in sea level that are more than 90% coherent between the tide gauge Mise and tide gauge at Pozzuoli. The circles indicate the mean ratio of amplitude between the three gauges, the size of the circle being inversely proportional to their standard deviation. Large circles close to unity (horizontal line) indicate periods where sea level produces both maximum dilatational load on the sea floor and maximum tilt on shore near the tiltmeters.
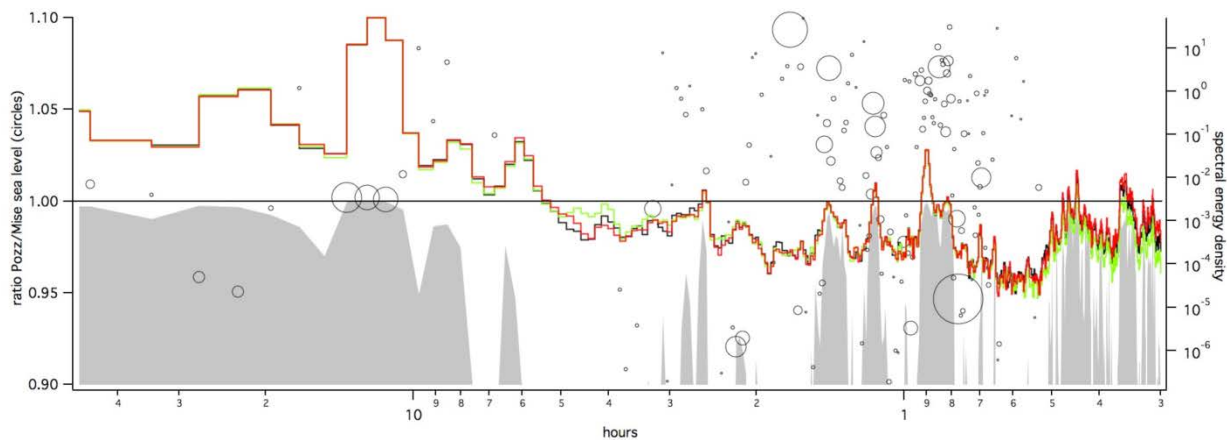
4.2.4 – Response of the tiltmeters to harmonic variations in sea level

We speculate that the admittance between load and tilt may provide a sensitive measure of the rheology surrounding the subsurface magma chamber. Approximately 1 m of sea level change produces 0.1 mm of relative height change in the north-south pipe. The relative contribution of fluid and gas phases in a magma source near the shore could, in principle, change this admittance. The weaker the system, the more likely are offshore stresses to produce an increase in tilt. Although the ratio of tilt to load tide can be undertaken at any period, there are advantages to undertaking this at discrete periods using power-spectral averaging methods.

In Figure 4.32 we show the spectral response of the longest tiltmeter (North-South 150 m) and the Pozzuoli tide gauge. Despite broad coherent energy between tide gauges below 40 minutes we see no significant tilt signal, confirming that these frequencies represent subharmonics in Bay seiches whose nodes and antinodes result in shear stress but no uniform dilatational loading of the sea floor. The coherence between the sea loading signal and tilt at periods greater than 40 minutes is encouraging, and seiches have the advantage that they have no counterpart in the astronomical tides, but we have insufficient data at present to examine the admittance between sea level forcing and the onshore tilt response throughout the year.

Harmonic analysis methods work best where the length of the data are much longer than the periods of interest. Thus although our analysis demonstrates that the semidiurnal tide is the dominant periodic loading function available for our study, the presence of coherent energy at 2.5 and 1.1 hours, despite the two orders of magnitude lower loading amplitude, would in principle permit us an order of magnitude higher time resolution. In practice the seiche amplitudes during periods of atmospheric calm could in principle reduce to vanishingly small amplitudes, and it is thus probable that the semidiurnal load tide will remain the forcing signal of choice in our subsequent analysis.

Figure 4.32 - Power spectra for Pozzuoli sea level and north-south tilt October 2009. The ratios of sea/level amplitude^2 (m^2) to difference in height^2 between the two ends of the tiltmeter (mm^2) are indicated for selected harmonics (These are summarized in Figure 4.33).
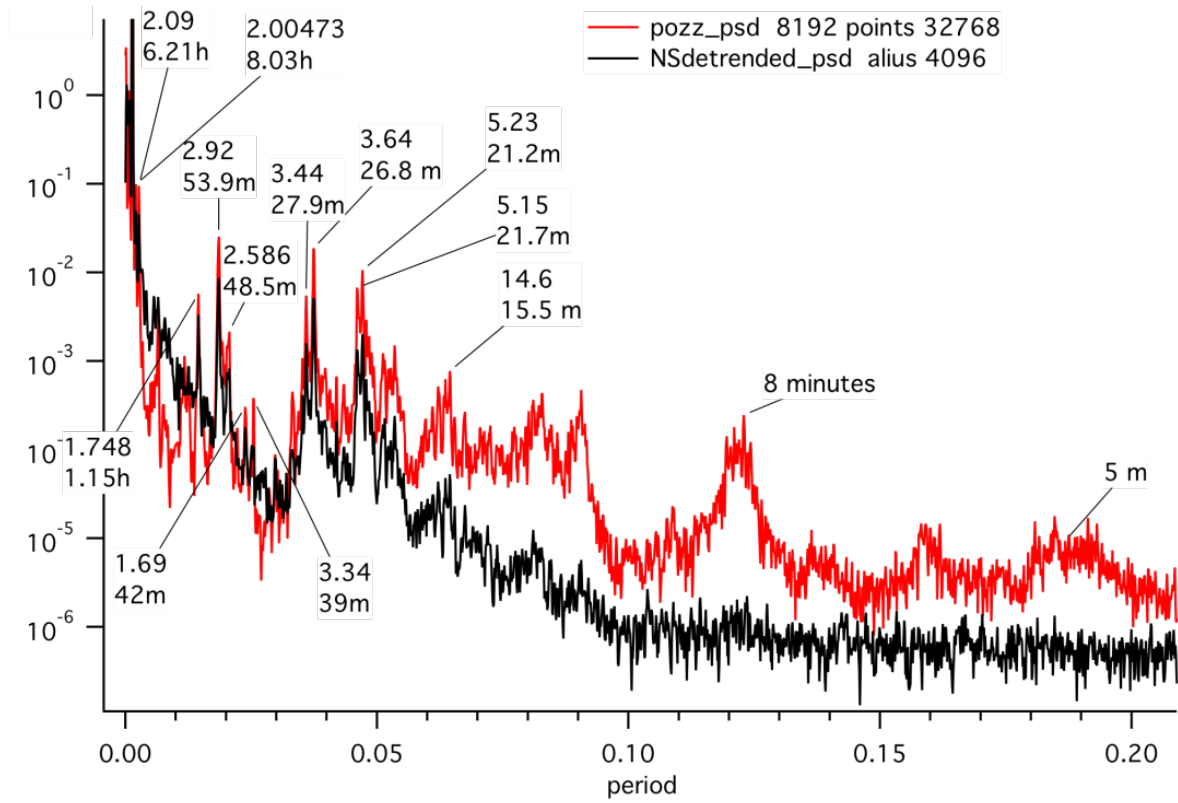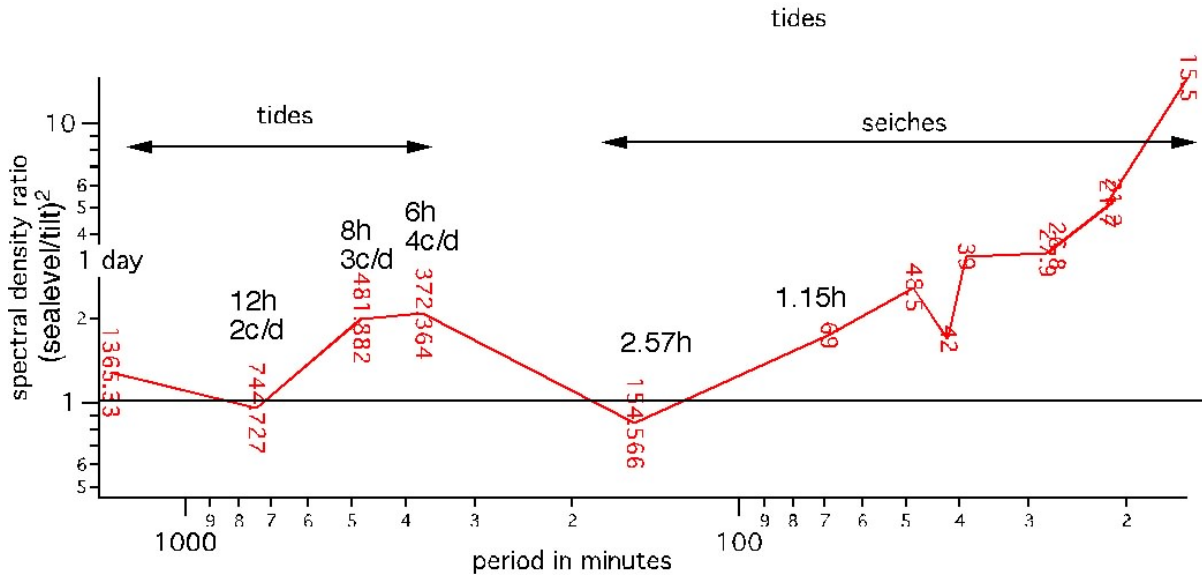

Figure 4.33 – Tilt response to sea level loading at discrete periods. The amplitude ratio for tidal periods is close to unity but is not well resolved in this two week analysis. Tilt responds decreasingly to seiches with periods shorter than 40 minutes.

Acknowledgments

Bibliography

Agnew, DC., Strainmeters and tiltmeters, Rev. Geophys., 24, 579-624, 1986

Blum, P.-A., Contribution à l'étude de la verticale en un lieu, Ann. Geophys., 19, 215-243, 1962.

Beavan, J., Bilham, R., Thermally Induced Errors in fluid Tube Tiltmeters, Journ. Geoph. Res., vol 82, n°36, pp 5699-5704, 1977.

Bilham, R., Beavan, J., Plumb, R., Long Michelson Fluid Tiltmeters for tectonic Studies, EOS Trans. AGU, 59, 1030, 1978.

Bilham, R., Beavan, J., Evans, K., Long baseline Fluid-Tube Tiltmeter Geometry and the Detection of Flexure of Tilt, Proc of 9th Int. Symp. On earth Tides, New-york, 85-94, 1983.

Bilham, R. G., Plumb, R., Beavan, R. J., Design Considerations in an Ultra-Stable, Long Baseline Tiltmeter- Results from a Laser Tiltmeter Terrestrial and Space Techniques in Earthquake Prediction Research, Vogel, Friedr. Vieweg und Sohn, Viesbaden, 235-254, 1979.

Boudin, F., Développement et validation d'un inclinomètre longue base de subsurface à silice et mercure : Application à des mesures géophysiques de haute résolution sur le chantier pilote du Golfe de Corinthe.

Dal Moro G., Zadro, M., Subsurface Deformations Induced by rainfall and Atmospheric Pressure: Tilt/Strain Measurements in NE-Italy Seismic Area, Earth and Planet. Sc. Let., 164, 193-203, 1998.

Dietrich, J. H., Earthquake nucleation on faults with rate- and state-dependent strength, Tectonophysics, 211, 115-134, 1992.

Dragert, H., Wang, K., James, T. S., A silent slip event on the deeper Cascadia Subduction interface, Science 292, 1525-1528, 2001. 296 Références biliographiques

Eaton, J. P., A portable water-tube tiltmeter, Bulletin of the Seismological Society of America, 49, 301-316, 1959.

Emter, D., Meier, E., Schick, R., Long Baseline Tilt Measurement with Differential Fluid Pressure Tiltmeters, Cahiers du centre Europ. De Géodyn. Et de Séismol., 4, 51-56, 1991.

Horsfall . J, A new Geophysical Tiltmeter, Ph. D. Thesis, University of Cambridge, 1977.

Horsfall, J. A. C., King, G. C. P., A new Geophysical Tiltmeter, Nature, 274, 675-676, 1978.

Inouchi, N., Yoshimura, A., Imakiire, T., Ground Tilt Observations by Means of a Long Water-Tube Tiltmeter in Omaesaki, Shizuoka, Bull. Georg. Surv. Inst., 32, 41-50, 1987.

Jonsson, S., Segall, P., Pedersen R., Björnsson, G., Post-earthquake ground movements correlated to pore-pressure transients, Nature, 424, 179-183, 2003.

Jonsson, S., Segall, P., Agustsson, K., Agnew, D., Local Fluid Flow and Borehole Strain in the South Iceland Seismic Zone, AGU, 2003.

King, G. C. P., Bilham, Tidal tilt measurement in Europe, Nature, 243, 74-76, 1973.

Kostoglodov, V., Bilham, R., Santiago, J. A., Manea, V., Manea, M., Hernandez, V. R., Long-baseline fluid tiltmeter for seismotectonic studies of Mexican subduction zone. Geofisica Internacional, vol. 41, 1, pp 11-25, 2002.

Linde, A. T., Gladwin, M. T., Johnston, M. J. S., The Loma Prieta earthquake, 1989 and earth strain tidal amplitudes: An unsuccessful search for associated changes, Geophys. Res. Let., 19, 317-320, 1992.

Linde, A. T., Gladwin, M. T., Johnston, M. J. S., Gwyther, R. L., Bilham, R. G., A slow earthquake sequence on the San Andreas fault, Nature, 383, 65-68, 1996.

Linde, A. Sacks, S. I., Voight, B., Malin, P., Shalev, E., Mattioli, G. S., Young, S. R., Borehole Strainmeters on Monserrat: the CALIPSO Project and the July 2003 Eruption. AGU, 2003.

Malvern, L., Introduction to the Mechanics of a Continuous Medium, Prentice-Hall inc., Series in Eng. of the Phys. Sciences, 1969.

Melchior, P., The tides of the planet Earth, 1 st ed., Pergamon Press, Oxford, 1978.

Michelson, A. A., Gale, H. G., The Rigidity of the Earth, Astrophys. Journ., vol 50, 330-345, 1919.

Okada, Y., Internal Deformation due to shear and tensile faults in a half space, Bull. Seism. Soc. Am., 82, 1018-1040, 1992. 299 Références biliographiques

O'Reilly M., Read, S., Foster, P., Monitoring Dam Performance using tiltmeters, Ancol/Nzsold conf., Sydney, 1998.

Romagnoli, C., Zerbini, S., Lago, L., Richter, B., Simon, D., Domenichini, F., Elmi, C., Ghirotti, M., Influence of soil consolidation and thermal expansion effects on height and gravity variations, Journ. of Geodynamics, 35, 521-539, 2003.

Sacks, I. S., Suyehiro, S., Evertson, D. W., Yamagishi, Y., Sacks- Evertson strainmeter, its installation in Japan and some preliminary results concerning strain steps, Pap. Meteoreol. Geophys, 22, 195-208, 1971.

Sacks, I. S., Linde, A., Malin, P., Roeloffs, E. A., Hill, D. P., Ellsworth, W. L., Long Valley Deep Hole Geophysical Observatory - Strain instrumentation and Installation, AGU, 2003.

Sato, T., Ooe, M., Sato, N., Tidal Tilt and Strain Measurements and Analyses at the Esahi Earth Tide Station, Proc. of 9th Int. Symp. On Earth Tides, New-York, 223-237, 1983.

Shearer, M. P., Introduction to Seismology, Cambridge University Press, 1999.

Wenzel, H. –G., Earth Tide Data Processing Package ETERNA 3.30, Manual ETERNA33. HLP, 1996.

Wyatt, F., Cabaniss, G., Agnew, D., A Comparison of Tiltmeters at Tidal Frequencies, Geophys. Res. Lett., 9, 743-746, 1982.

Wyatt, F., Bilham, R., Beavan, J., Sylvester, A. G., Owen, T., Harvey, A., Macdonald, C., Jackson D. D., Agnew, D. C., Comparing Tiltmeters for Crustal Deformation Measurements: a Preliminary Report Geophys. Res. Let., 11, 963-966, 1984.